



January 2017

Theory And Application Development Of Electronic Structure Methods Involving Heavy Computation

Run Li

Follow this and additional works at: <https://commons.und.edu/theses>

Recommended Citation

Li, Run, "Theory And Application Development Of Electronic Structure Methods Involving Heavy Computation" (2017). *Theses and Dissertations*. 2269.

<https://commons.und.edu/theses/2269>

This Dissertation is brought to you for free and open access by the Theses, Dissertations, and Senior Projects at UND Scholarly Commons. It has been accepted for inclusion in Theses and Dissertations by an authorized administrator of UND Scholarly Commons. For more information, please contact zeinebyousif@library.und.edu.

THEORY AND APPLICATION DEVELOPMENT OF ELECTRONIC STRUCTURE
METHODS INVOLVING HEAVY COMPUTATION

by

Run Li

Bachelor of Science, University of Science and Technology of China, 2009

Master of Science, University of Minnesota –Twin Cities, 2011

A Dissertation

Submitted to the Graduate Faculty

of the

University of North Dakota

in partial fulfillment of the requirements

for the degree of

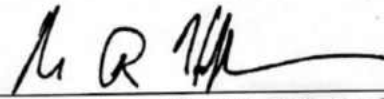
Doctor of Philosophy

Grand Forks, North Dakota

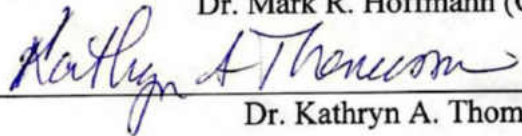
August
2017

Copyright 2017 Run Li

This dissertation, submitted by Run Li in partial fulfillment of the requirements for the Degree of Doctor of Philosophy from the University of North Dakota, has been read by the Faculty Advisory Committee under whom the work has been done and is hereby approved.



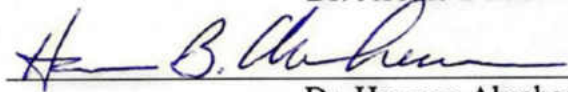
Dr. Mark R. Hoffmann (Chair)



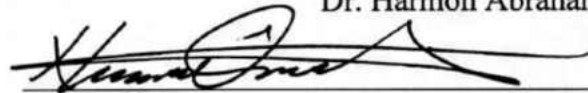
Dr. Kathryn A. Thomasson



Dr. Jerome Delhommelle



Dr. Harmon Abrahamson



Dr. Nuri Oncel

This dissertation is being submitted by the appointed advisory committee as having met all of the requirements of the School of Graduate Studies at the University of North Dakota and is hereby approved.

Grant McGimpsey
Dean of the School of Graduate Studies

Date

PERMISSION

Title Theory and Application Development of Electronic Structure Methods
 involving Heavy Computation

Department Chemistry

Degree Doctor of Philosophy

In presenting this dissertation in partial fulfillment of the requirements for a graduate degree from the University of North Dakota, I agree that the library of this University shall make it freely available for inspection. I further agree that permission for extensive copying for scholarly purposes may be granted by the professor who supervised my dissertation work or, in his absence, by the Chairperson of the department or the dean of the School of Graduate Studies. It is understood that any copying or publication or other use of this dissertation or part thereof for financial gain shall not be allowed without my written permission. It is also understood that due recognition shall be given to me and to the University of North Dakota in any scholarly use which may be made of any material in my dissertation.

Run Li
July 15, 2017

TABLE OF CONTENTS

| | |
|--|-------|
| LIST OF FIGURES | ix |
| LIST OF TABLES | xii |
| ACKNOWLEDGEMENTS | xvi |
| ABSTRACT | xviii |
| CHAPTERS | |
| I. INTRODUCTION | 1 |
| Hartree–Fock..... | 3 |
| Density Functional Theory | 5 |
| Single-Reference Perturbation Method..... | 10 |
| Configuration Interaction..... | 12 |
| Multiconfigurational Self-Consistent Field Theory..... | 14 |
| Multireference Configuration Interaction Method..... | 17 |
| Multireference Perturbation Theory | 23 |
| Ab Initio Calculation of Solids | 25 |

| | |
|--|----|
| II. THEORETICAL CALCULATIONS ON THE UV ABSORPTION OF PROPARGYL RADICAL AROUND 242 NM | 31 |
| Introduction..... | 31 |
| Methods..... | 34 |
| MRCISD(TQ) | 34 |
| Rydberg orbitals and Rydberg states | 34 |
| Computational theories used in the calculations of propargyl radical..... | 35 |
| Results and discussions..... | 39 |
| Rydberg orbital analysis with MCSCF | 40 |
| MRCISD(TQ) and Rydberg states..... | 42 |
| GVVPT2 and GVVPT3 results..... | 43 |
| Conclusions..... | 48 |
| III. PARALLELIZATION OF TRIPLE AND QUADRUPLE PERTURBATION CORRECTIONS TO MULTIREFERENCE CISD .. | 49 |
| Introduction..... | 49 |
| MRCISD(TQ) Method..... | 51 |
| Macroconfigurations..... | 56 |
| Parallelization scheme | 58 |
| Machine Specifications..... | 64 |
| Results..... | 64 |

| | |
|--|-----|
| Conclusions..... | 67 |
| IV. PARALLELIZATION OF THE SECOND ORDER GENERALIZED VAN VLECK PERTURBATION THEORY..... | 71 |
| Introduction..... | 71 |
| GVVPT2 Method..... | 72 |
| Parallelization scheme | 78 |
| Machine Specifications..... | 85 |
| Results..... | 86 |
| Conclusions..... | 91 |
| V. IMPLEMENTATION OF RESTRICTED DENSITY FUNCTIONAL THEORY IN UNDMOL..... | 93 |
| Introduction..... | 93 |
| Methods..... | 95 |
| Relationship between ROHF and UHF Fock Matrices..... | 101 |
| Test calculation results..... | 106 |
| Conclusions..... | 108 |
| VI. A DFT STUDY ON ZINC(II)-PTHALOCYANINE TETRASULFONIC ACID ON MONO-LAYER EPITAXIAL GRAPHENE ON SILICON CARBIDE(0001) | 109 |
| Introduction..... | 109 |
| Methods..... | 112 |

| | |
|--|-----|
| Calculations of periodic systems | 112 |
| Parameters used in the current study | 115 |
| Results and discussion | 117 |
| Conclusions..... | 125 |
| REFERENCES | 126 |

LIST OF FIGURES

| Figure | Page |
|---|------|
| 1. Jacob's ladder..... | 10 |
| 2. The Shavitt graph for the $(2, 1, 0^2)$ irreducible representation of the $U(4)$ group..... | 21 |
| 3. A two-dimensional Bravais lattice of no particular symmetry..... | 25 |
| 4. The first Brillouin zone of a face centered cubic crystal and the high symmetry points..... | 26 |
| 5. Miller indices in a simple cubic Bravais lattice..... | 27 |
| 6. Band structure of face centered cubic silicon crystal..... | 30 |
| 7. The most important unimolecular reaction channels for the propargyl radical together with the heats of reaction..... | 32 |
| 8. (a–c) b_1 valence orbitals. (d–g) b_2 valence orbitals. (h) $8a_1$ Rydberg orbital. (i) b_1 Rydberg orbital..... | 39 |
| 9. Equilibrium structure of propargyl radical optimized by B3LYP/AVTZ..... | 40 |

| | | |
|-----|--|-----|
| 10. | Subspace arrangement in MRCISD(TQ) method. | 53 |
| 11. | Parallelization scheme of the parallelized <i>tqcorr</i> program..... | 62 |
| 12. | Structure of subroutines in the serial <i>tqcorr</i> program. | 63 |
| 13. | Speedup curves of MRCISD(TQ) test cases..... | 69 |
| 14. | Speedup management of MRCISD(TQ) based on the macroconfigurations granularity..... | 70 |
| 15. | The potential energy curve of Mn ₂ calculated by CASPT2..... | 72 |
| 16. | Subspace arrangement in GVVPT2 method..... | 74 |
| 17. | Schematic diagram of the dependence of the correction energies on the energy difference $\varepsilon_{m_e}^p - \varepsilon_p^{(0)}$ | 78 |
| 18. | Algorithm used in the <i>mkhx</i> routine..... | 81 |
| 19. | Structure of subroutines in the serial <i>gvvpt2cfg</i> program..... | 82 |
| 20. | Parallelization scheme of the parallelized <i>gvvpt2cfg</i> program..... | 83 |
| 21. | Speedup of the <i>gvvpt2cfg.exe</i> program..... | 89 |
| 22. | The blocked structure of the Fock matrix..... | 101 |
| 23. | Structure of phthalocyanine..... | 110 |
| 24. | Structure of the Zn-PcS molecule..... | 111 |

| | | |
|-----|--|-----|
| 25. | Three-layer slab models of the MgO (100) surface. (a) With 2-D periodic boundary conditions. (b) 3-D supercell approximation of the slab model as adopted in plane wave calculations..... | 114 |
| 26. | A two-dimensional Monkhorst-Pack mesh in the first Brillouin zone..... | 115 |
| 27. | DOS of monolayer graphene calculated by PBE-D2..... | 117 |
| 28. | (a) 9nm × 9nm experimental STM image of Zn-PcS molecules. (b) corresponding line scans across each of the Zn-PcS molecules..... | 118 |
| 29. | (a) dI/dV curves measured on mono-(top)/bi-layer (middle) epitaxial graphene (MEG/BEG) and on Zn-PcS (bottom) molecule. (b) Section of the same dI/dV curves in (a), near the characteristic dip of BEG..... | 120 |
| 30. | Total DOS, projected DOS on the Zn-PcS molecule and projected DOS on graphene..... | 122 |
| 31. | HOMO and LUMO of a Zn-PcS molecule adsorbed on graphene..... | 123 |
| 32. | (a) top view and (b) side view of the charge density difference on Zn-PcS adsorbed on graphene. (c) The plane-averaged charge density difference along the direction normal to the graphene surface. | 124 |

LIST OF TABLES

| Table | Page |
|--|------|
| 1. Definition of step numbers in DRT..... | 20 |
| 2. Active spaces and electron occupations used in the calculations..... | 37 |
| 3. Geometry parameters obtained from current and previous calculations. | 40 |
| 4. Main configurations of the excited states..... | 41 |
| 5. Average distance of electrons to the C-C-C-H axis (Bohr)..... | 42 |
| 6. MRCISD(TQ) and MRCISD calculation results..... | 43 |
| 7. Basis set effect of GVVPT2 and GVVPT2 calculations..... | 44 |
| 8. GVVPT3 and extended GVVPT2 in AVTZ basis set results..... | 47 |
| 9. Details of the molecules used in benchmark MRCISD(TQ) calculations..... | 68 |
| 10. Details of the molecules used in GVVPT2 benchmark calculations..... | 88 |
| 11. Calculation times (in seconds) test cases..... | 91 |
| 12. Expanding Fock matrices of closed- and open-shell parts in ROHF..... | 104 |
| 13. Test calculation on single point energies | 107 |

LIST OF ABBREVIATIONS

| | |
|--------|--|
| AVTZ | aug-cc-pVTZ |
| ACVTZ | aug-cc-pCVTZ |
| AVQZ | aug-cc-pVQZ |
| CAS | Complete Active Space |
| CBS | Complete Basis Set |
| CI | Configuration Interaction |
| CSF | Configuration State Function |
| CPU | Central Processing Unit |
| DFT | Density Functional Theory |
| DIIS | Direct Inversion in the Iterative Subspace |
| DOS | Density of States |
| DRT | Distinct Row Table |
| GGA | Generalized Gradient Approximation |
| GUGA | Graphical UGA |
| GVVPT | Generalized Van Vleck Perturbation Theory |
| GVVPT2 | the Second order GVVPT |
| GVVPT3 | the Third order GVVPT |

| | |
|------------|--|
| HOMO | Highest Occupied Molecular Orbital |
| LDA | Local Density Approximation |
| LSDA | Local Spin Density Approximation |
| LUMO | Lowest Unoccupied Molecular Orbital |
| MCSCF | Multiconfigurational Self-Consistent Field |
| mDRT | modified DRT |
| MP2 | the Second Order Moller–Plesset perturbation theory |
| MPI | Message Passing Interface |
| MRCI | Multireference Configuration Interaction |
| MRCISD | MRCI including Single and Double excitations |
| MRCISDTQ | MRCI including Single, Double, Triple, and Quadruple excitations |
| MRCISD(TQ) | MRCISD corrected by Triple and Quadruple excitations |
| MRPT | Multireference Perturbation Theory |
| PAW | Projected Augmented Wave |
| RAS | Restricted Active Space |
| RDFT | Restricted DFT |
| RHF | Restricted Hartree–Fock |
| RODFT | Restricted Open-shell DFT |
| ROHF | Restricted Open-shell Hartree–Fock |
| SGA | Symmetric Group Approach |
| STM/STS | Scanning Tunneling Microscopy/Scanning Tunneling Spectroscopy |
| TQ | Triple and Quadruple |
| UDFT | Unrestricted DFT |

| | |
|--------|--|
| UGA | Unitary Group Approach |
| UHF | Unrestricted Hartree–Fock |
| UV | Ultraviolet |
| Zn-PcS | Zinc(II)-Phthalocyanine Tetrasulfonic Acid |

ACKNOWLEDGEMENTS

Till this day, I still cannot believe that I'm about to graduate. Looking back, I see myself learning and progressing. From not knowing what a CI matrix is, not knowing whether GVVPT2 or MRCISD is more accurate, to now, writing this dissertation. I couldn't have done it without my supervisor Dr. Mark Hoffmann. He has always been there for me every step of the way, encouraging me to go on pursuing the next research topic, guiding me toward the right direction. Learning his way of conducting research and incorporating ideas across disciplines was a tremendous experience and will always be a great treasure to me. I would also like to thank my committee Dr. Nuri Oncel, Dr. Harmon Abrahamson, Dr. Kathryn Thomasson, and Dr. Jerome Delhommelle. Their advice during our research collaboration and annual oral progress reports helped me shaping my research into this dissertation. I'm very grateful for Dr. Yibo Lei. His short visit fast forwarded my understanding of multireference wave function methods immensely.

It was fortunate of me to share my graduate school experience with Eric Timian, Dr. Yuanjun Li, Minh Duong, Sylvester Popis, and Dr. Shuhui Yin in this research group. They have been my inspirations in research and life, and more importantly they have always supported me as friends. A special thank you goes to Jason Hicks who has been my

great friend and role model on communication and social interaction; and Hans Musgrave for refueling my passion for research.

I would like to thank my dearest friends who supported me all these years. Ziwei Qi, Harpa Jonsdottir, Mei-Chuan Lin, and Asina, I can't imagine what my life would have been if I didn't have you. Last but not the least, I would like to thank my parents for supporting me all through my life, for making me who I am today, for trusting me to make the best decisions for myself, and for giving me the freedom to explore the world and to make my mistakes.

ABSTRACT

The propargyl radical, the most stable isomer of C_3H_3 , is very important in combustion reactions. However, theoretical calculations have never been able to find a strong absorption around 242 nm as seen in experiments. In this study, we calculated the electronic energy levels of the propargyl radical using highly accurate multireference methods, including multireference configuration interaction singles and doubles method with triples and quadruples treated perturbatively [denoted as MRCISD(TQ)], as well as second and third order generalized Van Vleck perturbation theories (GVVPT2 and GVVPT3). Calculations indicate that this absorption can be solely attributed to a Franck-Condon-allowed transition from the ground B_1 state to the Rydberg-like first A_1 excited state. Calculations also show that GVVPT2 with a relatively small active space fails to capture enough Rydberg character of this excited state, while it can be recovered by GVVPT3, MRCISD, and MRCISD(TQ).

In order to speed up MRCISD(TQ) calculations, the triple and quadruple (TQ) perturbative corrections, the most time-consuming part of MRCISD(TQ) calculations, were parallelized using Message Passing Interface (MPI). The MRCISD(TQ) method is organized in the framework of macroconfigurations, which allows the use of incomplete reference spaces and provides an efficient means of screening large number of non-

interacting configuration state functions (CSFs). The test calculations show that the parallel code achieved close to linear speed-up when the number of CSFs in each macroconfiguration is small. The speed-up suffers when large numbers of CSFs exist in only a few macroconfigurations.

The computer algorithm for second-order generalized van Vleck multireference perturbation theory (GVVPT2) was similarly parallelized using the MPI protocol, organized in the framework of macroconfigurations. The maximum number of CSFs per macroconfiguration is found to have less influence on the MPI speedup and scaling than in the case of MRCISD(TQ).

It was previously found that unrestricted local density approximation (LDA) orbitals can be used in place of MCSCF to provide orbitals for GVVPT2. This inspired us to use the more controllable restricted density functional theory (DFT) to provide unbiased orbitals for GVVPT2 calculations. In this study, the relationship between restricted DFT and unrestricted DFT were explored and the restricted DFT results were obtained by utilizing subroutines from unrestricted DFT calculations. We also found that the DIIS technique drastically sped up the convergence of RDFT calculations.

Plane wave DFT methods are commonly used to efficiently evaluate solid state materials. In this work, the electronic properties of pristine graphene and Zn-phthalocyanine tetrasulfonic acid (Zn-PcS) physisorbed on single-layer graphene were calculated using plane wave DFT. The Perdew-Burke-Ernzerhof functional with dispersion

correction (PBE-D2) was used. The densities of states were obtained for both pristine and adsorbed graphene, and the disappearance of the characteristic dip in the density of states of the adsorbed system was attributed to the lowest unoccupied molecular orbital of the adsorbed molecule. A small charge transfer from graphene to the molecule was found. We present comparison of DFT results with Scanning Tunneling Microscopy/Spectroscopy data.

CHAPTER I

INTRODUCTION

Modern computational chemistry is widely used in predicting the reactive and spectroscopic properties of chemical systems. For sufficiently small systems, such calculations usually begin with electronic structure calculations that generate potential energy curves or surfaces, followed by dynamic calculations to study the state-to-state rate of reaction and possibly macroscopic behavior. Traditional electronic structure methods can be classified as semi-empirical methods (such as AM1, PM6),¹ mean-field methods (including Hartree–Fock and density functional methods),^{2–5} single reference perturbation methods⁶ (for example the second order Møller–Plesset perturbation theory (MP2)⁷) and their multireference extensions,^{8,9} multiconfigurational self-consistent field method,¹⁰ single reference configuration interaction including single and double excitations and their multireference extensions (multireference configuration interaction¹¹), single reference coupled cluster^{12,13} including single and double excitation operators, and their multireference extensions,^{14–16} etc. For larger molecules, which cannot be treated by electronic structure methods, force field methods^{17,18} (molecular mechanics methods) can be useful. For instance, force fields can treat systems composed of more than 10,000 atoms, whereas mean field methods are typically limited to treating molecules containing

less than 1000 atoms.¹⁹ Multireference methods are typically restricted by the size of active spaces, which determines how many N-electron basis functions are used to expand the Hamiltonian.

Various techniques can be used to speed up the calculation, although a common feature is the introduction of intermediate quantities that reduce unnecessary repeated calculations; these techniques are mostly method dependent, and generally involve a balance between the central processing unit (CPU) resources and memory (or disk) resources. In contrast, one common technique that can be applied to all computational methods is the parallel implementation of the computational program. In this dissertation, recent progress made to improve the efficiency of large hybrid variational-perturbational multireference calculations are described.

The dissertation is organized as follows. This chapter provides an overview of traditional computational chemistry methods that are relevant to the dissertation, including Hartree–Fock, density functional theory (DFT), single reference perturbation method, single reference configuration interaction (CI), multiconfigurational self-consistent field method (MCSCF), multireference configuration interaction (MRCI), multireference perturbation theory (MRPT), and finally the basics of solid state calculations involving periodic boundary conditions. Chapter II discusses the propargyl radical system, whose excitations prove to be so difficult to predict accurately that the computationally expensive method multireference configuration interaction method including single and double excitations corrected by triple and quadruple excitations (MRCISD(TQ)) are required. Chapter III discusses the parallel implementation of the MRCISD(TQ) method. Chapter IV describes the parallelization of a widely applicable multireference perturbation theory,

i.e., the second order generalized van Vleck perturbation theory (GVVPT2) that uses many of the parallelization techniques developed for MRCISD(TQ). Chapter V describes the implementation of a spin-restricted density functional theory, which, among other uses, can be used to replace the computationally expensive MCSCF method to provide orbitals for GVVPT2 calculations. Chapter VI discusses calculation of the Zn-pthalocyanine tetrasulfonic acid adsorbed on graphene system using DFT with a plane wave basis, which provides insight into directions for extending traditional quantum chemistry techniques to the nano- and meso-scales.

Hartree–Fock

The Hartree–Fock method is the most basic *ab initio* method used in modern computational chemistry.^{2-4,19-22} The Hartree–Fock method treats electron–electron interaction in a mean field way, such that each electron in the system feels an averaged potential generated by the other $N - 1$ electrons. It is an extension of the simple product function (called the Hartree method) in that the electron wave function is represented by a Slater determinant such that the wave function is antisymmetric upon exchanges of electrons.

Without considering the nature of spin orbitals (other than orthonormality conditions), the Hartree–Fock ground state energy can be written as

$$E_0 = \langle \psi_0 | H | \psi_0 \rangle = \sum_a^N \langle \chi_a | h | \chi_a \rangle + \frac{1}{2} \sum_a^N \sum_b^N (\langle \chi_a \chi_a | \chi_b \chi_b \rangle - \langle \chi_a \chi_b | \chi_b \chi_a \rangle) \quad [1.1]$$

where a and b are spin-orbitals, and h is the one-electron operator for the kinetic energy and nucleus-electron interactions.

The best spin-orbitals should minimize the energy in the expression above, this leads to the Hartree–Fock equations for the spin orbitals

$$h(1)\chi_a(1) + \sum_{b \neq a} \left[\int d\mathbf{r}_2 |\chi_b(2)|^2 r_{12}^{-1} \right] \chi_a(1) - \sum_{b \neq a} \left[\int d\mathbf{r}_2 \chi_b^*(2) \chi_a(2) r_{12}^{-1} \right] \chi_b(1) = \varepsilon_a \chi_a(1) \quad [1.2]$$

After the definition of the Coulomb and exchange operator, the Hartree–Fock equation above can be rewritten as

$$\left[h(1) + \sum_{b \neq a} J_b(1) - \sum_{b \neq a} K_b(1) \right] \chi_a(1) = \varepsilon_a \chi_a(1) \quad [1.3]$$

from which a Fock operator can be defined as

$$f(1) = h(1) + \sum_{b \neq a} J_b(1) - \sum_{b \neq a} K_b(1) \quad [1.4]$$

All equations above use spin orbitals, thus are general for both the spin-restricted case and the spin-unrestricted case. By including conditions of spin restriction, the above equations can take different forms when expanded in spatial orbitals multiplied by spin-dependent coefficients, which will be discussed in detail in Chapter V.

Another way to look at the Hartree–Fock method is from the orbital rotation point of view.²⁰ It provides a compact way of representing orbital optimization at the Hartree–Fock level. Since the transformation of the orbital coefficient matrices are done by multiplications of unitary matrices (e.g., unitary operators expressed in a suitable basis), so that such multiplication can be written in an exponential form

$$|\kappa\rangle = \exp(-\kappa)|0\rangle \quad [1.5]$$

where κ is the anti-Hermitian one-electron operator

$$\kappa = \sum_{PQ} \kappa_{PQ} a_P^\dagger a_Q \quad [1.6]$$

Since the Hartree–Fock method uses a mean-field treatment, electron correlation effect is not considered for the electrons of the opposite spin, but somewhat included (by virtue of the Pauli Exclusion Principle) for those with the same spin. Correlation effects can be further separated into dynamic and static correlation effects. Static correlation effects come from the degeneracy and near degeneracy of multiple Slater determinants at the ground state. Since Hartree–Fock method only uses one Slater determinant, it is qualitatively wrong when such effects are present. The MCSCF method is designed primarily to treat the static correlation error by including multiple determinants in the calculation. The dynamic correlation arises from the instantaneous nature of electron interactions. Perturbation theories such as MP2 are primarily designed to capture the dynamic correlation effect. Typically, the neglect of static correlation leads to larger errors than the neglect of dynamic correlation, and the most common way to treat both types of correlation effect is to treat the static correlation first, followed by dynamic correlation correction.

Density Functional Theory

In 1964, Hohenberg and Kohn²³ proved two theorems which set the foundation of density functional theory. The existence theorem states that the external potential and thus the total energy is a unique function of electron density. The variational theorem states the electron density, with appropriate boundary conditions (i.e., N-representability), that minimizes the energy is the ground state density. This means that the complicated electronic interaction can be efficiently solved by approximating the external potential electrons feel as a mean-field. A year later, Kohn and Sham²⁴ devised a method to carry

out DFT calculations by representing electronic densities with orbitals (Eq. 1.7), retaining the exact nature of constraints for DFT. By using this method, the Schrodinger equation takes the form of Eq 1.8, usually referred to as the Kohn–Sham equation; the orbitals obtained are usually called Kohn–Sham orbitals. The one-electron Kohn–Sham Hamiltonian can be expressed as the summation of the classical non-interacting electron kinetic term, the nuclear attraction potential, the classical mean-field electronic repulsion potential, and the exchange–correlation potential which accounts for both the non-classical corrections to the electron–electron repulsion energy, and the non-classical correction to the kinetic energy deriving from the interacting nature of the electrons. Unlike the Hartree–Fock method, the Hohenberg–Kohn theorems show that DFT is an exact method. However, the exact form of the exchange correlation potential is unknown. Various approximations are used to approximate it, and the expression of this potential uniquely defines the DFT method.

$$\rho = \sum_{i=1}^N \langle \chi_i | \chi_i \rangle \quad [1.7]$$

$$h_i^{KS} \chi_i = \varepsilon_i \chi_i \quad [1.8]$$

$$h_i^{KS} = -\frac{1}{2} \nabla_i^2 - \sum_k^{nuclei} \frac{Z_k}{|r_i - r_k|} + \int \frac{\rho(r')}{|r_i - r'|} dr' + V_{XC} \quad [1.9]$$

$$V_{XC} = \frac{\delta E_{XC}}{\delta \rho} \quad [1.10]$$

$$E[\rho(r)] = \sum_i^N \left(\langle \chi_i | -\frac{1}{2} \nabla_i^2 | \chi_i \rangle - \langle \chi_i | \sum_k^{nuclei} \frac{Z_k}{|r_i - r_k|} | \chi_i \rangle + \langle \chi_i | \frac{1}{2} \int \frac{\rho(r')}{|r_i - r'|} dr' | \chi_i \rangle \right) + E_{XC}[\rho(r)] \quad [1.11]$$

The expression for exchange correlation potential is usually separated linearly into an exchange term and a correlation term. Each term is usually constructed by parameterizations. Certain DFT methods are constructed only based on physical constraints, such as obtaining the correct uniform electron gas limit. In these cases, the parameters have physical meanings and are not empirical. The X- α method²⁵ and PBE²⁶ are both of this type. Other DFT methods contain parameters that are optimized to minimize the error of certain types of data set. Typically, these methods are designed to incorporate physical constraints as well.

Based on what local characteristics the exchange correlation potential depends on (e.g., density, density gradient, kinetic energy density), most DFT methods can be assigned to a Jacob's ladder of increasing accuracy.²⁷ The first rung of the ladder is the least accurate type and is called the local density approximation (LDA), with the exchange and correlation functionals depending on the local density only. Required to obtain the correct uniform electron gas limit, the LDA exchange functional takes the form of Eq 1.12.

$$E_X^{LDA}[\rho] = -\frac{3}{4} \left(\frac{3}{\pi} \right)^{1/3} \int \rho(r)^{4/3} dr \quad [1.12]$$

LDA typically gives an error of 1% of total energy, making it impractical for chemical purposes, since the total bonding energy is of comparable magnitude. The local spin density approximation (LSDA) is a spin polarized extension of LDA; it employs both spins densities separately,

$$E_{XC}^{LSDA}[\rho_{\uparrow}, \rho_{\downarrow}] = \int \varepsilon_{XC}[\rho_{\uparrow}, \rho_{\downarrow}] \rho(r) dr \quad [1.13]$$

The second rung, generalized gradient approximation (GGA), depends on the gradient of electron density in addition to the electron density itself, and is thus considered

semi-local (in the sense of a Taylor expansion of the density). The most common way to construct GGA is to add a term related to the dimensionless reduced gradient, see Eq 1.14.

$$E_{XC}^{GGA}[\rho_{\uparrow}, \rho_{\downarrow}] = \int \varepsilon_{XC}(\rho_{\uparrow}, \rho_{\downarrow}, \nabla\rho_{\uparrow}, \nabla\rho_{\downarrow})\rho(r) dr \quad [1.14]$$

$$\varepsilon_{XC}^{GGA}[\rho(r)] = \varepsilon_{XC}^{LSDA}[\rho(r)] + \Delta\varepsilon_{XC} \left[\frac{|\nabla\rho(r)|}{\rho(r)^{4/3}} \right] \quad [1.15]$$

The third rung, meta-GGA, is constructed by considering the dependence of the Laplacians of electron density, such as TPSS,²⁸ or the Kohn–Sham orbital kinetic energy densities, such as the Minnesota functionals.^{29–32} These types of calculations are more commonly used in molecular calculations than in plane wave calculations.

The fourth rung, hyper-GGA, adds the exact exchange energy density as a local ingredient. Widely used global hybrid functionals include B3LYP,^{33–35} PBE0,³⁶ etc., whereas some other DFT methods like CAM-B3LYP³⁷ and ω B97X-D³⁸ use different parameters for Hartree–Fock exchange at different distances. Hybrid GGA methods are the most commonly used DFT methods in molecular calculations because the inclusion of the Hartree–Fock exact exchange can drastically improve the calculation accuracy without much increase of computational time. The most famous DFT method (i.e., B3LYP³³) has an expression of Eq 1.16.

$$E_{XC}^{B3LYP} = (1-a)E_X^{LSDA} + aE_X^{HF} + b\Delta E_C^B + (1-c)E_C^{LSDA} + cE_C^{LYP} \quad [1.16]$$

The fifth and last rung of Jacob’s ladder utilizes both the occupied and unoccupied Kohn–Sham orbitals. These types of functionals require large basis sets (comparable to those needed in wave function calculations) and are not yet practical for general use.

Typically, DFT methods are reliable in predicting geometry and ground state energies of molecules. The challenges reside in the calculation of reaction barriers, excited states, systems of multireference character, long-range dispersion, charge transfer systems, hydrogen bonding, strong correlation, etc. In order to treat multireference character cases, non-collinear DFT methods^{39,40} and multideterminantal DFT^{41–44} were developed over the years. Excited states can be treated by time-dependent DFT,^{45–47} real time time-dependent DFT,⁴⁸ or spin-flip DFT methods.⁴⁹ Dispersion can be treated by adding van der Waals corrections to the Kohn–Sham Hamiltonian.^{50,51}

In the area of DFT methods, it is worth pointing out that there are other variations of DFT methods that are fundamentally different from the above mentioned ones. For example, the orbital-free DFT method⁵² follows the Hohenberg–Kohn theorem without using Kohn–Sham orbitals; the DFT+U method⁵³ has an empirical parameter U to describe the electron localization, which can be important in systems like Mott insulators; various versions of density functional tight binding methods⁵⁴ solve the secular equation in self-consistent^{55,56} or non-self-consistent^{57,58} ways to treat large molecules, clusters, nanostructures, and condensed-matter systems; the recently developed machine learning DFT method^{59,60} can learn from density matrix renormalization group method data to obtain the kinetic energy as a functional of electron densities in an orbital-free manner.

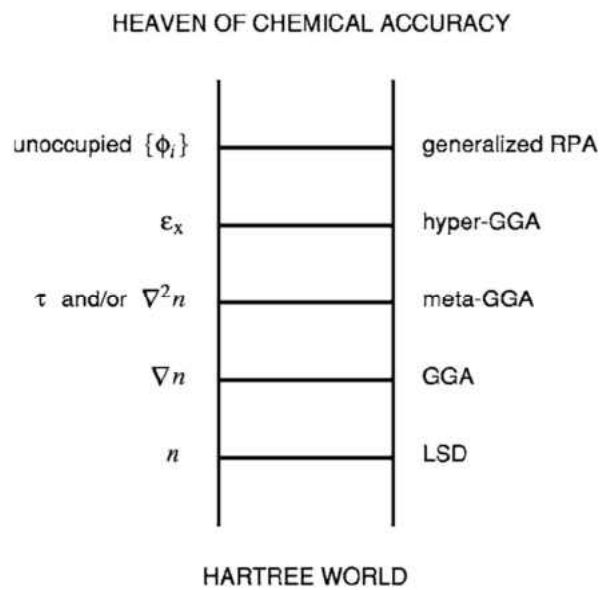


Figure 1. Jacob's ladder [Fig. 1 from Reference 27]

Single-Reference Perturbation Method

Perturbation methods are used to recover dynamic correlations. Commonly seen types of perturbation methods include the Rayleigh–Schrodinger perturbation theory and the less commonly used Brillouin–Wigner perturbation theory.⁶ In perturbation theories, the Hamiltonian H is written as the sum of two terms: one being the zero order Hamiltonian which contains the majority of the interaction H_0 , and the other being the “small” perturbation U .

$$H = H_0 + U \quad [1.17]$$

The term H_0 should be exactly solvable with eigensolutions

$$H_0 |i^{(0)}\rangle = E_i^{(0)} |i^{(0)}\rangle \quad [1.18]$$

The exact solution of the exact Hamiltonian that we look for can be expressed as

$$H|0\rangle = E|0\rangle \quad [1.19]$$

By choosing the Fock operator (*vide supra*) as the zero-order Hamiltonian in Rayleigh-Schrodinger perturbation theory, the ubiquitous Møller–Plesset perturbation theory (i.e., MPn, where n is the order of perturbation) can be constructed. It is useful to note that the Hartree–Fock energy is correct through the first order in Moller–Plesset perturbation theory. After expanding the exact solutions into summations of all orders of the perturbation results,

$$E|0\rangle = \sum_{k=0}^{\infty} |0^{(k)}\rangle \quad [1.20]$$

$$E = \sum_{k=0}^{\infty} E^{(k)} \quad [1.21]$$

the Schrodinger equation can be written as

$$(H_0 + U) \sum_{k=0}^{\infty} |0^{(k)}\rangle = \left(\sum_{k=0}^{\infty} E^{(k)} \right) \sum_{k=0}^{\infty} |0^{(k)}\rangle \quad [1.22]$$

The Rayleigh–Schrodinger perturbation theories are derived by collecting terms of the same order n

$$(H_0 + E^{(0)})|0^{(n)}\rangle = -U|0^{(n-1)}\rangle + \sum_{k=0}^{\infty} E^{(k)}|0^{(n-k)}\rangle \quad [1.23]$$

Since the inversion of $H_0 + E^{(0)}$ is well-defined for states other than the reference, the n-th order wave function correction can be written as

$$|0^{(n)}\rangle = -(H_0 + E^{(0)})^{-1} \left(-U|0^{(n-1)}\rangle + \sum_{k=0}^{\infty} E^{(k)}|0^{(n-k)}\rangle \right) \quad [1.24]$$

This relationship can be used recursively to generate the perturbation equations of higher order. Using a projection operator $P = 1 - |\mathbf{0}^{(0)}\rangle\langle\mathbf{0}^{(0)}|$ to circumvent the nonsensical self-perturbation, the low-order wave functions can be written as

$$\begin{aligned} |\mathbf{0}^{(1)}\rangle &= -P(H_0 + E^{(0)})^{-1}PU|\mathbf{0}^{(0)}\rangle \\ |\mathbf{0}^{(2)}\rangle &= -P(H_0 + E^{(0)})^{-1}P(U - E^{(1)})|\mathbf{0}^{(1)}\rangle \\ |\mathbf{0}^{(3)}\rangle &= -P(H_0 + E^{(0)})^{-1}P\left[(U - E^{(1)})|\mathbf{0}^{(2)}\rangle - E^{(2)}|\mathbf{0}^{(1)}\rangle\right] \end{aligned} \quad [1.25]$$

And their energy corrections are

$$\begin{aligned} E^{(1)} &= \langle\mathbf{0}^{(0)}|U|\mathbf{0}^{(0)}\rangle \\ E^{(2)} &= \langle\mathbf{0}^{(0)}|U|\mathbf{0}^{(1)}\rangle \\ E^{(3)} &= \langle\mathbf{0}^{(0)}|U|\mathbf{0}^{(2)}\rangle \end{aligned} \quad [1.26]$$

It can be proven that Rayleigh–Schrodinger equation obeys the so-called $2n + 1$ rule,⁶¹ meaning the n -th order wave function can give the energy of the order $2n + 1$.

Configuration Interaction

The single-reference configuration interaction method improves Hartree–Fock results by solving a variational problem that includes more Slater Determinants in the calculations. The Hartree–Fock N-electron wave function is used as the reference, and additional determinants are generated by exciting electrons from occupied orbitals into virtual orbitals. The importance of determinants is decided by variationally optimizing the total energy, while the Hartree–Fock orbitals are kept without further optimization.

$$|C\rangle = \sum_i C_i |i\rangle \quad [1.27]$$

$$\frac{\partial}{\partial C_i} \frac{\langle C|H|C\rangle}{\langle C|C\rangle} = 0 \quad [1.28]$$

This leads to the eigenvalue problem

$$\mathbf{HC} = E\mathbf{C} \quad [1.29]$$

If all possible electron configurations are included in the calculation, the CI method is referred to as full-CI. The full-CI method provides the variational limit of non-relativistic electronic structure calculations; the full-CI limit for a relativistic Hamiltonian is possible but requires additional approximations (e.g., “no pairs”). Unfortunately, the full-CI method is impossible to apply to large molecules since the number of configurations increases drastically (e.g., more than exponentially) with the system size. For a fixed number of electrons k , the number of determinants increases as n^k with the number of orbitals n . In practice, the full-CI method is rarely used except for model problems, and the truncated CI methods are used instead.

The CI methods are usually truncated based on the level of excitations. If only determinants generated from double electron excitations are included in the CI matrix, the CI method is usually referred to as CID. Truncated CI methods lose their size-extensivity, meaning the energy of the sum of separate systems A and B does not equal to the energy of a combined system A+B even though A and B are far enough apart so that they don't interact with each other. When the Hartree-Fock reference wavefunction fails qualitatively, the other determinants generated from the reference by a tractable finite number of replacements will also fail to effectively describe the excited states. Thus by

directly using Hartree–Fock orbitals without optimization, the tightly truncated CI methods are not the most effective for calculating systems with high static correlation effects. On the other hand, dynamic correlations depend more on the nodal structure and the overall shape of orbitals, so that careful orbital optimization is not necessary. The truncated CI method can capture dynamic correlation to a reasonable amount.

The CI space can be expanded in either Slater determinants or Configuration State Functions (CSFs). CSFs are linear combinations of spin-symmetry-adapted Slater determinants, and thus are more compact than determinants but more importantly guarantee that wave functions are eigenfunctions of both S^2 and S_z . For the same configuration space of a singlet, the dimension of the set of CSFs is about a quarter of that of determinants. For a full-CI expansion, the rigorous ratio of the number of spin-adapted CSFs and determinants can be calculated by⁶²

$$\frac{N_{CSF}}{N_{det}} = \frac{(2S+1)(n+1)}{(S+1+\frac{N}{2})(n+S+1-\frac{N}{2})} \quad [1.30]$$

Multiconfigurational Self-Consistent Field Theory

In some chemical systems, multiple electron configurations are important in the qualitative description. These systems usually exhibit resonance structures or have low-lying excited states. Some studies are interested in the energy of excited states instead of the ground state. Still other studies look at a reaction path, where electronic configurations change from before to after a reaction, and the relative importance of electronic configurations change (sometimes dramatically) along the reaction path. For these systems, multiple electron configurations must be included, and the orbitals need to correctly

represent each configuration without bias. This requires simultaneous optimization of the orbital coefficients and the configuration coefficients.

Following the notations from the subsections describing Hartree–Fock and CI, the MCSCF wave function can be written in the form

$$|\kappa, \mathbf{C}\rangle = \exp(-\kappa) \sum_i C_i |i\rangle \quad [1.31]$$

$$E_{MCSCF} = \min_{\kappa, \mathbf{C}} \frac{\langle \kappa, \mathbf{C} | H | \kappa, \mathbf{C} \rangle}{\langle \kappa, \mathbf{C} | \kappa, \mathbf{C} \rangle} \quad [1.32]$$

The optimization of the MCSCF function is much more difficult than that of single-reference methods. The reason is there generally are multiple local stationary points that satisfy some optimization convergence criteria, and even some that satisfy all criteria, but they may still not be the global minima or are not physical. One must investigate the nature of orbitals carefully to make sure the calculation makes sense. Another very important way to reduce this problem is in the selection of active spaces; in other words, in the selection of which orbitals and what configurations are optimized in the calculation. If certain orbitals are always doubly occupied, for example the 1s orbital of oxygen in a ground electronic state calculation of H₂O, the Hartree–Fock orbitals should be accurate enough and do not need to be further optimized or require minimal changes. Similarly, high energy virtual orbitals do not need much optimization because they are almost never occupied. Furthermore, not only is it not necessary to optimize them, but their inclusion in the active (or variable occupancy) space destabilizes a calculation. Where optimization is most valuable is in connection with the valence orbitals and low energy virtual orbitals. These orbitals and their occupation schemes define the active spaces. Moreover, and in homage

to the chemical intuition of Valence Bonds, a common rule of generating efficient active spaces is to include pairs of bonding and anti-bonding orbitals.

Active spaces can be classified as complete or incomplete, depending on whether all determinants (or CSFs) consistent with specified symmetries that can be generated from a given set of orbitals are included in the many body basis. There are two schemes in common use to select active spaces: complete active space (CAS) and restricted active space (RAS). The CAS method allows the electrons to occupy the active orbitals in all possible ways consistent with the Pauli exclusion principle and other symmetries. This can be viewed as a full-CI in the active space. The RAS method further divides the set of active orbitals into three categories RAS1, RAS2, and RAS3. The RAS1 space can be fully occupied or have a maximum of two electrons excited from the RAS1 orbitals. The RAS3 space can have a maximum of two electrons in the RAS3 orbitals. The RAS2 orbitals can host the rest of the electrons in the system. Typically, the orbitals in the RAS1 and RAS3 spaces are bonding and the corresponding anti-bonding orbitals, respectively. In our approach, active spaces can be defined based on a macroconfiguration scheme,⁶³ which is more flexible than the traditional approaches. This approach provides an easy and mathematically well-defined way to divide the orbitals into an arbitrary number of groups with arbitrary occupancies. Computationally, use of macroconfigurations leads to efficient algorithms and, of specific interest here, provides a convenient way to parallelize multireference calculations. The macroconfiguration method is described in detail in Chapter III.

Multireference Configuration Interaction Method

Multireference configuration interaction methods (MRCI) are similar to single-reference configuration interaction methods, except that more than one many-electron function is used as the reference, as opposed to Hartree–Fock. Typically, MCSCF functions from a previous calculation are used. This method can capture both static and dynamic correlation effects.

Similar to single-reference CI methods, the configuration (or CI) space in which the N-electron wavefunction is expanded is represented as antisymmetrized product functions (i.e., Slater determinants) or linear combinations of them (e.g., CSFs). The expansion coefficients over the many electron basis can be organized into a vector (referred to as the CI vector) and the integrals over the Hamiltonian operator as a matrix (called the CI matrix or simply as the Hamiltonian). The size of the CI space can reach the order of billions of CSFs or more. If the CI space is expanded in determinants, its size is usually a few times larger than expanding by CSFs. Considering the overall size of the CI matrix and the complexity of diagonalizing this matrix (even for only a few lowest eigenpairs), expanding the Hamiltonian by CSFs is usually advantageous even though programming CSF-based code is more complicated.

Like single reference CI methods, MRCI diagonalizes part of the CI matrix. Considering the dimension of CI matrices, conventional diagonalization techniques that are useful for “smaller” matrices (i.e., up to maybe 10^3 or 10^4 dimensional) cannot be applied. Luckily, we are not interested in the fully diagonalized matrix. Instead, the physical problems in which we are interested require us to only calculate a few states that have the lowest energy. In this way, the problem of diagonalizing

$$HC_i = C_i E_i \quad [1.33]$$

restricts the range of “i”, and algorithms for finding the lowest eigenpairs of large, sparse matrices can be applied. Essentially all algorithms are of the Preconditioned Conjugate Gradient variety, of which Lanczos⁶⁴ and Arnoldi⁶⁵ are the best known (for symmetric and asymmetric, respectively). For quantum chemistry problems, the eponymous variety introduced by Davidson (or more generally Davidson-Jacobi) is the most effective and the most used.⁶⁶

In the Davidson algorithm, some trial vectors C_i are selected to start the calculation. The number of trial vectors is usually around the number of eigenpairs desired. Then the matrix product $\sigma_i = HC_i$ is calculated. A matrix eigenvalue problem in a subspace can be formed by multiplying $\tilde{H}_{ij} = C_{ij}^+ \sigma_i = C_{ij}^+ HC_i$, and this subspace has the same dimension as the number of trial vectors, which is considerably smaller than the original CI matrix. By diagonalizing this submatrix $\tilde{H}_{ij} x_i = \rho_i x_i$, eigenvectors x_i and eigenvalues ρ_i can be obtained. At this point, a residual can be formed that measures how accurately the CI matrix is approximated by the submatrix, using $r_i = (H - \rho_i I)x_i$. It should be zero if the subspace perfectly approximates the CI matrix. Using this residual, a set of additional basis vectors can be generated and constrained to be orthogonal to the original one, and the next iteration can be carried out until convergence. For practical reasons, e.g., limitation of available disk space, the expanding set of basis vectors sometimes needs to be contracted into a new set of trial vectors and the whole process repeated.

In the calculation of the CI matrix, the most time-consuming step is the calculation of the matrix product $\sigma_i = HC_i$. Due to the size of the Hamiltonian matrix, storing it in

memory or even disk becomes impractical. Instead, direct CI was developed to calculate the Hamiltonian matrix on-the-fly during the diagonalization step.⁶⁷ In practice, the most efficient programs only store the trial vectors and the sigma vectors on disk. Many approaches can be used to improve the efficiency of this calculation. The most commonly seen ones for CSF-based Hamiltonians are Table-CI,^{68,69} symmetric group approach (SGA),^{70–73} unitary group approach (UGA),^{74,75} and its graphical presentation, the so-called graphical unitary group approach (GUGA).^{76,77} These methods not only provide efficient ways to arrange and label the CSFs, but also provide ways to organize the calculation steps.

Both UGA and SGA couple electrons successively; i.e., they look at the change of quantum numbers with the increase of number of electrons, and determine how to add electrons to achieve the desired (spin-)symmetry. It was shown that the UGA and SGA methods are inherently related.⁷⁸ The Yamanouchi–Kotani states often used as basis functions in SGA methods are equivalent (up to overall phase) to the Gelfand–Tsetlin states normally used as basis functions in UGA. GUGA can be implemented in various ways, with well-known codes by Brooks and Schaefer,^{79–81} Siegbahn,^{82,83} Shavitt and coworkers,⁸⁴ and Wen and coworkers^{85,86} to name a few. GUGA is regarded as arguably the most efficient approach, especially when the orbital spaces have many singly occupied orbitals and when the basis functions are limited to single and double electron excitations.

The most popular formalism of GUGA was developed by Shavitt.^{41,84,87,88} It was shown earlier that the intrinsic structure of spin-adapted CSFs can be compactly represented by a Paldus tableau.^{74,89,90} In any genealogical coupling scheme, each CSF can be thought as constructed by putting in one orbital at a time into the vacuum space. Each new orbital can be unoccupied, doubly occupied, or singly occupied with an increase or

decrease in total spin (S^2). In a Paldus tableau, the CSF can be represented by recording each step of the generation using n sets of three numbers

$$[a_i b_i c_i], (i = 1, 2, \dots, n) \quad [1.34]$$

where

$$\begin{aligned} a_i &= \frac{1}{2} N_i - S_i \\ b_i &= 2S_i \\ c_i &= i - a_i - b_i \end{aligned} \quad [1.35]$$

representing the number of coupled pairs, total spin increasing, and empty orbitals at step i . N_i and S_i are the cumulative number of electrons and total spin at step i . Following this procedure, a step number d_i can be defined to represent how to get from step i to $i + 1$.

Table 1. Definition of step numbers in DRT

| d | $\Delta a \overline{\Delta c}$ | $\Delta a \Delta c$ | ΔS | ΔN |
|----------|--------------------------------|---------------------|----------------|------------|
| 0 | 0 1 | 0 0 | 0 | 0 |
| 1 | 0 0 | 0 1 | $\frac{1}{2}$ | 1 |
| 2 | 1 1 | 1 0 | $-\frac{1}{2}$ | 1 |
| 3 | 1 0 | 1 1 | 0 | 2 |

All possible ways to generate Paldus tableaux can be collected together in tables known as distinct row tables (DRT).

Shavitt translated the DRT representation into a graph, called the Shavitt graph.⁸⁴ Each row in a Paldus tableaux is a node point in the Shavitt graph. Each arc connecting the nodes denotes one step taken (i.e., the occupancy and spin coupling of a given orbital), and the slope of the arc is related to the step number d_i . Following a set of arcs from bottom to top would generate a Paldus tableau, and thus a CSF. The number of paths from the bottom node to the top node gives the number of CSFs of the desired spin- (and often point group) symmetry. Following the Shavitt graph, it is easy to calculate the number of CSFs related to any node. By using the nodal information, the CSFs can be indexed easily. The indices are called the arc weights.

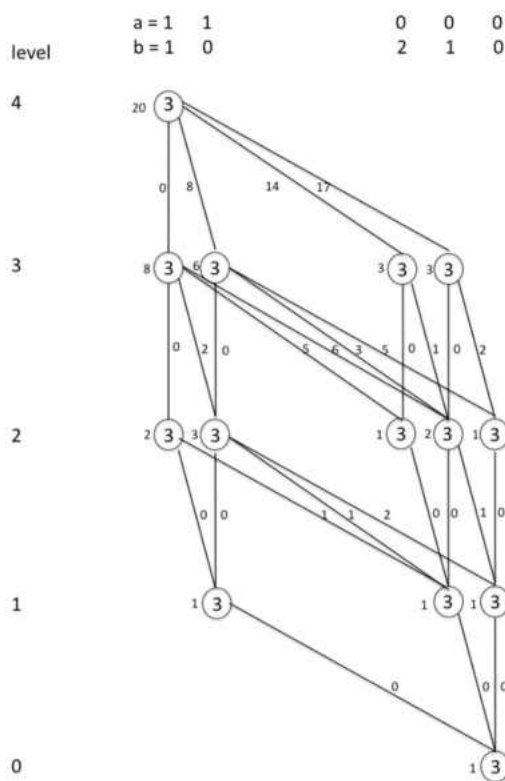


Figure 2. The Shavitt graph for the $(2, 1, 0^2)$ irreducible representation of the $U(4)$ group. This corresponds to the configurations with 3 electrons occupied in 4 orbitals, generating one electron pair and one unpaired electron. $S=1/2$, $N=3$, $n=4$.⁹¹

The GUGA method provides further ways to organize the CI calculation. Making maximal use of the nodal structures, calculations can be organized into contributions to large numbers of CSF pairs simultaneously, rather than the interaction of two CSFs at a time. Realization of this concept gives rise to loop driven,^{79,80} shape driven,^{92,93} integral driven^{82,83} and other approaches depending on particulars. This versatility can potentially help utilize varieties of computer infrastructures by distributing realizations of the GUGA formalism in different ways.

In the current version of UNDMOL, MRCI uses a configuration-driven GUGA method. In this method, the CI vectors are first arranged by configurations and then by macroconfigurations. This separates the CI vectors into two levels of coarse-grained groups. This enables the use of macroconfigurations to identify large sets of configurations that can possibly interact with each other, following the idea that the Hamiltonian operator is a two-electron operator. Subsequently, configurations can be used to screen possibly interacting CSFs, which outnumber configurations (sometimes substantially). This drastically decreases the calculation time compared to conventional CSF-based algorithms, especially when arcane incomplete model spaces are needed. One particular drawback of conventional GUGA is that the global lexical order of CSFs belonging to a single configuration is distributed diffusely. This restricts the application to some perturbation theories if explicit treatment of configurations is required. The macroconfiguration approach is also helpful in this respect. For each macroconfiguration, a DRT can be generated. Using macroconfigurations not only provides a clean and flexible way to define incomplete active spaces, but also solves the problem that the conventional Shavitt graph is inefficient in treating complicated incomplete active spaces. Conventional restricted

active spaces, which are not even particularly complicated incomplete spaces, are generated by removing the unwanted configuration state functions from the complete active space, which is not convenient in MRCI especially when triple and quadruple excitations are needed.

In addition to using macroconfigurations, the configuration-driven CI program in UNDMOL utilizes a modified DRT (mDRT), which ignores the spin information of electrons, in some stages of the calculation. In other words, cases where step number $d_i = 1$ and $d_i = 2$ are combined. This is reminiscent of the occupancy graphs that are used in high efficiency SGA programs.⁷³ The spin coupling of the CSF can be treated separately, when needed, with an abbreviated DRT that considers only the open shell part.

Multireference Perturbation Theory

A common way to approximate multireference CI methods is to treat part of the MRCI perturbatively as opposed to variationally. This gives rise to multireference perturbation theories (MRPT), although there are other ways of deriving MRPTs. MRPT methods, as do many other MR techniques, also use variational wave functions in a smaller space as reference functions. Since second-order MRPTs have seen the most development and use, MCSCF wave functions are the appropriate variational references. And since the Hamiltonian is a (one- and) two-electron operator, the first order correction generates a CI matrix with the same excitations as those found in MRCISD. However, the coefficients of the CSFs are calculated perturbatively instead. MRPTs based on simple reference spaces (e.g., complete) are often amenable to resummation techniques so that CSF coefficients are

not explicitly calculated. This option is generally not available to incomplete model space based MRPTs, like ours.

Like all perturbation methods, MRPTs separate the Hamiltonian into two parts. The dominant part is often treated variationally, usually by MCSCF (as in the case of GVVPT2) or MRCISD (in the case of MRCISD(TQ)). The perturbation part evaluates how the external space part of the Hamiltonian affects the Hamiltonian of the model space. This can be visualized by Lowdin partitioning,⁹⁴ although additional steps are generally needed and define the various different MRPTs.

The complete CI matrix can be written in the blocked form

$$\begin{pmatrix} H_{MM} & H_{MQ} \\ H_{QM} & H_{QQ} \end{pmatrix} \begin{pmatrix} C_M \\ C_Q \end{pmatrix} = E \begin{pmatrix} C_M \\ C_Q \end{pmatrix} \quad [1.36]$$

or the separate equations

$$H_{MM}|C_M\rangle + H_{MQ}|C_Q\rangle = E|C_M\rangle \quad [1.37]$$

$$H_{QM}|C_M\rangle + H_{QQ}|C_Q\rangle = E|C_Q\rangle \quad [1.38]$$

The external wave function can be expressed formally in terms of the model space wavefunction by

$$|C_Q\rangle = (E - H_{QQ})^{-1} H_{QM} |C_M\rangle \quad [1.39]$$

Eliminating the external space wave function $|C_Q\rangle$, a new effective Hamiltonian with dimension of the model space can be found

$$[H_{MM} + H_{MQ}(E - H_{QQ})^{-1}H_{QM}]|C_M\rangle = E|C_M\rangle \quad [1.40]$$

From this equation, it can be seen that if the model space Hamiltonian H_{MM} is the dominant part, then the $H_{MQ}(E - H_{QQ})^{-1}H_{QM}$ part is the perturbation.

***Ab Initio* Calculation of Solids**

Molecular electronic structure methods that expand electron orbitals by linear combinations of Gaussian or Slater type orbitals can only treat systems as large as thousands of atoms (even with severe approximations to the Hamiltonian operator). However, a solid crystal contains as many as Avogadro's number of atoms or ions, thus cannot be directly calculated using a local orbital basis. However, crystals exhibit symmetry not found in molecules. By utilizing their translational invariance, a crystal can be represented by a Bravais lattice,⁹⁵ with each point of the lattice representing a repeating unit of the crystal. With the definition of Bravais lattices and reciprocal lattices, it can be easily seen that planewaves can be used as a natural basis in the calculation of crystals.

A three-dimensional lattice is composed of all points with position vector $R = n_1\mathbf{a}_1 + n_2\mathbf{a}_2 + n_3\mathbf{a}_3$, where \mathbf{a}_1 , \mathbf{a}_2 and \mathbf{a}_3 are three non-coplanar basis vectors, and n_1 , n_2 and n_3 are integers. Basis vectors \mathbf{a}_1 , \mathbf{a}_2 , and \mathbf{a}_3 define a parallelepiped called a primitive unit cell. The length and angles between \mathbf{a}_1 , \mathbf{a}_2 , and \mathbf{a}_3 are called cell parameters.

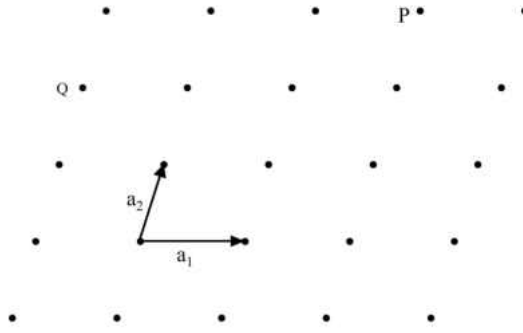


Figure 3. A two-dimensional Bravais lattice of no particular symmetry ($|\mathbf{a}_1| \neq |\mathbf{a}_2|, \theta_{\mathbf{a}_1\mathbf{a}_2} \neq 60^\circ$). Primitive vectors \mathbf{a}_1 and \mathbf{a}_2 are shown. All points are linear combinations of them with integral coefficients, for example, $P = 2\mathbf{a}_1 + 3\mathbf{a}_2$, $Q = -\mathbf{a}_1 + 2\mathbf{a}_2$.

The lattice defined by real space (or position space) vectors \mathbf{a}_1 , \mathbf{a}_2 , and \mathbf{a}_3 are called the direct lattice. Each direct lattice also admits a reciprocal lattice, constructed by the reciprocal lattice basis vectors \mathbf{b}_1 , \mathbf{b}_2 , and \mathbf{b}_3 , following the orthogonality condition

$$a_i b_j = 2\pi \cdot \delta_{ij} \quad [1.41]$$

The space in which the reciprocal lattice lives is called the reciprocal space. Due to its connection to momentum \mathbf{k} in the planewave formulation, it is also called momentum space or k space. For any \mathbf{k} vector in the reciprocal space $\mathbf{k} = k_1\mathbf{b}_1 + k_2\mathbf{b}_2 + k_3\mathbf{b}_3$, where k_1 , k_2 , and k_3 are integers, the planewave $e^{i\mathbf{k}\cdot\mathbf{r}}$ will have a periodicity of the reciprocal lattice,

$$e^{i\mathbf{k}\cdot(\mathbf{r}+\mathbf{R})} = e^{i\mathbf{k}\cdot\mathbf{r}} \quad [1.41]$$

Recognizing that the reciprocal vectors \mathbf{b}_1 , \mathbf{b}_2 , and \mathbf{b}_3 make the reciprocal lattice, unit cells can also be found in the reciprocal space. The most commonly used way to define a reciprocal unit cell is the first Brillouin zone. It is constructed by first connecting one

reciprocal lattice point to all its nearest neighbors and then letting orthogonal planes pass through their midpoints. The area enclosed by these planes is called the first Brillouin zone.

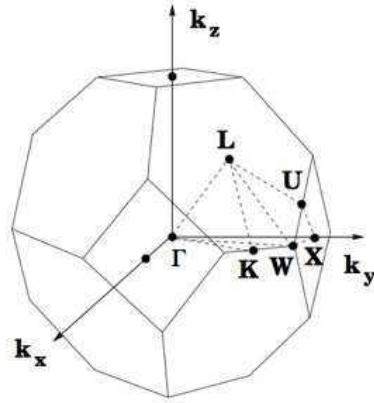


Figure 4. The first Brillouin zone of a face centered cubic crystal and the high symmetry points.⁹⁶

The correspondence relationship of real space and reciprocal space provides us a good way to represent planes in real space. A plane normal to the reciprocal lattice vector $h\mathbf{b}_1 + k\mathbf{b}_2 + l\mathbf{b}_3$ can be represented by Miller indices h, k, l .

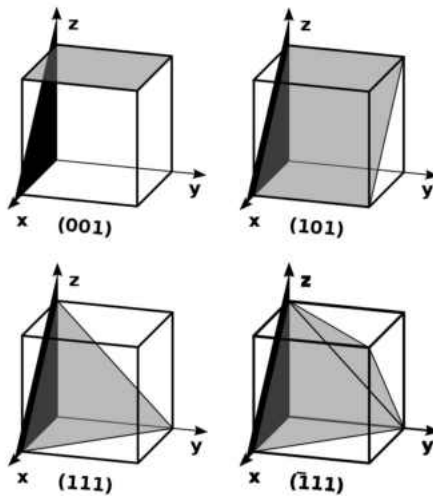


Figure 5. Miller indices in a simple cubic Bravais lattice.⁹⁶

Due to the periodicity of a crystal, the potential energy of such a crystal must be periodic as well. In other words, for all direct space lattice vectors \mathbf{R}

$$V(\mathbf{r} + \mathbf{R}) = V(\mathbf{r}) \quad [1.42]$$

Using this condition, it can be seen that the eigenstates ψ of a system with such a periodic potential can be chosen to have the form of a plane wave times a function with the periodicity of the Bravais lattice

$$\psi_{n,\mathbf{k}}(\mathbf{r}) = e^{i\mathbf{k}\cdot\mathbf{r}} u_{n,\mathbf{k}}(\mathbf{r}) \quad [1.43]$$

where

$$u_{n,\mathbf{k}}(\mathbf{r} + \mathbf{R}) = u_{n,\mathbf{k}}(\mathbf{r}) \quad [1.44]$$

This is the foundationally important Bloch's theorem in solid state physics and chemistry.

It also suggests

$$\psi_{n,\mathbf{k}}(\mathbf{r} + \mathbf{R}) = e^{i\mathbf{k}\cdot\mathbf{R}} \psi_{n,\mathbf{k}}(\mathbf{r}) \quad [1.45]$$

An equivalent way to write Bloch's theorem is

$$\psi(\mathbf{r} + \mathbf{R}) = e^{i\mathbf{k}\cdot\mathbf{R}} \psi(\mathbf{r}) \quad [1.46]$$

In this way, all cell periodic functions can be written as a linear combination of plane wave basis functions $e^{i\mathbf{G}\cdot\mathbf{r}}$, where \mathbf{G} is the wave vector of the plane wave basis function.

$$u_{n,\mathbf{k}}(\mathbf{r}) = \frac{1}{\Omega^{1/2}} \sum_{\mathbf{G}} c_{\mathbf{G}n\mathbf{k}} e^{i\mathbf{G}\cdot\mathbf{r}} \quad [1.47]$$

$$\psi_{n,\mathbf{k}}(\mathbf{r}) = \frac{1}{\Omega^{1/2}} \sum_{\mathbf{G}} c_{\mathbf{G}n\mathbf{k}} e^{i(\mathbf{G}+\mathbf{k})\cdot\mathbf{r}} \quad [1.48]$$

$$\rho(\mathbf{r}) = \sum_{\mathbf{G}} \rho_{\mathbf{G}} e^{i\mathbf{G}\cdot\mathbf{r}} \quad [1.49]$$

$$V(\mathbf{r}) = \sum_{\mathbf{G}} V_{\mathbf{G}} e^{i\mathbf{G}\cdot\mathbf{r}} \quad [1.50]$$

In practice, only those plane waves $|\mathbf{G} + \mathbf{k}|$ are included for which

$$\frac{1}{2}|\mathbf{G} + \mathbf{k}|^2 < E_{cut-off} \quad [1.51]$$

where the right hand side is called the cut-off energy, representing the maximum of the kinetic energy of the plane wave basis function used in the calculation.

Given a function $f(r)$ of the same periodicity as that of a crystal, the average value of the function can be calculated by integrating within the first Brillouin zone:

$$f(\mathbf{k}, \mathbf{k}') = \int [\psi_{\mathbf{k}'}(\mathbf{r})]^* f(\mathbf{r}) [\psi_{\mathbf{k}}(\mathbf{r})] d\mathbf{r} \quad [1.52]$$

Using the plane wave expansion above, we can expand the wave functions and the periodic function as

$$\psi_{n,\mathbf{k}}(\mathbf{r}) = e^{i\mathbf{k}\cdot\mathbf{r}} u_{n,\mathbf{k}}(\mathbf{r}) = \sum_{\mathbf{G}} c_{\mathbf{G}} e^{i(\mathbf{k}+\mathbf{G})\cdot\mathbf{r}} \quad [1.53]$$

$$\psi_{n,\mathbf{k}'}(\mathbf{r}) = e^{i\mathbf{k}'\cdot\mathbf{r}} u_{n,\mathbf{k}'}(\mathbf{r}) = \sum_{\mathbf{G}'} c_{\mathbf{G}'} e^{i(\mathbf{k}'+\mathbf{G}')\cdot\mathbf{r}} \quad [1.54]$$

$$f(\mathbf{r}) = \sum_{\mathbf{G}''} C_{\mathbf{G}''} e^{i\mathbf{G}''\cdot\mathbf{r}} \quad [1.55]$$

The integral can be evaluated using the following sum, which is non-zero only when $k = k'$

$$\begin{aligned} f(k, k') &= \sum_{\mathbf{G}} c_{\mathbf{G}} \sum_{\mathbf{G}'} c_{\mathbf{G}'} \sum_{\mathbf{G}''} c_{\mathbf{G}''} \int e^{i(\mathbf{k}+\mathbf{G}+\mathbf{G}'')\cdot\mathbf{r}} e^{i(\mathbf{k}'+\mathbf{G}')\cdot\mathbf{r}} d\mathbf{r} \\ &= \sum_{\mathbf{G}} c_{\mathbf{G}} \sum_{\mathbf{G}'} c_{\mathbf{G}'} \sum_{\mathbf{G}''} c_{\mathbf{G}''} \int e^{i(\mathbf{k}+\mathbf{G}+\mathbf{G}'')\cdot\mathbf{r}} e^{i(\mathbf{k}'+\mathbf{G}')\cdot\mathbf{r}} d\mathbf{r} = f(\mathbf{k}) \end{aligned} \quad [1.56]$$

Following the method above, a set of quantum mechanical equations can be constructed for each \mathbf{k} point. Each equation can be solved for a set of energy solutions.

Connecting the energies of high symmetry \mathbf{k} points and those of the \mathbf{k} points in between, a

band structure can be obtained. An example of the high symmetry k points in a face center cubic crystal can be found in Figure 4.

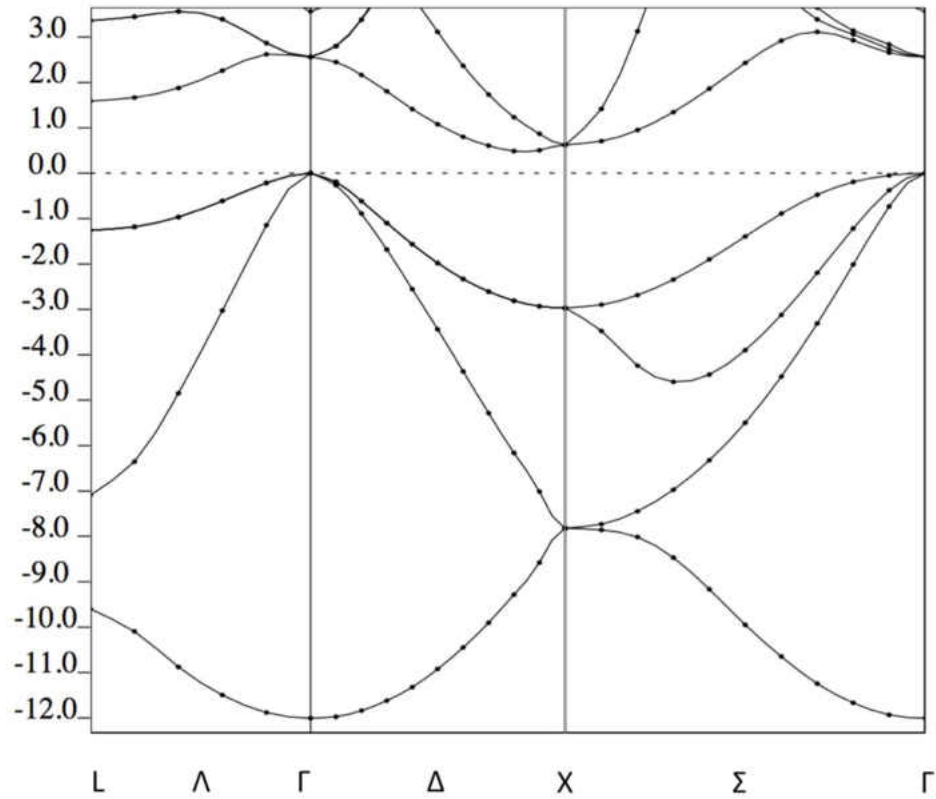


Figure 6. Band structure of face centered cubic silicon crystal. Calculation inspired by Reference 97.

CHAPTER II

THEORETICAL CALCULATIONS ON THE UV ABSORPTION OF PROPARGYL RADICAL AROUND 242 NM

Introduction

The propargyl radical (H_2CCCH) is the most stable isomer of C_3H_3 .^{98,99} Its formation and reactions have attracted much attention because it is an important precursor in the formation and growth of polycyclic aromatic hydrocarbons,¹⁰⁰ which are pollutants of concern due to the potency of their adverse health impacts. Such reactions are important not only in the studies of combustion reactions, but also planetary atmospheres and interstellar media.^{101–103} Previous spectral^{104–108} and computational^{109–112} studies were carried out to study the ionization potential and vibrational properties of propargyl. The kinetics of propargyl photodissociation was also studied using experimental^{106,113} and theoretical^{114–116} methods. Its heat of formation,¹¹⁷ electron spin resonance,¹¹⁸ bond dissociation energy¹¹⁹ and the properties of its cation¹²⁰ and anion¹²¹ forms were also studied extensively.

Propargyl radical has a strong ultraviolet (UV) absorption band at 240 nm.^{122,123} After absorption, propargyl radical can go through a photodissociation process and break down into $\text{HCCCH} + \text{H}$, $c\text{-C}_3\text{H}_2 + \text{H}$, $\text{CCCH}_2 + \text{H}$, or $\text{C}_3\text{H} + \text{H}_2$.^{118,124} (See Figure 7) It was shown that at 240 nm the majority of propargyl radicals go through the $\text{HCCCH} + \text{H}$ channel.¹¹⁵ However, not all dissociation paths were observed in all experiments, depending on the precursors used to obtain the radicals. Based on MCSCF calculations,

the 240 nm peak was initially assigned to be the $1^2B_1 \rightarrow 3^2B_1$ transition with a single electron excited from the $\pi(b_2)$ into the $\pi^*(b_2)$ orbital.¹²³ Einfeld^{125,126} performed more extensive MRCISD+Q calculations and claimed that the only transition of propargyl radical in the 240 nm region is the $1^2B_1 \rightarrow 2^2B_2$ dipole-forbidden transition. Because this transition cannot produce a strong peak, he concluded that that peak must come from another species. After subsequent experimental studies, similar results were obtained no matter how propargyl was prepared, while the peaks predicted by Einfeld were never found. The consensus from experimental studies is that it is indeed propargyl radicals that are responsible for the peak at 240 nm.^{122,127,128} Moreover, it is generally believed that the original assignment $1^2B_1 \rightarrow 3^2B_1$ was correct. The conundrum is that there is no theoretical calculation that matches this result within 10 kcal/mol, including the original MCSCF calculation.

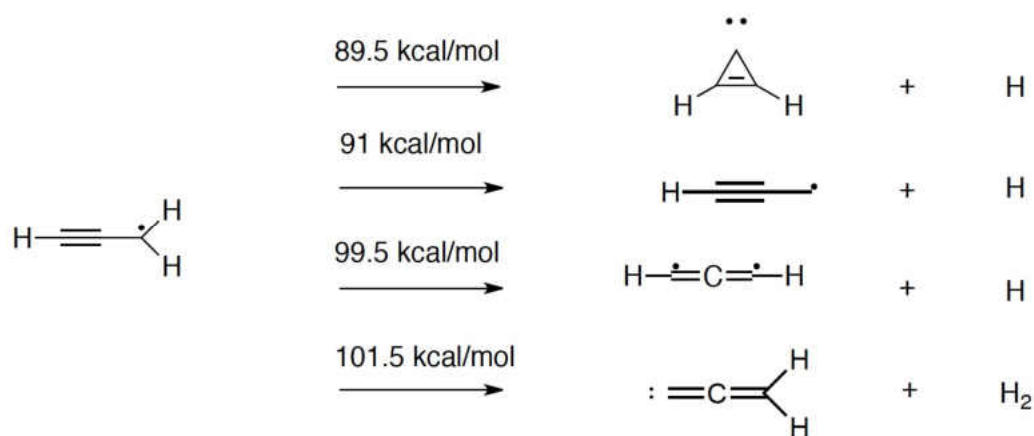


Figure 7. The most important unimolecular reaction channels for the propargyl radical together with the heats of reaction.¹¹³

We report and analyze the results of the most complete description of the electronic structure of the low-lying states of propargyl to date. The MRCISD(TQ) method,^{129,130} which is a multireference CI method that includes all single and double excited configurations variationally and the contributions of the triple and quadruple excitations perturbatively, was used. Also see Chapter III of this dissertation for additional information about MRCISD(TQ). Our implementation of MRCISD(TQ) is with uncontracted singly and doubly excited CSFs, so that full flexibility of the excited configuration is retained. The inclusion of triple and quadruple excitations not only reduces the size extensivity error but also includes correlation for states that are not well-represented qualitatively using a valence active space (e.g., Rydberg states). MRCISD(TQ) is free of “intruder states” problems, and allows for simultaneous calculations of several electronic states of the same space and spin symmetry. To further understand the electronic structure of the propargyl radical, we also carried out calculations with multireference perturbation methods GVVPT2^{9,131} and GVVPT3,¹³² both of which build dynamic correlation upon an MCSCF description of the static correlation and determination of orbitals.

The rest of the chapter is organized as follows. In the Methods section, we begin a description of the calculation methods and the active spaces used in all calculations. The next section reports out results and discussions, and the Rydberg character is analyzed. We also present here our results calculated by MRCISD, MRCISD(TQ), GVVPT2, and GVVPT3, as well as the effect of active spaces on GVVPT2 calculations. Finally, our conclusions are given in the last section.

Methods

MRCISD(TQ)

The MRCISD(TQ) method used in this study, also referred to as the nR-MRCISD(TQ) method, was developed in our group.¹²⁹ It can simultaneously calculate the energies of multiple low-energy states, as opposed to single-state methods, such as most internally contracted methods and the original MRCISD(TQ) method¹³⁰ developed in our group. As the nR-MRCISD(TQ) method is described in detail in Chapter III, we only mention here that only one iteration of this method is used in this study, because it has been shown that the subsequent iterations do not improve the calculation results much.¹²⁹

Rydberg orbitals and Rydberg states

In this work, we refer to molecular orbitals that are dominated by atomic orbitals with higher principle quantum numbers than those of valence orbitals as Rydberg orbitals. For example, the 3s and 3p orbitals of a carbon atom would contribute to Rydberg orbitals. More precisely, the Rydberg orbitals in this work are determined based on the size of isodensity surfaces of the orbitals and their nodal structures.

Physically speaking, Rydberg states are electronic states in which an electron is excited into a Rydberg orbital. However, in electronic structure calculations, it is possible to obtain a Rydberg state without the involvement Rydberg orbitals. This can be done by having multiple configurations that have high energy orbitals occupied. Since the electron distribution in Rydberg states is in general much more diffuse than valence states, this is used as the main character used in this work to distinguish Rydberg states. Another criterion used is the basis set dependency of Rydberg states. The detail is presented in the results and discussion section.

Computational theories used in the calculations of propargyl radical

It was shown in previous studies that geometries optimized from B3LYP calculations are more reliable than those from MCSCF ones.¹³³ Due to the computational cost of MRCISD, the geometry of propargyl radical was optimized using DFT with the B3LYP functional using the aug-cc-pVTZ(AVTZ)¹³⁴ basis set. MRCISD(TQ) calculations were performed for the two lowest A₁ states, the four lowest B₁ states, and the three lowest B₂ states. All states are weighted equally in each calculation. All MRCISD and MRCISD(TQ) calculations are performed with the AVTZ basis set. The molecular orbitals used in MRCISD and MRCISD(TQ) calculations were obtained from MCSCF calculations: the frozen core space always contained seven a₁ orbitals and one b₂ orbital, which are the 1s electrons of carbons and the σ -type backbone of the structure; the active spaces of the B₁ and B₂ states had five electrons occupying three b₁ orbitals and two b₂ orbitals in a complete active space manner, all of which are valence type π orbitals; whereas the A₁ states calculations used a macroconfiguration⁶³ approach that confined four electrons in those orbitals and one electron in a group of active orbitals composed of two diffuse a₁ orbitals. The MRCISD and MRCISD(TQ) calculations used the same active space configurations and correlated all but the three lowest a₁ orbitals of the MCSCF in the frozen core; i.e., the remaining higher lying four a₁ and one b₂ orbitals were placed into the active core space.

Similar complete active spaces are used in GVVPT2 and GVVPT3 calculations. The lowest A₁ and A₂ states were calculated with a CAS containing one a₁ Rydberg-like orbital, three b₁ orbitals, and two b₂ orbitals; the four B₁ states had a CAS composed of four b₁ orbitals and two b₂ orbitals, where the third b₁ orbital is Rydberg-like; the two B₂

states had three b_1 orbitals and two b_2 orbitals in the CAS. Similar to the MRCISD(TQ) calculations, GVVPT2 and GVVPT3 calculations had three a_1 orbitals in the frozen core, and four a_1 orbitals and one b_2 orbital in the active core, whereas the CASSCF calculations that these calculations were based on had them all in the frozen core.

Table 2. Active spaces and electron occupations used in the calculations.

| | | A1 | A2 | B1 | B2 |
|------------------------|------|--------------------------------|--------------------------------|--------------------------------|-------------------------------|
| MRCISD & MRCISD(TQ) | AOG1 | $(1b_12b_13b_12b_23b_2)^4$ | | $(1b_12b_13b_12b_23b_2)^5$ | $(1b_12b_13b_12b_23b_2)^5$ |
| | AOG2 | $(8a_19a_1)^1$ | | | |
| GVVPT2 & GVVPT3 | CAS | $(8a_11b_12b_13b_12b_23b_2)^5$ | $(8a_11b_12b_13b_12b_23b_2)^5$ | $(1b_12b_13b_14b_12b_23b_2)^5$ | $(1b_12b_13b_12b_23b_2)^5$ |
| GVVPT2, 2- level | AOG1 | $(4a_15a_16a_17a_11b_1)^{10}$ | $(4a_15a_16a_17a_11b_1)^{10}$ | $(4a_15a_16a_17a_11b_1)^{10}$ | $(4a_15a_16a_17a_11b_1)^{10}$ |
| | AOG2 | $(8a_11b_12b_13b_12b_23b_2)^5$ | $(8a_11b_12b_13b_12b_23b_2)^5$ | $(1b_12b_13b_14b_12b_23b_2)^5$ | $(1b_12b_13b_12b_23b_2)^5$ |
| GVVPT2, 3- level | RAS1 | $(4a_15a_16a_17a_11b_1)^{10}$ | $(4a_15a_16a_17a_11b_1)^{10}$ | $(4a_15a_16a_17a_11b_1)^{10}$ | $(4a_15a_16a_17a_11b_1)^{10}$ |
| | RAS2 | $(8a_11b_12b_13b_12b_23b_2)^5$ | $(8a_11b_12b_13b_12b_23b_2)^5$ | $(1b_12b_13b_14b_12b_23b_2)^5$ | $(1b_12b_13b_12b_23b_2)^5$ |
| | RAS3 | $(9a_110a_112a_12a_14b_1)^0$ | $(9a_110a_112a_12a_14b_1)^0$ | $(8a_19a_110a_111a_14b_1)^0$ | $(8a_19a_110a_111a_14b_1)^0$ |

Calculations were performed using AVTZ, aug-cc-pCVTZ(ACVTZ)¹³⁵ and aug-cc-pVQZ(AVQZ)¹³⁴ basis sets. The AVTZ and AVQZ results allowed extrapolation to the complete basis set (CBS) limit. The static and dynamic correlations were extrapolated separately. The former used the MCSCF energy and extrapolated based on the exponential scheme:^{136,137}

$$E_X^{MCSCF} = E_{\text{lim}}^{MCSCF} + B \exp(-\alpha X), \quad [2.1]$$

with B being the fitting parameter and $\alpha = 1.63$, as suggested by Halkier et al.,¹³⁸ tested by our research group.^{139–141} The dynamic correlation energies were defined as the differences between the larger variational or perturbation theory results and the MCSCF ones, and they were extrapolated based on the extrapolation scheme proposed by Schwartz et al.,¹⁴² Halkier et al.¹⁴³ and Helgaker et al.¹⁴⁴

$$E_X^{corr} = E_{\text{lim}}^{corr} + AX^{-3}, \quad [2.2]$$

where A is the fitting parameter.

To further investigate the effect of active spaces on the calculations, GVVPT2 calculations were also performed with incomplete active space methods achieved by extended macroconfiguration methods. The 3-level active space calculations used a RAS-type arrangement with RAS1 including four a_1 and one b_2 type orbitals that were originally in the active core space, RAS2 being the original CAS, and RAS3 being the corresponding anti-bonding orbitals of RAS1. Each RAS level allowed for a maximum of two electrons/holes. The 2-level active space calculations only allowed electrons to occupy the RAS1 and RAS2 spaces with single and double excitations in between. Both incomplete

active space schemes include extra correlation by including extra CSFs. The 2-level active space calculations only included extra core-valence interactions, whereas the 3-level active space calculations included extra correlation from virtual orbitals.

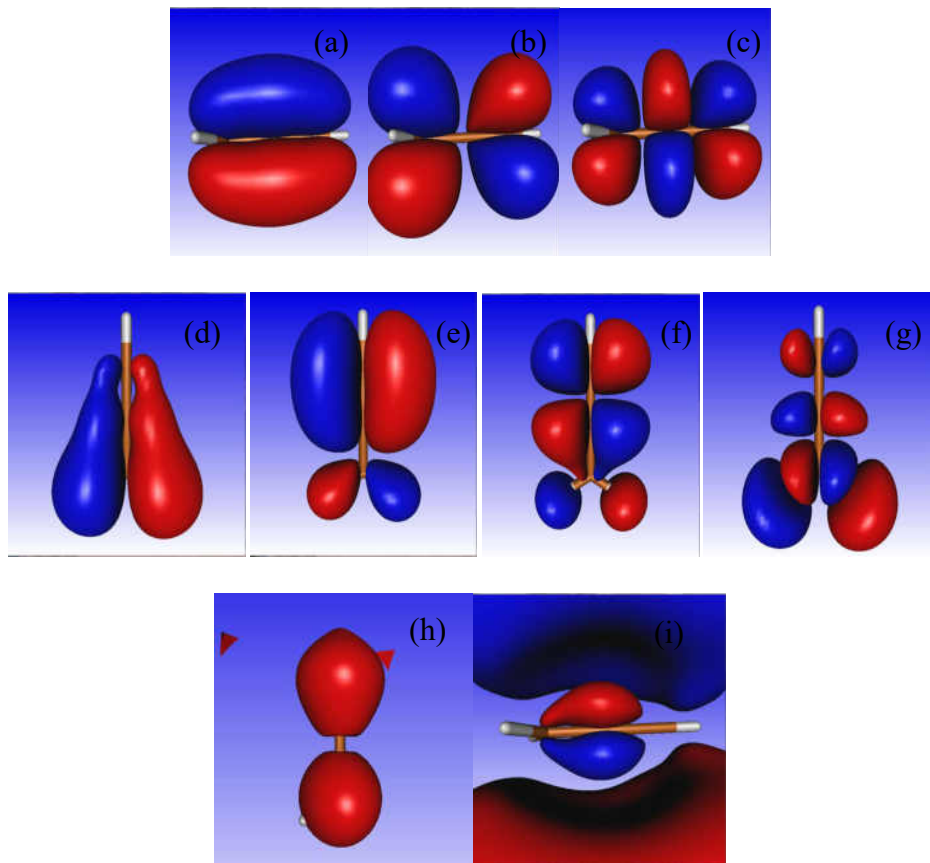


Figure 8. (a–c) b_1 valence orbitals. (d–g) b_2 valence orbitals. $1b_2$ is treated as a core orbital except in the extended calculations, while $2b_2$ and $3b_2$ are in the active space. (g) is always in the virtual space. (h) $8a_1$ Rydberg orbital included in the calculations of A_1 and A_2 states. (i) b_1 Rydberg orbital included in B_1 state calculations.

Results and discussions

It can be seen from Table 3 that the geometries obtained from B3LYP calculations agree reasonably well with previous calculations and were the precise geometry used in this study. The DFT results were obtained with the AVTZ basis set. The biggest difference

lies in the length of the CC single bond, which B3LYP slightly underestimates compared with the others. We also performed a geometry optimization with GVVPT2, and the result agrees very well with CCSD(T*)-F12 calculation, and note that the B3LYP geometry is fairly similar to it. We do not expect large differences to be induced by using the B3LYP geometry.

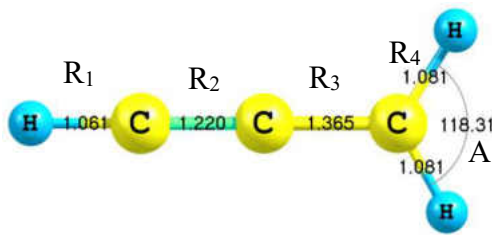


Figure 9. Equilibrium structure of propargyl radical optimized by B3LYP/AVTZ.

Table 3. Geometry parameters obtained from current and previous calculations. (In angstroms and degrees)

| | R ₁ | R ₂ | R ₃ | R ₄ | A |
|---------------------------------|----------------|----------------|----------------|----------------|-------|
| B3LYP/AVTZ | 1.061 | 1.220 | 1.365 | 1.081 | 118.3 |
| RCCSD(T)/AVTZ ¹⁰⁹ | 1.064 | 1.228 | 1.382 | 1.081 | 119.1 |
| GVVPT2/AVTZ | 1.060 | 1.227 | 1.374 | 1.078 | 119.0 |
| CCSD(T*)-F12a/VQZ ²⁸ | 1.063 | 1.225 | 1.377 | 1.080 | 119.1 |

Rydberg orbital analysis with MCSCF

Based on the MCSCF calculations reported herein and additional attempts, it was observed that MCSCF descriptions of higher lying B₁ or B₂ states do not produce heavily occupied Rydberg-orbitals. These states were best obtained if they are not heavily weighted during the MCSCF optimization. MCSCF calculations also suggest that the third and fourth

B₁ states are nearly degenerate (separated by 1.5 kcal/mol). However, this disagrees with all our higher-level calculations, which predict an energy difference of at least 7 kcal/mol with the opposite order. Not surprisingly, it was found that MCSCF energies are not reliable for Rydberg states. We also alert the reader that the states are labeled according to the energy predicted by higher level method, in order to be consistent throughout the entire paper.

Although the MCSCF energies cannot be trusted for quantitative results, it seems that qualitative understanding of states that have Rydberg character can be obtained. It can be seen from the MCSCF calculations the third B₁ state is qualitatively described by an electron excitation from the second b₂ π bonding orbital into the third b₂ π* anti-bonding orbital, and that the Rydberg-like third b₁ orbital is occupied in the fourth B₁ state. The average distance of electrons to the C-C-C-H axis was calculated to elucidate the Rydberg characters of the states. It can be seen from Table 5 that this distance is dramatically larger in the first A₁, first A₂, and fourth B₁ states, corroborating their Rydberg character.

Table 4. Main configurations of the excited states.

| | Main configuration |
|-----------------------|---|
| 1A₁ | 8a ₁ ⁽¹⁾ 1b ₁ ⁽²⁾ 2b ₂ ⁽²⁾ |
| 1A₂ | 8a ₁ ⁽¹⁾ 1b ₁ ⁽²⁾ 2b ₁ ⁽¹⁾ 2b ₂ ⁽¹⁾ |
| 1B₁ | 1b ₁ ⁽²⁾ 2b ₁ ⁽¹⁾ 2b ₂ ⁽²⁾ |
| 2B₁ | 1b ₁ ⁽¹⁾ 2b ₁ ⁽²⁾ 2b ₂ ⁽²⁾ |
| 3B₁ | 1b ₁ ⁽²⁾ 2b ₁ ⁽¹⁾ 2b ₂ ⁽¹⁾ 3b ₂ ⁽¹⁾ |
| 4B₁ | 1b ₁ ⁽²⁾ 2b ₁ ⁽⁰⁾ 3b ₁ ⁽¹⁾ 2b ₂ ⁽²⁾ |
| 1B₁ | 1b ₁ ⁽²⁾ 2b ₁ ⁽²⁾ 2b ₂ ⁽¹⁾ |
| 2B₁ | 1b ₁ ⁽²⁾ 2b ₁ ⁽⁰⁾ 2b ₂ ⁽²⁾ 3b ₂ ⁽¹⁾ |

Table 5. Average distance of electrons to the C-C-C-H axis (Bohr).

| | 1A₁ | 1A₂ | 1B₁ | 2B₁ | 3B₁ | 4B₁ | 1B₂ | 2B₂ |
|--------------------------------|-----------------------|-----------------------|-----------------------|-----------------------|-----------------------|-----------------------|-----------------------|-----------------------|
| Average distance (Bohr) | 8.68 | 8.87 | 6.19 | 6.17 | 6.55 | 8.28 | 6.28 | 6.34 |

MRCISD(TQ) and Rydberg states

Because the singles and doubles subspaces (and of course the reference) are treated variationally, the MRCISD(TQ) method can include the effect of Rydberg orbitals perturbatively even though they are not in the active space. With this method, a conventional valence-like active space can be used while accounting for the effect of Rydberg orbitals, should they be important. It is useful to recall that, in general, Rydberg states have relatively small correlation energy (e.g., large spatial extent) so that perturbative treatment should be efficacious once they are included in the variational space. In test studies, this was indeed found to be the case numerically.¹²⁹ The MRCISD(TQ) calculation results for the A₁, B₁, and B₂ states are listed in Table 6 together with MRCISD results. From these calculations, we can see MRCISD and MRCISD(TQ) are similar, with the largest deviations, not surprisingly, occurring for the most high-lying B₁ state. This means the correlations are mostly captured by MRCISD and the approximations made in the MRCISD(TQ) method can be expected to be valid. Our results agree with Eisfeld's that the dipole forbidden $1^2B_1 \rightarrow 2^2B_2$ transition is located around 242 nm. However, our calculations identify another, hitherto not discussed, transition in the vicinity: the dipole allowed transition $1^2B_1 \rightarrow 1^2A_1$ is also within 0.2 eV error of the experimental value. This suggests that the 242 nm absorption is very likely the vertical excitation from the ground state to the Rydberg-like A₁ state. It is worth noting that to our knowledge, Eisfeld¹²⁵ is the

only one that considered the possibility of excitations to A_1 states, but the active spaces of choice are very different from ours.

Table 6. MRCISD(TQ) and MRCISD calculation results.

| | MRCISD(TQ)/AVTZ | | MRCISD/AVTZ | |
|---------------------------|-----------------|-------|-------------|-------|
| | eV | nm | eV | nm |
| 1B ₁ | 0 | | 0 | |
| 1B ₂ | 3.461 | 358.2 | 3.588 | 345.6 |
| 2B ₁ | 4.080 | 303.9 | 4.120 | 300.9 |
| 2B ₂ | 5.086 | 243.8 | 5.220 | 237.5 |
| 1A ₁ | 5.325 | 232.8 | 5.162 | 240.2 |
| 3B ₁ | 6.078 | 204.0 | 6.126 | 202.4 |
| 4B ₁ | 6.882 | 180.2 | 7.146 | 173.5 |
| 3B ₂ | 7.755 | 159.9 | 7.822 | 158.5 |
| Experiment ¹²³ | 5.123 | 242 | 5.123 | 242 |

GVVPT2 and GVVPT3 results

The GVVPT2 and GVVPT3 calculations were performed using various basis sets and choices of active spaces, and the results are summarized in Table 7. Judging from the calculations using the ACVTZ basis set, the inclusion of core-valence correlation does not have any significant impact. The results are different by 0.004 eV or less for either GVVPT2 or GVVPT3. This might be expected because the Rydberg character of states, which is critical to the description of this system, is much more strongly affected by virtual orbitals than by core orbitals. It is also evident that the differences between AVTZ and AVQZ non-Rydberg states are extremely small in both GVVPT2 and GVVPT3 calculations, whereas the Rydberg states tend to have larger basis set effect, with GVVPT2 more so than GVVPT3. In the case of Rydberg states 1A₁, 1A₂ and 4B₁, larger basis sets tend to change GVVPT2 and GVVPT3 energies in opposite directions. We believe this is

another indicator of their Rydberg character. This behavior is also evident in the $3B_1$ state, which is a non-Rydberg state based on the MCSCF calculation. Since the GVVPT2 and GVVPT3 calculations are more reliable than MCSCF, we believe the $3B_1$ state may also have some Rydberg character.

Table 7. Basis set effect of GVVPT2 and GVVPT3 calculations.

| nm | GVVPT2 | | | | GVVPT3 | | | |
|-----------------|--------|--------|-------|-------|--------|--------|-------|-------|
| | /AVTZ | /ACVTZ | /AVQZ | /CBS | /AVTZ | /ACVTZ | /AVQZ | /CBS |
| 1B ₁ | - | - | - | - | - | - | - | - |
| 1B ₂ | 338.2 | 338.3 | 336.4 | 334.8 | 333.9 | 334.1 | 334.6 | 334.8 |
| 2B ₁ | 311.8 | 311.9 | 311.8 | 311.8 | 292.2 | 292.1 | 291.2 | 290.4 |
| 2B ₂ | 236.3 | 236.3 | 235.5 | 234.8 | 231.6 | 231.7 | 231.7 | 231.6 |
| 1A ₁ | 214.1 | 214.0 | 211.8 | 209.9 | 240.6 | 240.7 | 241.0 | 241.1 |
| 3B ₁ | 198.2 | 198.0 | 200.7 | 201.1 | 201.4 | 201.5 | 199.8 | 197.1 |
| 4B ₁ | 180.6 | 180.6 | 175.0 | 121.1 | 191.6 | 191.6 | 195.8 | 198.9 |
| 1A ₂ | 157.2 | 157.2 | 155.9 | 154.8 | 167.8 | 167.9 | 167.9 | 167.7 |
| eV | GVVPT2 | | | | GVVPT3 | | | |
| | /AVTZ | /ACVTZ | /AVQZ | /CBS | /AVTZ | /ACVTZ | /AVQZ | /CBS |
| 1B ₁ | 0 | 0 | 0 | 0 | 0 | 0 | 0 | 0 |
| 1B ₂ | 3.666 | 3.665 | 3.685 | 3.703 | 3.713 | 3.711 | 3.705 | 3.703 |
| 2B ₁ | 3.976 | 3.975 | 3.976 | 3.976 | 4.243 | 4.244 | 4.258 | 4.270 |
| 2B ₂ | 5.246 | 5.246 | 5.265 | 5.281 | 5.352 | 5.352 | 5.352 | 5.353 |
| 1A ₁ | 5.791 | 5.793 | 5.855 | 5.907 | 5.153 | 5.150 | 5.144 | 5.142 |
| 3B ₁ | 6.257 | 6.261 | 6.177 | 6.166 | 6.155 | 6.152 | 6.205 | 6.290 |
| 4B ₁ | 6.866 | 6.866 | 7.083 | 7.245 | 6.470 | 6.471 | 6.331 | 6.234 |
| 1A ₂ | 7.887 | 7.888 | 7.952 | 8.007 | 7.387 | 7.384 | 7.386 | 7.393 |

It can be seen from Table 8 that GVVPT3 can almost reproduce the results obtained from MRCISD(TQ) and MRCISD, with an error of less than 0.06 eV from the MRCISD(TQ) results, while GVVPT2, with the same active spaces, is only accurate to less than 0.04 eV for non-Rydberg states, and to 0.1 eV for Rydberg states. Similar to all results reported in the literature,^{109,111,123,125} the energy of the non-Rydberg $3B_1$ state is around 200

nm, which is too high to be the absorption in question; the $2B_2$ state is at the correct energy level, but since this transition is dipole forbidden it shouldn't result in a strong UV peak. Our results also show that the Rydberg state $4B_1$ is close to the $3B_1$ state in energy. Other calculations show that including the $4B_1$ state into our calculation does not have a great effect on the accuracy of $3B_1$ state calculation.

The 2-level active space calculations were performed by putting the σ bonding orbitals in a macroconfiguration in the active space, allowing a maximum of two electrons to be excited to the original CAS. These results showed changes of energies of less than 0.15 eV, which is less than the improvement induced by changing 2-level GVVPT2 to 3-level. This improvement exhibits no significant differences between Rydberg and non-Rydberg states. These results are consistent with the calculations with core-valence basis set calculations in Table 7. Both of these two calculations only improve core-valence electronic interactions, and both results show that this interaction is not as critical as the valence-virtual correlation for our system.

In the 3-level active space calculations, anti-bonding σ orbitals are included in an additional macroconfiguration (RAS3), allowing a maximum occupancy of two electrons. This largely improves the results from 2-level GVVPT2 calculations, particularly for the Rydberg states where the improvements can be as large as 0.32 eV in the case of the first A_1 state. When comparing lower level method with higher level ones, the largest differences almost always involve the Rydberg states. For instance, comparing GVVPT2/CAS with GVVPT2/3-level calculations, the energy differences for Rydberg states are larger than 0.13 eV; GVVPT2/CAS with GVVPT3 are larger than 0.27 eV; GVVPT2/2-level with GVVPT2/3-level are larger than 0.08 eV; and any method with

MRCISD and MRCISD(TQ) are typically larger than 0.2 eV. This suggests that the inclusion of the correlation introduced by virtual orbital is of critical importance in the propargyl system. We can also see from the calculations that GVVPT2 calculations with small active spaces are not reliable to characterize Rydberg states. Expanding the active space to include more virtual orbitals can be helpful. In some cases, GVVPT3 can help successfully correct the correlation with a small active space.

Table 8. GVVPT3 and extended GVVPT2 in AVTZ basis set results.

| nm | Dipole Allowed Transition? | GVVPT2/CAS | GVVPT2/2-lvl | GVVPT2/3-lvl | GVVPT3 | MRCISD | MRCISD(TQ) |
|-----------------|----------------------------------|------------|--------------|--------------|--------|--------|------------|
| 1B ₁ | | - | - | - | - | - | - |
| 1B ₂ | No | 338.2 | 350.8 | 351.0 | 333.9 | 345.6 | 358.2 |
| 2B ₁ | Yes | 311.8 | 313.3 | 313.5 | 292.2 | 303.9 | 303.9 |
| 2B ₂ | No | 236.3 | 236.5 | 236.6 | 231.6 | 237.5 | 243.7 |
| 1A ₁ | Yes | 214.1 | 217.5 | 223.1 | 240.6 | 240.2 | 232.8 |
| 3B ₁ | Yes | 198.2 | 201.4 | 201.5 | 201.4 | 202.4 | 204.0 |
| 4B ₁ | Yes | 180.6 | 179.4 | 179.5 | 191.6 | 173.5 | 180.2 |
| 1A ₂ | Yes | 157.2 | 160.2 | 162.5 | 167.8 | | |
| eV | Dipole Allowed Transition? | GVVPT2/CAS | GVVPT2/2-lvl | GVVPT2/3-lvl | GVVPT3 | MRCISD | MRCISD(TQ) |
| 1B ₁ | | 0 | 0 | 0 | 0 | 0 | 0 |
| 1B ₂ | No | 3.666 | 3.534 | 3.585 | 3.713 | 3.588 | 3.461 |
| 2B ₁ | Yes | 3.976 | 3.957 | 4.044 | 4.243 | 4.120 | 4.080 |
| 2B ₂ | No | 5.246 | 5.243 | 5.161 | 5.352 | 5.220 | 5.086 |
| 1A ₁ | Yes | 5.791 | 5.699 | 5.557 | 5.153 | 5.162 | 5.325 |
| 3B ₁ | Yes | 6.257 | 6.157 | 6.125 | 6.155 | 6.126 | 6.078 |
| 4B ₁ | Yes | 6.866 | 6.911 | 6.589 | 6.470 | 7.146 | 6.882 |
| 1A ₂ | Yes | 7.887 | 7.741 | 7.630 | 7.387 | | |

Conclusions

Based on the MRCISD(TQ), MRCISD, and GVVPT3 studies on the electronic states of propargyl radical, we conclude that the vertical excitation from the ground B_1 state to the Rydberg-like first A_1 excited state is responsible for the strong absorption band around 242 nm observed in experiments. We also show that the calculations performed before ours on non-Rydberg states are generally correct. However, our study has included a more accurate description of electronic structure, using MRCISD(TQ), than had previously been applied to this molecule, capturing the Rydberg character of the excitation around 240 nm. These calculations were performed with the generally reliable aug-cc-pVTZ basis. It is notable that these calculations involved considerations of 32 to 93 million CSFs at the MRCISD level with 1.6 to 4.5 trillion CSFs with inclusion of triple and quadruple excitations, and are easily the largest calculation to date using MRCISD(TQ). It is also worth noting that the calculations were performed on a single workstation. GVVPT2 calculations with small active spaces are not reliable to characterize Rydberg states. Expanding the active space to include more virtual orbitals can be helpful. In some cases, GVVPT3 can help successfully correct the correlation even with a small active space. Both MRCISD and MRCISD(TQ) could recover the Rydberg character even though the Rydberg orbitals are not considered explicitly. When the Rydberg orbitals are included, GVVPT3 results are within reasonable errors to the MRCISD and MRCISD(TQ) results.

CHAPTER III.

PARALLELIZATION OF TRIPLE AND QUADRUPLE PERTURBATION CORRECTIONS TO MULTIREFERENCE CISD

Introduction

Multireference variational methods are widely regarded as one of the most accurate methods in computational chemistry, especially when entire potential energy surfaces (PESs) and/or excited electronic states are of interest. The inclusion of large numbers of configuration state functions can correctly capture a large amount of both the dynamical and static correlation effects, giving highly accurate results. Moreover, such calculations are able to address several electronic states in a single run. Unfortunately, the number of CSFs (or determinants) increases rapidly (in fact, more than exponentially) with excitation level, and the method is not strictly size-extensive (although the size-extensivity errors are generally smaller than other sources of error). In previous work,^{129,130} it was shown that fully variational considerations of reference functions and single and double excitations, and perturbative treatments of triple and quadruple excitations provides highly accurate results. Moreover, the inclusion of triple and quadruple (TQ) perturbation added to multireference configuration interaction with single and double excitation method (MRCISD), can largely eliminate the size-extensivity error in singles and doubles configuration interaction methods. Although the method has not yet been used for “production,” it is to be expected (and calculations on pilot systems confirmed) that this

method is particularly appropriate for application to excited states and highly multireference systems (such as multi-radicals) with delocalized electrons. This method is particularly helpful if qualitatively reliable reference functions are difficult to obtain. In these cases, a large number of CSFs is typically necessary, but variational determination of all coefficients is not.

MRCISD(TQ) based on uncontracted CI is a very expensive method, since all many-electron basis functions in the singles and doubles subspace would need to be dressed. Various methods have been used to speed up the calculation. By using GUGA to organize the CSFs^{80,129} instead of Table-CI, large increases in the efficiency of evaluating the Hamiltonian matrix elements can be realized. The use of symbolic external orbitals¹⁴⁵ was used to avoid the complicated GUGA formalisms in the triple and quadruple space. Both methods are implemented in the UNDMOL program. Another way to reduce the time of calculation would be to use either internally^{82,146} or externally^{85,147} contracted CI functions. However, this approximation may lead to the loss of correlation energy, and in particular can fail in the treatment of states with many singly occupied orbitals.

One commonly used method to reduce the run time of any computational program is through program parallelization. All modern computers including personal ones nowadays are multi-core computers. In computational sciences, supercomputers are used more and more in all disciplines of sciences. Supercomputers not only provide more multiple cores to run processors, they also provide access to the memory spaces of multiple nodes. Computational chemistry software including Gaussian,¹⁴⁸ GAMESS,¹⁴⁹ COLUMBUS,¹⁵⁰ MOLPRO,¹⁵¹ etc. use tools like Linda,¹⁵² Distributed Data Interface,¹⁵³ Global Array¹⁵⁴ to manage the usages of distributed-memory. However, these packages

were developed decades ago. The current supercomputers are equipped with large memory on each node, usually around 64G or more. With smart partitioning of the data, it is possible for a parallel program to access the local memory only for the majority of a calculation, avoiding the communication of nodes at the memory level. With this hope in mind, tools for shared-memory programming on distributed-memory are not used in this study. In the current work, in order to use multiple computer nodes in the same calculation, a message passing interface (MPI) approach realized by the Open MPI library is used. This allows us to use supercomputers that are built on either shared or distributed memory access infrastructure.

The aim of this research is to parallelize the TQ perturbation part of MRCISD(TQ) calculations, called *tqcorr.exe* in the UNDMOL software suite. The parallel code was developed based on the configuration driven GUGA approach of nR-MRCISD(TQ), with the CSFs arranged by configurations and by macroconfigurations. Since the size of macroconfigurations vary drastically, it is not a good idea to assign macroconfigurations to processors naively based on the index of the macroconfigurations. Instead, a master/slave type parallelization scheme was used to assign macroconfigurations dynamically to the slave processors, depending on which slave is available at a given time.

MRCISD(TQ) Method

The MRCISD(TQ) method used in this study was also referred to as the nR-MRCISD(TQ) method.¹²⁹ It is an iterative method that can simultaneously calculate the energies of multiple low-energy states, as opposed to the previous MRCISD(TQ) method² developed in our group.

The MRCISDTQ subspace can be divided into three subspaces: a reference subspace R specified by a given set of reference configurations; a Q₁ subspace that is related to the R space configurations by all single and double excitations that are not already included in R space; and a Q₂ subspace related to R space by triple and quadruple excitations. R and Q₁ spaces form the model space M, which has all configurations in MRCISD space. The exact, self-consistent primary space P is defined by projecting the exact MRCISDTQ wavefunction to the target low-lying states $|\bar{\Psi}_P\rangle = |\Psi_1, \Psi_2, \dots, \Psi_{N_P}\rangle$, such that the vectors from its orthogonal space in M (referred to as the secondary space S) make no contributions to $|\bar{\Psi}_P\rangle$.^{155,156} Of course, this would be unrealistically expensive in practice and a primary space spanned by the MRCISD vectors of interest is used. In this way, the parts of the model space are concentrated to a much smaller P space. The exact S space doesn't have any interaction with the Q₂ space and an approximate S space can be assumed to have sufficiently small interactions with the Q₂ space for the primary states of interest.

A wave operator Ω that maps the optimal primary space basis $|\bar{\Phi}_P\rangle = |\Phi_1, \Phi_2, \dots, \Phi_{N_P}\rangle$ to $|\bar{\Psi}_P\rangle = \Omega|\bar{\Phi}_P\rangle = P\Omega|\bar{\Phi}_P\rangle + Q_2\Omega|\bar{\Phi}_P\rangle = |\bar{\Phi}_P\rangle\Omega_{PP} + |\bar{\chi}_{Q_2}\rangle\Omega_{Q_2P}$ can be generated while satisfying the orthonormalization condition

$$\langle\bar{\Phi}_P|\Omega|\bar{\Phi}_P\rangle = \mathbf{\Omega}_{PP}^+\mathbf{\Omega}_{PP} + \mathbf{\Omega}_{PQ_2}^+\mathbf{\Omega}_{Q_2P} = \mathbf{I}_P. \quad [3.1]$$

where

$$\mathbf{\Omega}_{PP} = \langle\bar{\Phi}_P|\Omega|\bar{\Phi}_P\rangle \text{ and } \mathbf{\Omega}_{Q_2P} = \langle\bar{\chi}_{Q_2}|\Omega|\bar{\Phi}_P\rangle. \quad [3.2]$$

This wave operator is formally defined for the primary space, but it is useful to extend its domain to the entire model space. This is done by defining it to act as the identity operator within the secondary space, i.e., $\Omega(P+S) = S + P\Omega P + Q_2\Omega P$.

The Schrodinger equation for the N_p lowest energy states in the model space is

$$H\Omega|\bar{\Phi}_p\rangle = \Omega|\bar{\Phi}_p\rangle \mathbf{E}_p. \quad [3.3]$$

Following the above definitions, a Hermitian effective Hamiltonian can be generated for the model space by

$$H^{eff} = M\Omega^+H\Omega M, \quad [3.4]$$

which satisfies

$$H^{eff}|\bar{\Phi}_p\rangle = |\bar{\Phi}_p\rangle \mathbf{E}_p. \quad [3.5]$$

The effective Hamiltonian can be calculated by blocks: $SH^{eff}S = SHS$;

$$SH^{eff}P = SHP\Omega P + SHQ_2\Omega P ; PH^{eff}P = \frac{1}{2}[(P\Omega P)^{-1}H\Omega P + P\Omega^+HP(P\Omega P)^{-1}].$$

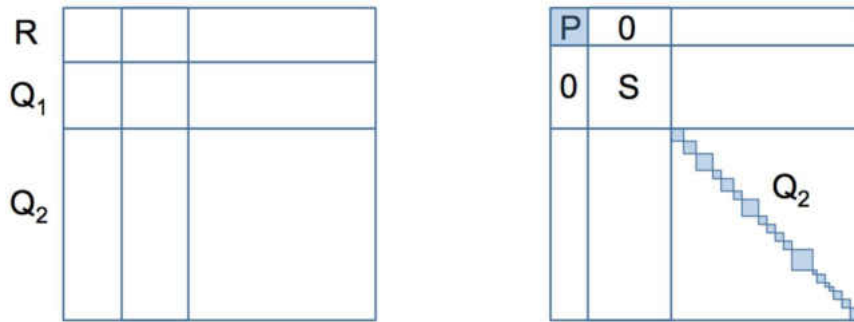


Figure 10. Subspace arrangement in MRCISD(TQ) method. R: reference space. Q₁: SD excitation space. Q₂: TQ excitation space. P: Primary space. S: secondary (orthogonal) space.

In CSF basis $|\vec{\chi}_M\rangle = |\vec{\chi}_R, \vec{\chi}_{Q_1}\rangle$ matrix form, its N_p -lowest roots can be solved by

$$\mathbf{H}_{MM}^{eff} \mathbf{C}_{MP} = \mathbf{C}_{MP} \mathbf{E}_P. \quad [3.6]$$

The \mathbf{C}_{MP} matrix rotates the reference part of the nonoptimal wave function into the optimal one and thereby generates a new wave operator by $|\vec{\Phi}_P\rangle = |\vec{\chi}_M\rangle \mathbf{C}_{MP} = |\vec{\chi}_R\rangle \mathbf{C}_{RP} + |\vec{\chi}_{Q_1}\rangle \mathbf{C}_{Q_1P}$.

We point out that the new wave functions $\vec{\Phi}_P^{(n)}$ can also be used as basis functions to generate new wave operators $\Omega_{PP}^{(n)}$ and $\Omega_{Q_2P}^{(n)}$ and new effective Hamiltonian matrices $\mathbf{H}_{MM}^{eff(n)} = \langle \vec{\chi}_M | \Omega^{(n)+} H \Omega^{(n)} | \vec{\chi}_M \rangle$. In this way, if the S subspace of the effective Hamiltonian were to be calculated, the full MRCISDTQ wave function could be approximated perturbatively in an iterative manner, using

$$|\vec{\Psi}_P^{(n)}\rangle = \Omega^{(n-1)} |\vec{\Phi}_P^{(n)}\rangle = \left(|\vec{\Phi}_P^{(n-1)}\rangle \Omega_{PP}^{(n-1)} + |\vec{\chi}_{Q_2}\rangle \Omega_{Q_2P}^{(n-1)} \right) \langle \vec{\Phi}_P^{(n-1)} | \vec{\Phi}_P^{(n)} \rangle \quad [3.7]$$

which is variationally optimal at each iteration for given wave operators $\Omega_{PP}^{(n)}$ $\Omega_{Q_2P}^{(n)}$.

Similarly, the total MRCISDTQ energy is approximated by

$$\mathbf{E}_P^{(n)} = \langle \vec{\Psi}_P^{(n)} | H | \vec{\Psi}_P^{(n)} \rangle = \langle \vec{\Psi}_P^{(n)} | H^{eff(n-1)} | \vec{\Psi}_P^{(n)} \rangle = \mathbf{C}_P^{(n)+} \mathbf{H}_{MM}^{eff(n-1)} \mathbf{C}_P^{(n)} \quad [3.8]$$

When all quasidegenerate states of interest are included in the primary space, we can expect the coupling between the primary space and secondary space $SH^{eff}P$ to be negligible. Consequently, as noted earlier, it should be sufficient to construct and diagonalize the effective Hamiltonian in the primary space, and solve

$$\mathbf{H}_{PP}^{eff(n-1)} \mathbf{W}_{PP}^{(n)} = \mathbf{W}_{PP}^{(n)} \mathbf{E}_P^{(n)} \quad [3.9]$$

instead. Similarly, the new estimate of the primary space projection of the wavefunction can be calculated by

$$\left| \vec{\Phi}_P^{(n)} \right\rangle = \left| \vec{\Phi}_P^{(n-1)} \right\rangle W_{PP}^{(n)} = \left| \vec{\Phi}_P^{(0)} \right\rangle W_{PP}^{(1)} W_{PP}^{(2)} \dots W_{PP}^{(n)} \quad [3.10]$$

Because of its huge size, the Hamiltonian for Q_2 space must be approximated. One approximation is to project blocks that include the diagonal, with each block corresponding to the Hamiltonian matrix elements of a set of CSFs that belong to a specific configuration. A more drastic approximation is to the pure diagonal, which results in an Epstein-Nesbet approximation. In an earlier investigation,¹³⁰ we showed that a modified Epstein-Nesbet (i.e., configurationally averaged) gave approximately the same results as did the block diagonal variant. The part of the wave operator that calculates the effect of all CSFs generated from a given configuration (a set of vectors in Q_2 space, denoted as e_2) into part of the primary space wavefunction can be expressed as

$$\Omega_{e_2 I}^{(n)} = -\frac{1}{\varepsilon_{e_2} - E_I^{(n)}} H_{e_2 P}^{(n)} \Omega_{PI}^{(n-1)} \quad [3.11]$$

where I is a state in the P space, and ε_{e_2} is the average energy of configuration e_2 in the Q_2 space.

$$\varepsilon_{e_2} = \frac{1}{\dim(L_{e_2})} \sum_{q_2 \in L_{e_2}} \langle \chi_{q_2} | H | \chi_{q_2} \rangle \quad [3.13]$$

Since the model space is separated into the P space and the S space and the Q_2 space, and the primary space is separated by a large space of CSFs that mostly originate from the Q_1 space, the energy differences between the P space and the Q_2 space is large. Consequently, MRCISD(TQ) method should not face any intruder state problem.

Macroconfigurations

The concept of macroconfigurations was first developed in our group to describe the electron distribution in active spaces.⁶³ A macroconfiguration is defined by the groups of orbitals and the number of electrons in those groups, such that each group of orbitals can be anywhere from empty to fully occupied, as long as the total number of electrons match to the number of active electrons.

$$(\text{group } 1)^{n_1} (\text{group } 2)^{n_2} (\text{group } 3)^{n_3} \dots (\text{group } g)^{n_g}$$

$$0 \leq n_i \leq 2 \times \dim(\text{group}_i) \quad [3.14]$$

$$n_{act} = \sum_{i \leq g} n_i$$

For example, a complete active space¹² is the simplest macroconfiguration, which specifies only one group of orbitals and the number of electrons that occupy them. A model space calculation with restricted active space¹³ include three groups of orbitals called RAS1, RAS2, and RAS3. If allowing a maximum of two electrons and two holes in the RAS3 and RAS1 orbital groups respectively, the active space would include the following six macroconfigurations: $(\text{RAS1})^{n_{\text{RAS1}}}(\text{RAS2})^{n_{\text{RAS2}}}(\text{RAS3})^{n_{\text{RAS3}}}$, $(\text{RAS1})^{n_{\text{RAS1}}-1}(\text{RAS2})^{n_{\text{RAS2}}+1}(\text{RAS3})^{n_{\text{RAS3}}}$, $(\text{RAS1})^{n_{\text{RAS1}}-1}(\text{RAS2})^{n_{\text{RAS2}}}(\text{RAS3})^{n_{\text{RAS3}}+1}$, $(\text{RAS1})^{n_{\text{RAS1}}-2}(\text{RAS2})^{n_{\text{RAS2}}+2}(\text{RAS3})^{n_{\text{RAS3}}}$, $(\text{RAS1})^{n_{\text{RAS1}}-2}(\text{RAS2})^{n_{\text{RAS2}}+1}(\text{RAS3})^{n_{\text{RAS3}}+1}$, $(\text{RAS1})^{n_{\text{RAS1}}-2}(\text{RAS2})^{n_{\text{RAS2}}}(\text{RAS3})^{n_{\text{RAS3}}+2}$.

Macroconfigurations do not have any restrictions on the number of electrons in any group of orbitals; the idea of macroconfigurations is more similar to the generalized active space¹⁴, but is more structured than it. Similar to what is done in RAS partitioning, orbitals having similar energies can be put into a group and given total occupancies to form macroconfigurations, such as putting the orbitals with bonding character into RAS1, and

the anti-bonding characters into RAS3. However, sometimes it can be more advantageous to put orbitals with the same spatial extent into the same group, combining both bonding and antibonding type orbitals, in a generalization of valence bonds.

Inside of the UNDMOL software suite, CSFs are always arranged by macroconfigurations. As a result, parallelization of nR-MRCISD(TQ) can be achieved by assigning CSFs to the CPUs in packages of macroconfigurations.

The nR-MRCISD(TQ) calculation is programmed using a macroconfiguration-driven GUGA. When evaluating the interaction of the primary and the Q_2 space, a screening process is carried out first to speed up the calculation. Since the Hamiltonian is at most a two-electron operator, macroconfigurations that differ by more than two electron excitations do not interact with each other, thus no calculation is needed.

The original GUGA is not very effective for complicated incomplete active space calculations. Macroconfigurations provide a clean, elegant, yet flexible way of treating incomplete active spaces. In the calculations, each macroconfiguration has an orbital distinct row table (DRT), and the interaction of macroconfigurations can be calculated by the overlay of the orbital DRT. When needed, the orbital paths can be expanded into sets of Shavitt step vectors.

From a programming point of view, arranging CSFs into groups according to macroconfigurations divides the large CI vector of CSFs into smaller chunks, allowing the computer to read only a small portion into the memory at a time, eliminating the requirement of large memory. Even when the calculation system gets large, the memory attached to a single CPU should be large enough such that tools for shared-memory programming on distributed-memory Global Array¹⁵⁴ are not necessary.

It is possible to separate the CSFs in a single macroconfiguration into several macroconfigurations. This is proven very useful in order to parallelize nR-MRCISD(TQ) efficiently. For example, a CAS(2, 2) can be represented in a single macroconfiguration that assigns two electrons into a group of two orbitals a and b , which can be denoted as $(a, b)^2$, but it can also be represented by three macroconfigurations $(a)^2(b)^0$, $(a)^1(b)^1$, and $(a)^0(b)^2$. These two ways contain the same number of CSFs, but the number of CSFs in each macroconfiguration is reduced in the second case, as are the related single-, double-, triple and quadruple excitations, thus allowing for more efficient parallelization.

Parallelization scheme

The most time-consuming part in the TQ perturbation calculation is the formation of H_{Q_2P} . In practice, the matrix product $H_{PP}^{eff(n-1)}W_{PP}^{(n)}$ is updated right after the formation of the H_{Q_2P} matrix of a particular macroconfiguration. This is realized in the routine *mkhw*. The macroconfigurations in the Q_2 space only interact with the model space, but not with each other (in the perturbation approximation we use), and each macroconfiguration updates the $H_{PP}^{eff(n-1)}W_{PP}^{(n)}$ matrix with the same weight, as a result, it is possible to divide this task by macroconfigurations in the Q_2 space. However, since the numbers of CSFs vary drastically in each macroconfiguration, distributing macroconfigurations to processors simply based on their indices is not very efficient. Instead, we decide to use a master/slave type MPI scheme to assign the next macroconfiguration calculation to the next available processor. This sacrifices the level of parallelization of the program by 1 processor but limits the occurrences of the worst-case scenarios. After all servant processors finish calculating the contributions from all macroconfigurations in the Q_2

space, the master processor collects the results from all slave processors and continues with the rest of the calculation that involves diagonalizing the $H_{PP}^{eff(n-1)}W_{PP}^{(n)}$ matrix which is small (typically no more than ten by ten in size). The parallelization scheme is represented in Figure 10.

In the calculation of $mkhw$, the matrix H_{Q_2P} is only calculated in the first iteration. In the serial code, this result is written in a scratch file called *scrfile*, and they are read in subsequent iterations. This brings a new challenge if all processors need to write to the same file. In a supercomputer, it is usually a lot faster to write scratch files in the scratch space local to each node. But without knowing which macroconfigurations are assigned to which node ahead of time, it is difficult to find the correct scratch file or the correct location of the data in the file. In this regard, we decided to generate one scratch file for each processor, and request each processor to read the local scratch file. However, this requires that all the information used by the following iterations have to be calculated by the same processor in the first iteration, which means the assignments of macroconfigurations to processors must stay the same across iterations. Since all processors need to start working on $mkhw$ at the same time in each iteration, when the updated energy array is successfully broadcasted, so that the calculation time is largely determined by the size of macroconfigurations. We expect the calculation time of macroconfigurations to be slightly different across iterations, but the most time-consuming macroconfiguration in the first iteration should be the most time-consuming one in later iterations. In other words, the relative expenses of each macroconfiguration should stay roughly the same. As a result, the availability of all processors should be roughly the same in each iteration. This approach should not have a significant impact on the calculation time.

When the memory of the computer is less than what is needed to complete the TQ calculation, it is possible to write the formula tape into a scratch file called *ciftfile*. It contains the sequence number of the interacting configurations for a particular matrix element, the sequence number of the integrals entering this matrix element and the coefficients for the integrals in the matrix element. However, since this file gets re-written for each macroconfiguration, it suffices to simply generate a local *ciftfile* for each processor.

The subroutine *initci* initializes the CI space information for the entire calculation, including generating DRTs for the R space. This subroutine generates multiple arrays and arrays of complicated indexing structures for *mkhw* calculations. It is not easy to broadcast these data types to servant processors, and because this subroutine is not a time-limiting one, we have all processors run it once before the iterations start.

Since the program is embarrassingly parallel, and each macroconfiguration is quite large in the MRCISD(TQ) calculation, we don't expect the communication time to be the time-limiting step. In this code, while waiting for the slaves to finish calculating the contribution of each Q_2 space macroconfiguration, the master processor does not do anything except printing to the output file about which macroconfiguration is currently calculated by which processor. This should take a negligible amount of time compared with the work done at slave processors, even if as many as 1000 processors may work at the same time. In the current test cases, the maximum number of macroconfigurations in MRCISD(TQ) calculations is slightly over 1000. This means we can only use a maximum of the same number of cores for parallelization.

In some parallel programs, if a core can work on other things while waiting for the results from others, the non-blocking communication `MPI_iSend` and `MPI_iRecv` can be used. This allows the processor to initiate the data transfer process, but also work on something else while waiting for the data to go through. Since in the case of `MRCISD(TQ)` code, the master has nothing much to do anyway, we only use the blocking communication `MPI_Send` and `MPI_Recv` instead of `MPI_iSend` and `MPI_iRecv`.

In the current implementation of `MRCISD(TQ)`, all scratch files are stored on the scratch disk space local to the computational nodes. The only files stored at the user's work directory are the input and output files, and the infofile *undmol.dat*. This arrangement should take the maximum benefit of the fast local disk drives on the nodes.

| Master | Slave |
|---|---|
| Read user input Read infofile about general information on calculation Read CI array from cifile | Read infofile about general information on calculation |
| MPI_Bcast: Send variables based on user input MPI_Bcast: Send CI array | MPI_Bcast: Receive variables based on user input MPI_Bcast: Receive CI array |
| Initialize CI space (size construction) | Initialize CI space (size construction) |
| Start TQ iterations | Start TQ iterations |
| Re-initialize relevant variables MPI_Bcast: Send energy array | Re-initialize relevant variables MPI_Bcast: Receive energy array |
| Work on routine mkhw (assign macroconfigurations to slave processors) | Work on routine mkhw (calculate the contribution of macroconfigurations assigned by the master) |
| MPI_Reduce: sum arrays hwpp, wwpp results from all processors | MPI_Reduce: send arrays hwpp, wwpp results |
| Diagonalize hwpp matrix Obtain energy from the current iteration | Idle |
| Convergence Test | Idle |
| MPI_Bcast: send convergence test result to all processors Go to “Start TQ iterations” if not converged | MPI_Bcast: receive convergence test result Go to “Start TQ iterations” if not converged |
| MPI Finish | MPI Finish |

Figure 11. Parallelization scheme of the parallelized *tqcorr* program.

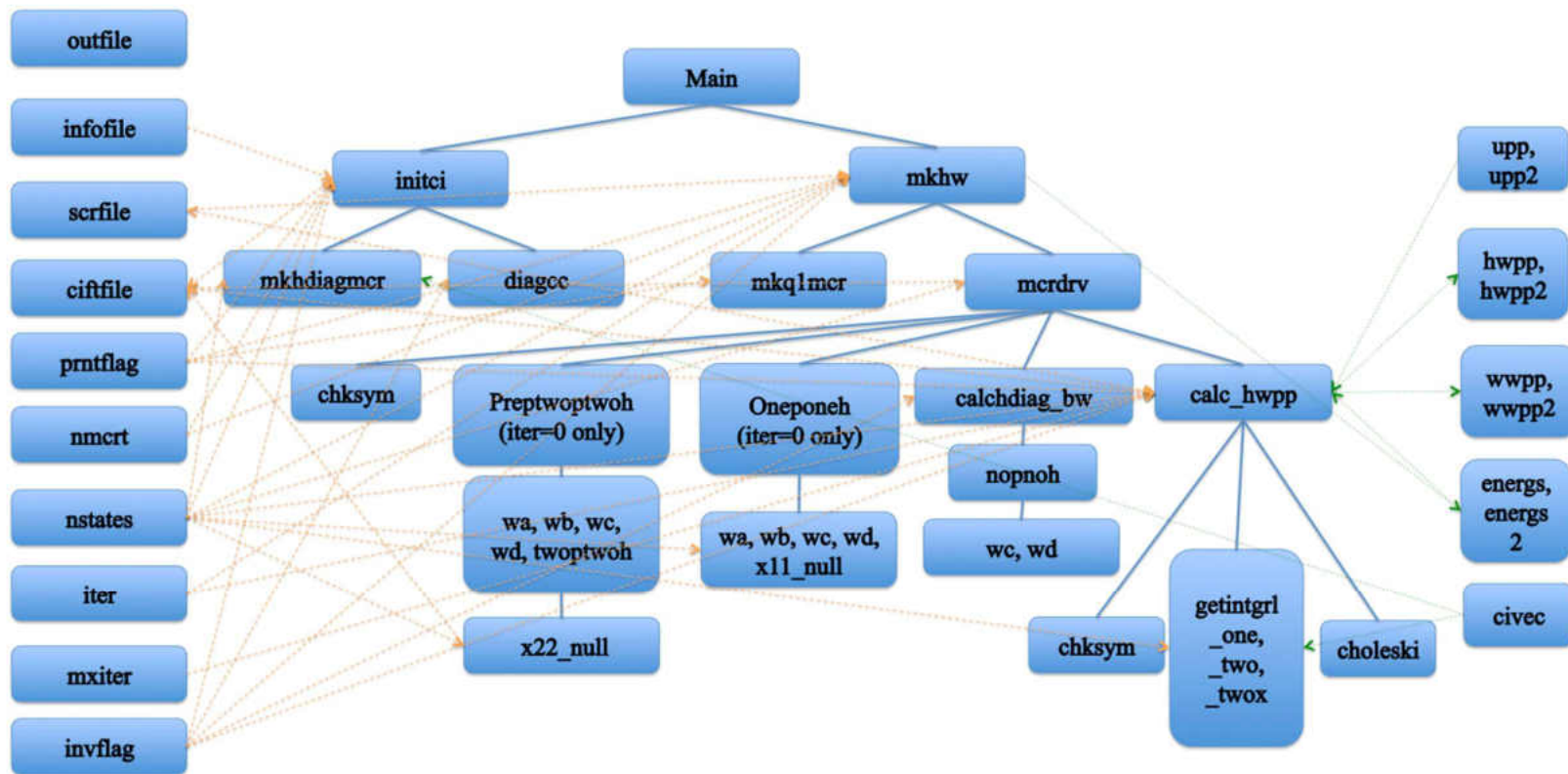


Figure 12. Structure of subroutines in the serial *tqcorr* program. Blue lines represent the calling of subroutines; orange dashed lines represent the accessing of variables; and green dotted lines represent the accessing of arrays. The arrows indicate read and write direction. In order to simplify the graph, the accessing relationship of outfile and the main function is ignored.

The parallelization was performed using one of the most commonly used open source MPI libraries: Open MPI. It supports InfiniBand which provides the inter-node communication on the test supercomputer.

Machine Specifications

The calculations reported here were all performed on the local Linux supercomputer at the University of North Dakota: “Hodor”. The 32 Dell PowerEdge 720 computer nodes are connected through the PCIe 3.0 expansion bus. Each node is configured with dual 64bit, Intel E5-2643 3.3GHz SandyBridge processors, giving a total of 8 cores per node. Each node also has 64GB of random access memory. The file system has two 146GB 15K revolutions per minute drives in Mirror Raid configuration. The nodes communicate through a private 1Gbit Ethernet Administration Network and a private 56Gbit FDR one-to-one InfiniBand Research Network.

Results

The systems used in the test calculations are summarized in Table 9 below. Water, the oxygen molecule, singlet and triplet methylene, and propargyl are selected to test the parallelization efficiency. The reference space active spaces are selected to be the CAS style in all calculations, represented by collections of macroconfigurations. The reference spaces remain the same in MCSCF, MRCISD, and MRCISD(TQ) calculations. All core orbitals are held “frozen” (i.e., unchanged from the final orbitals of the MCSCF calculation and doubly occupied) in the MRCISD and subsequent MRCISD(TQ) calculations. The MCSCF calculations are used to provide the orbitals and the MRCISD calculations are

used to generate the model space. Neither MCSCF nor MRCISD calculations are parallelized, and they are calculated by UNDMOL1.2. All TQ perturbation calculations are performed with the new *tqcorr.exe* program.

It can be seen from Figure 13 that the scaling is almost linear up to 8 cores in cases A, B, C, and G; but in the case of D and F, the scaling is nearly linear to about 16 cores. In cases A, B, C, and G, the total speedup can be as large as 4-5 times. In cases D and F, the speedup can be as large as 14-15 times. The worst case is E, where barely any improvement is achieved.

Since each node of the supercomputer “Hodor” has eight processors, it is naturally expected that the performance curve would change more drastically at multiples of 8 processors. This is caused by the inter-node communication. This trend is observed in all test cases except case H.

Since the partitioning of the CSFs used in parallelization is done by macroconfigurations, the relative sizes of macroconfigurations determined if the distribution is even or not, which impacts the parallelization efficiency. Test cases G, H, and I in Figure 14 are designed to investigate this. All three calculations work on the same O₂ system using the same aug-cc-pVTZ basis set with the same model space CAS composed of 8 electrons occupying all six p type orbitals. The calculation results agree to 10⁻¹², which is the energy tolerance of choice. The only thing different is the definition of macroconfigurations. Test H assigns all six orbitals as a group, then generates the CAS. Test G further divides the six orbitals into three groups based on if the orbitals are generated from p_x, p_y, or p_z orbitals, then the CAS is generated by occupying these three groups. Test I divides all six orbitals into six groups, with each group containing only one orbital. With

this treatment, the total number of macroconfigurations is different in all cases, even though the number of CSFs stays the same. The larger macroconfigurations are further divided into smaller ones, allowing multiple processors to work on the original same macroconfiguration. It can be seen that Test I scales the best, while Test H scales the worst.

To investigate this behavior, a variable called the granularity index can be defined to measure the characteristic of the calculation. It's defined as the maximum number of CSFs in a single macroconfiguration divided by the total number of CSFs.

$$GranularityIndex = \frac{MaxNumCSFsPerMacroconfiguration}{TotalNumCSFs} \quad [3.15]$$

The smaller the granularity index is, the more evenly CSFs are divided into macroconfigurations, and the better scaling should be achieved. If the largest grain of calculation takes 50% of the entire workload, the program can only speed up by a factor of two, no matter how many processors are used. Similarly, if the largest grain of calculation takes 5% of the entire workload, the maximum of speed up one can expect to achieve is 20. It should be mentioned here that the granularity index is not an exact measure of the parallelization workload, due to the fact that not all CSFs in the Q_2 space interact with all CSFs in the primary space. But since each calculation is different, and we can't always look into the code to find out which macroconfigurations interact with which, this provides a convenient way to roughly estimate the parallelization efficiency. Also, this information is generated by *mcrefgs_tq.exe*, a fast program run before the *tqcorr.exe* that can provide a warning before the heavy calculation of TQ perturbation is executed.

It can be seen from Figure 13 that calculations with similar granularity indices scale similarly with respect to the increase of cores. In cases E, F, and I, in order to achieve high parallelization efficiency, all reference space macroconfiguration groups are defined to

contain only one orbital such that the maximum number of configurations are generated. Based on these test calculations, it is recommended to use as many macroconfigurations as possible in MRCISD(TQ) calculations.

Conclusions

The MRCISD(TQ) method, a triple and quadruple correction to the MRCISD method, was parallelized in the computational chemistry software UNDMOL. The program was implemented and tested on the supercomputer “Hodor” which has 32 PowerEdge 720 computer nodes connected through the PCIe 3.0 expansion bus. Each node is configured with dual 64bit, Intel E5-2643 3.3GHz SandyBridge processors, giving a total of 8 cores per node. Each node also has 64GB of random access memory. The program uses macroconfigurations to divide the configuration space into smaller sections and the interactions between the Q_2 and the primary spaces are evaluated macroconfiguration by macroconfiguration. A master/slave type of parallelization scheme is used in the programming. The program is embarrassingly parallel.

Our test results show that the parallelization scaling is better when the CSFs are divided into more macroconfigurations. This can be done by including less orbitals in macroconfiguration orbital groups. This allows the each macroconfiguration to contain less CSFs, especially the most computationally expensive macroconfigurations that dominate the total speed up of the calculations. Based on the test examples, it is recommended to use the maximum number of macroconfigurations when defining the active space in MRCISD(TQ) calculations.

Table 9. Details of the molecules used in benchmark MRCISD(TQ) calculations.

| | A | B | C | D* | E | F* | G | H | I |
|---|-----------------------------|-----------------------------|------------------|-------------------------------|-------------------------------|-------------------------------|-----------------|-----------------|-----------------|
| System | CH ₂ | CH ₂ | H ₂ O | C ₃ H ₃ | C ₃ H ₃ | C ₃ H ₃ | O ₂ | O ₂ | O ₂ |
| State | ¹ A ₁ | ³ B ₁ | A ₁ | B ₁ | B ₁ | B ₁ | B _{1g} | B _{1g} | B _{1g} |
| Basis | AVTZ | AVTZ | AVTZ | VDZ | VDZ | VTZ | AVTZ | AVTZ | AVTZ |
| Active Space | 6e, 6o | 6e, 6o | 8e, 6o | 5e, 5o | 5e, 5o | 5e, 5o | 8e, 6o | 8e, 6o | 8e, 6o |
| No. Macroconfigurations | 117 | 111 | 133 | 1294 | 44 | 1294 | 113 | 9 | 735 |
| No. CSFs | 5.98E8 | 1.11E9 | 1.59E9 | 4.39E9 | 4.39E9 | 2.34E11 | 2.53E8 | 2.53E8 | 2.53E8 |
| Max. CSFs per Macroconfiguration | 1.19E8 | 2.23E8 | 2.58E8 | 2.27E8 | 2.31E9 | 1.31E10 | 4.25E7 | 2.31E8 | 6.46E6 |
| Granularity Index | 0.20 | 0.20 | 0.16 | 0.051 | 0.53 | 0.056 | 0.17 | 0.91 | 0.026 |

* Only the first iteration is calculated.

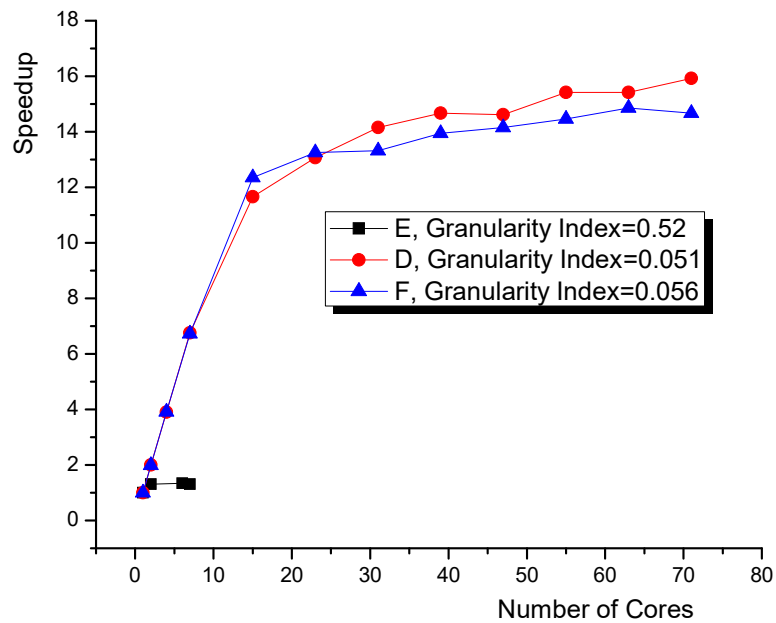
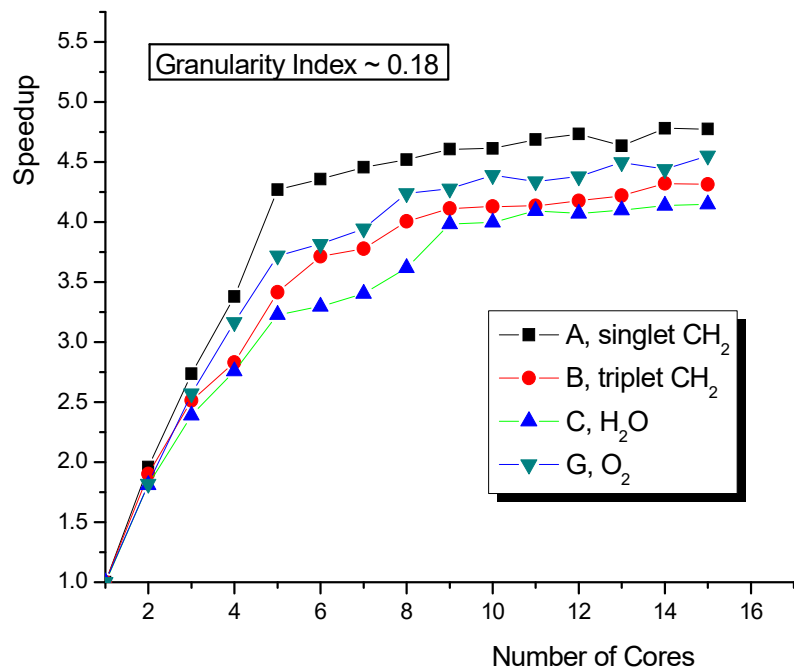


Figure 13. Speedup curves of MRCISD(TQ) test cases.

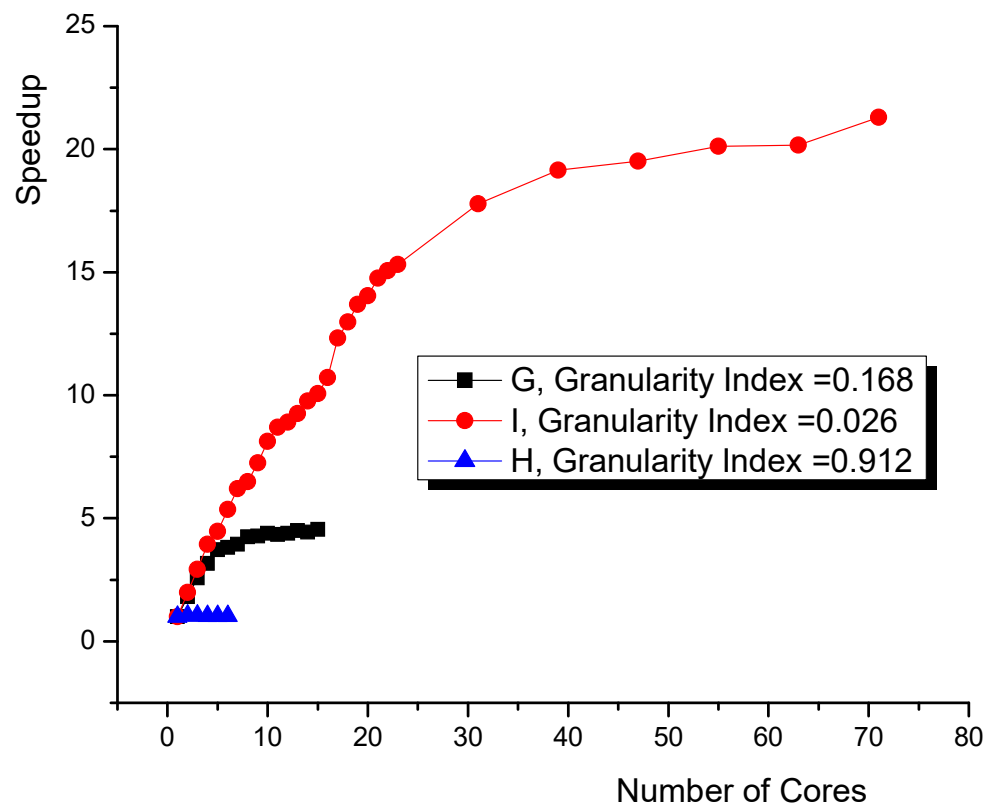


Figure 14. Speedup management based on the macroconfigurations granularity.

CHAPTER IV.

PARALLELIZATION OF THE SECOND ORDER GENERALIZED VAN VLECK PERTURBATION THEORY

Introduction

Multireference perturbation methods are considered among the most efficacious methods in electronic structure calculations. They are normally built on top of MCSCF wave functions which qualitatively capture the multireference character in the system, and singly and double excited configurations from the MCSCF configurations are included to quantitatively correct the energy and wave function of the system. Since multi-state multireference methods can calculate multiple electronic states in the same calculation, and they are considerably cheaper than the MRCI methods, they are widely used in the calculation of entire potential energy surfaces.

However, the most commonly used multireference perturbation theories, such as the popular CASPT2⁸ and MCQDPT2¹⁵⁷ methods, suffer from the intruder state problem.¹⁵⁸ Figure 15 illustrates a famous example of the potential energy surface calculation of the manganese dimer in which CASPT2 not only provides quantitatively wrong results, but that the energy curves are discontinuous at numerous geometries. This problem arises from the near zero-order degeneracy of the reference electronic states and the zero-order external space electronic states, or the so-called “intruder state problem”.¹⁵⁸ By using a matrix representation of the primary-external interaction operator X and a

hyperbolic tangent matrix function, the GVVPT2 variant of quasidegenerate perturbation theory is able to solve intruder state problem and always give a finite, physically sensible result.^{9,131,155,159}

The aim of this research is to parallelize the configuration-driven GUGA-based GVVPT2 calculation (called *gvvpt2cfg.exe*). Similar to MRCISD(TQ), the CSFs in GVVPT2 are also arranged by configurations and ultimately by macroconfigurations. The master/slave type parallelization scheme is used to assign macroconfigurations dynamically to the slave processors, depending on which slave is available.

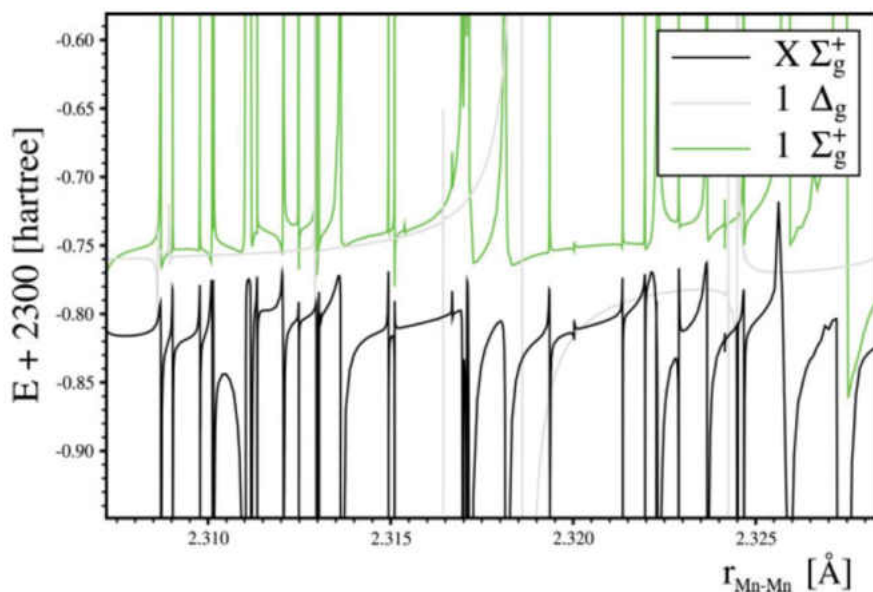


Figure 15. The potential energy curve of Mn_2 calculated by MCQDPT. Reproduced with permission from Figure 3 of Reference 158.

GVVPT2 Method

$GVVPT2^{9,156,159}$ can be derived from block-diagonal (self-consistent) quasidegenerate perturbation theory,^{131,155} which is similar to the so-called CEPA¹⁶⁰

methods, although at least an order of magnitude less computationally demanding. Similar to MRCISD(TQ), the Hamiltonian subblocks of GVVPT2 can also be spanned by a configuration space composed of orthonormal CSFs. This configuration space can be further partitioned into a model space L_M , and an external space L_Q . The model space is usually MCSCF type, and the L_Q space contains all CSFs that are generated by single and double excitations from the L_M space. The target wave functions of the lowest energy electronic states can be expanded in the antisymmetrized basis generated from the configuration space above, and they can be expressed as $|\bar{\Psi}_P\rangle = |\Psi_1, \Psi_2, \dots, \Psi_{N_P}\rangle$, where P labels the primary space, which contains all CSFs in which the users are interested. A secondary space, labeled S, $L_M = L_P \oplus L_S$ can be constructed to be the orthogonal complement of the primary space in the model space. Using the Van Vleck formalism,¹⁶¹ a unitary wavelike operator $\Omega = e^X$ can be used to transform a given set of reference wave functions $|\bar{\Phi}_P\rangle = |\Phi_1, \Phi_2, \dots, \Phi_{N_P}\rangle$ into $|\bar{\Psi}_P\rangle = e^X |\bar{\Phi}_P\rangle$, which satisfies the generalized Bloch equation $H\Omega P = \Omega P H^{eff} P$. Here, $H^{eff} = e^{-X} H e^X$ is the effective Hamiltonian, and $P = |\bar{\Phi}_P\rangle\langle\bar{\Phi}_P|$ is a projection operator on the primary L_P space. In the optimal primary subspace, where the subspace coincides with the projection of the exact wave function on the model space, a transformation matrix can be used to connect the many electron basis set $|\bar{\Phi}_P\rangle = |\bar{F}_M\rangle \mathbf{C}_{MP}$, and the operator X only describes the interaction of the primary L_P space and the external L_Q space.

$$X = QXP - PX^+Q = \sum_{p,q} X_{qp} \left(|F_q\rangle\langle\Phi_p| - |\Phi_p\rangle\langle F_q| \right) \quad [4.1]$$

where $|F_q\rangle$ is a CSF in the external L_Q space, and $Q = \sum_q |F_q\rangle\langle F_q|$ is the projection operator on the external L_Q space.

In this way, it can be seen that

$$QH^{eff}P = 0 \quad [4.2]$$

$$SH^{eff}P = 0 \quad [4.3]$$

where S is the projection operator on the secondary space. In this construction, the P–S interaction can be solved variationally, allowing one to consider strongly quasidegenerate primary and secondary states. The Q–S interaction wave operator does not need to be constructed, and the X operator directly transfers the effect of the L_Q space on the L_P space.

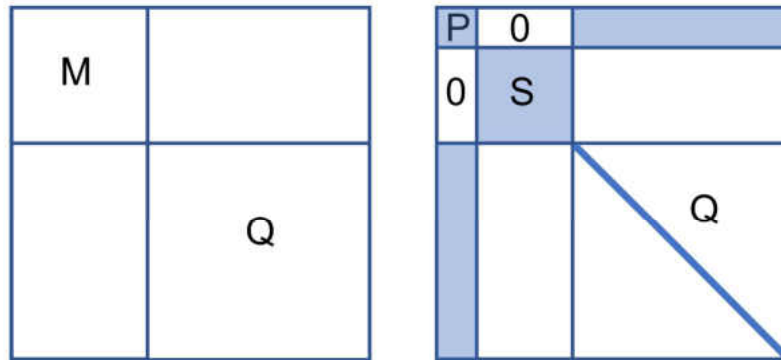


Figure 16. Subspace arrangement in GVVPT2 method. M: model space. Q: SD excitation space (external space). P: Primary space. S: secondary (orthogonal) space.

The operator X can be expressed in a perturbation series. The unperturbed Hamiltonian is chosen as $H_0 = PHP + QHQ$, and the perturbation part is the off-diagonal

block $V = PHQ + QHP$. Expanding the X operator to the first order in the wave functions, the model space effective Hamiltonian \mathbf{H}_{MM}^{eff} can be constructed using a blocked form

$$\mathbf{H}_{PP}^{eff} = \mathbf{H}_{PP} + \frac{1}{2}(\mathbf{H}_{PQ}\mathbf{X}_{QP} + \mathbf{X}_{QP}^+\mathbf{H}_{QP}) \quad [4.4]$$

$$\mathbf{H}_{SP}^{eff} = \mathbf{H}_{SQ}\mathbf{X}_{QP} \quad [4.5]$$

$$\mathbf{H}_{SS}^{eff} = \mathbf{H}_{SS} \quad [4.6]$$

Without further approximation, the P-Q interaction in a block-diagonal quasidegenerate perturbation theory satisfies the relationship^{155,156}

$$(\mathbf{H}_{QQ} - E_0^p)\mathbf{X}_{QP} = -\mathbf{H}_{QP}, p \in [1, N_p] \quad [4.6]$$

where $E_0^p = \langle \Phi_p | H | \Phi_p \rangle$ is the energy of the p-th reference state, which as mentioned above is selected to be the MCSCF eigenvectors within the model space.

In order to solve \mathbf{X}_{QP} above, several types of approximations can be made. The most naïve one is to define each element as

$$X_{qp}^{(X)} = \frac{H_{qp}}{\mathcal{E}_p^{(0)} - \mathcal{E}_q^p} = \frac{H_{qp}}{\Delta_X \mathcal{E}_q^p}, p \in L_p, q \in L_Q \quad [4.7]$$

where $H_{qp} = \langle F_q | H | \Phi_p \rangle$, $\mathcal{E}_p^{(0)}$ is the Møller-Plesset type energies of the unperturbed states in the primary space, and \mathcal{E}_q^p is the state specific zeroth-order energy of CSF q in the external space, which is the same for all CSFs belonging to the same external configuration, expressed as $\mathcal{E}_{m_e}^p$. They can be calculated from the state-specific one-particle reduced density matrix

$$D_{ab}^p = \langle \Phi_p | E_{ab} | \Phi_p \rangle = \sum_{mn} C_{mp} C_{np} \langle F_m | E_{ab} | F_n \rangle \quad [4.8]$$

and the state dependent orbital energies

$$f_{\mu}^p = h_{\mu\mu} + \sum_{a \geq b} D_{ab}^p \left[(\mu\mu|ab) - \frac{1}{2}(\mu a|\mu b) \right] \quad [4.9]$$

where $p \in L_p, m, n \in L_M$, a, b are occupied orbitals, and μ is any orbital.

$$\varepsilon_p^{(0)} = \sum_a f_a^p D_{aa}^p \quad [4.10]$$

$$\varepsilon_{\mathbf{m}_e}^p = \sum_{\mu} f_{\mu}^p N_{\mu}^{\mathbf{m}_e}, \quad [4.11]$$

where $N_{\mu}^{\mathbf{m}_e}$ is the occupation number of orbital μ in configuration \mathbf{m}_e . From this approximation, the energy contribution to the p-th electronic state from each external configuration can be written as

$$\Delta E_X^p(\mathbf{m}_e) = \sum_{q \in \mathbf{m}_e} H_{qp} X_{qp} = \frac{1}{\Delta_X \varepsilon_q^p} \sum_{q \in \mathbf{m}_e} H_{qp}^2 = -\frac{1}{\varepsilon_{\mathbf{m}_e}^p - \varepsilon_q^{(0)}} \sum_{q \in \mathbf{m}_e} H_{qp}^2 \quad [4.12]$$

However, when the energy difference $\varepsilon_{\mathbf{m}_e}^p - \varepsilon_p^{(0)}$ is small, the energy correction approaches singularity, and the approximation above fails drastically. Still following the general derivation of the response parameter $X_{qp}^{(Y)} = \frac{H_{qp}}{\Delta_Y \varepsilon_q^p}$, another approximation (denoted by Y instead of the original X) was designed by explicitly diagonalizing the Hamiltonian matrices involving uncoupled (p, \mathbf{m}_e) interactions, instead of treating them perturbatively.

This leads to the energy difference of the primary and external states as

$$\Delta_Y \varepsilon_q^p = \frac{1}{2}(\varepsilon_{\mathbf{m}_e}^p - \varepsilon_p^{(0)}) - \frac{1}{2} \sqrt{(\varepsilon_{\mathbf{m}_e}^p - \varepsilon_p^{(0)})^2 + 4 \sum_{q \in \mathbf{m}_e} H_{qp}^2} \quad [4.13]$$

and the correction energy from each configuration

$$\Delta E_Y^p(\mathbf{m}_e) = \frac{1}{\Delta_Y \mathcal{E}_q^p} \sum_{q \in \mathbf{m}_e} H_{qp}^2 = \frac{1}{\frac{1}{2}(\mathcal{E}_{\mathbf{m}_e}^p - \mathcal{E}_p^{(0)}) - \frac{1}{2} \sqrt{(\mathcal{E}_{\mathbf{m}_e}^p - \mathcal{E}_p^{(0)})^2 + 4 \sum_{q \in \mathbf{m}_e} H_{qp}^2}} \sum_{q \in \mathbf{m}_e} H_{qp}^2 \quad [4.14]$$

By plotting out the energy correction as a function of primary-external state energy differences, it can be seen that when $\mathcal{E}_{\mathbf{m}_e}^p \ll \mathcal{E}_p^{(0)}$, the energy correction calculated by approximation Y is unlimitedly large, which is unphysical. This corresponds to the case where the external configurations dominate the wave function instead of the model space configurations. Although this condition is rarely reached, it can be approached by Rydberg-type configurations, since usually only configurations generated by valence orbitals are included in MCSCF calculations. In order to solve this problem, a hyperbolic tangent function is used to bind the energy correction to a finite number, generating the final form of the GVVPT2 rotation parameter.

$$X_{qp}^{(Z)} = \frac{-\tanh(\Delta_Y \mathcal{E}_q^p)}{\Delta_Y \mathcal{E}_q^p} H_{qp} \quad [4.15]$$

$$\Delta E_Z^p(\mathbf{m}_e) = \frac{-\tanh(\Delta_Y \mathcal{E}_q^p)}{\Delta_Y \mathcal{E}_q^p} \Delta E_Y^p(\mathbf{m}_e) \quad [4.16]$$

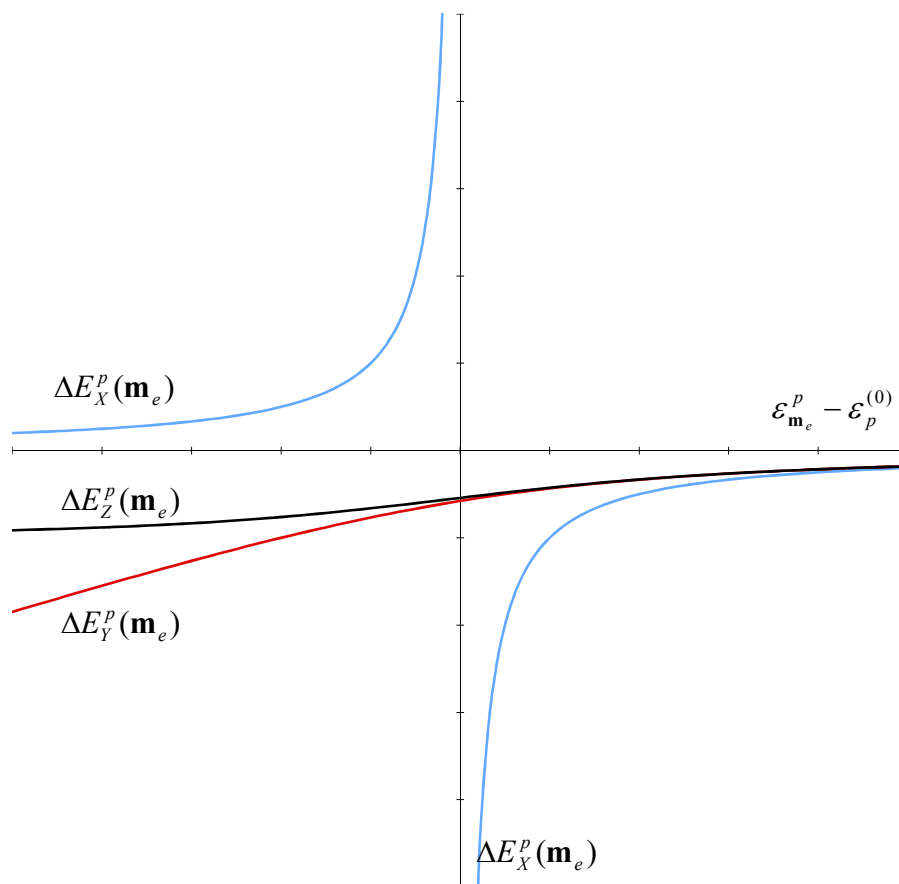


Figure 17. Schematic diagram of the dependence of the correction energies on the energy difference $\varepsilon_{\mathbf{m}_e}^p - \varepsilon_p^{(0)}$. The blue curve correspond to scheme X, the red one correspond to scheme Y, and the black one correspond to scheme Z.¹⁵⁹

Parallelization scheme

Assuming reliable orbitals are provided in a previous calculation (e.g., MCSCF), a complete GVVPT2 calculation starts from the atomic integral calculation of the orbital basis by *aoints.exe* and an orbital ordering process by *orbord.exe*; this is followed by an partial integral transformation realized by *mctrans.exe* (which is the same as the integral transformation needed in an MCSCF calculation, hence the name of the program); *mrcfsgs.exe* generates the macroconfigurations in the external space, then the *gvvpt2cfg.exe* program calculates the actual GVVPT2 vectors and energy; usually *printcfg.exe* is

executed subsequently to printout the detailed information of configurations and orbitals. Among all executable files, the *gvvpt2cfg.exe* takes the longest amount of time, followed by *aoints.exe*. With the increase of active space and the number of basis functions, the calculation of *gvvpt2cfg.exe* increases dramatically, whereas *aoints.exe* is only affected by the increase of basis functions. Thus, *gvvpt2cfg.exe* is the program that was chosen to be parallelized first.

Similar to the situation encountered with in MRCISD(TQ) method, where the external configuration contributions to the primary space configurations are independent of other external configurations, the GVVPT2 method can also be partitioned in an embarrassingly parallel manner. Since GVVPT2 also arranges the CSFs based on macroconfigurations, and these macroconfigurations are different in size as well, following the same argument as used with MRCISD(TQ), the master/slave partitioning technique is also applied to the parallelization of GVVPT2. Since macroconfiguration partitioning of CSFs reduces the amount of memory used in the program, and we know that the serial GVVPT2 program works on a single core, we think that it is not necessary to access memory across nodes, and thus global memory libraries are not used.

The most time-consuming part in the GVVPT2 perturbation calculation is the evaluation of the effect of the external space. This is done by calculating $X_{QP}, (X^+X)_{PP}$

where each element $(X^+X)_{ij} = \sum_{q \in L_Q} X_{iq}^+ X_{qj}$, and finally $(HX)_{MP}$ where each element

$(HX)_{mi} = \sum_{q \in L_Q} \langle F_m | H | F_q \rangle X_{qi}$. This is realized in the routine *mkhx*. The algorithm used in

mkhx is listed in Figure 18.

As can be seen from examination of Figure 19, the subroutines *init* (which initialize all subspaces and allocates memory space from the heap for arrays), *mkorben* (which generates and stores orbital energies), *mkopdm* (which generate the one-particle density matrices) and *offdiag* (which generates the off-diagonal Hamiltonian of the model space), all calculate data that needs to be used later in the calculations. Since these data are of complicated structure and hard to be broadcasted to all processors, and these calculations don't take much time, we ask them to be performed on all processors, such that each processor has a copy of the same calculation results. The majority of the changes in the serial code needed to achieve parallelization were done in the subroutine *mkhx*.

Initialize $(HX)_{MP}$, X_{QP} , $(X^+X)_{PP}$

Loop over macroconfigurations in the Q space

 Loop over configurations in the Q space

 Loop over interacting macroconfigurations in the M space

 Loop over configurations in the M space

 If (Q-M) configuration pairs interact

 If X_{QP} is being evaluated

 Calculate H_{qi} for future use

 Else if $(HX)_{MP}$ is being evaluated

 Calculate $(HX)_{mi}$

 End loop configurations in M

 End loop macroconfigurations in M

 If X_{QP} is being evaluated

 Calculate X_{qi}

 Calculate ε_{iq} and $\Delta_Y \varepsilon_q^p$

Figure 18. Algorithm used in the mkhx routine.

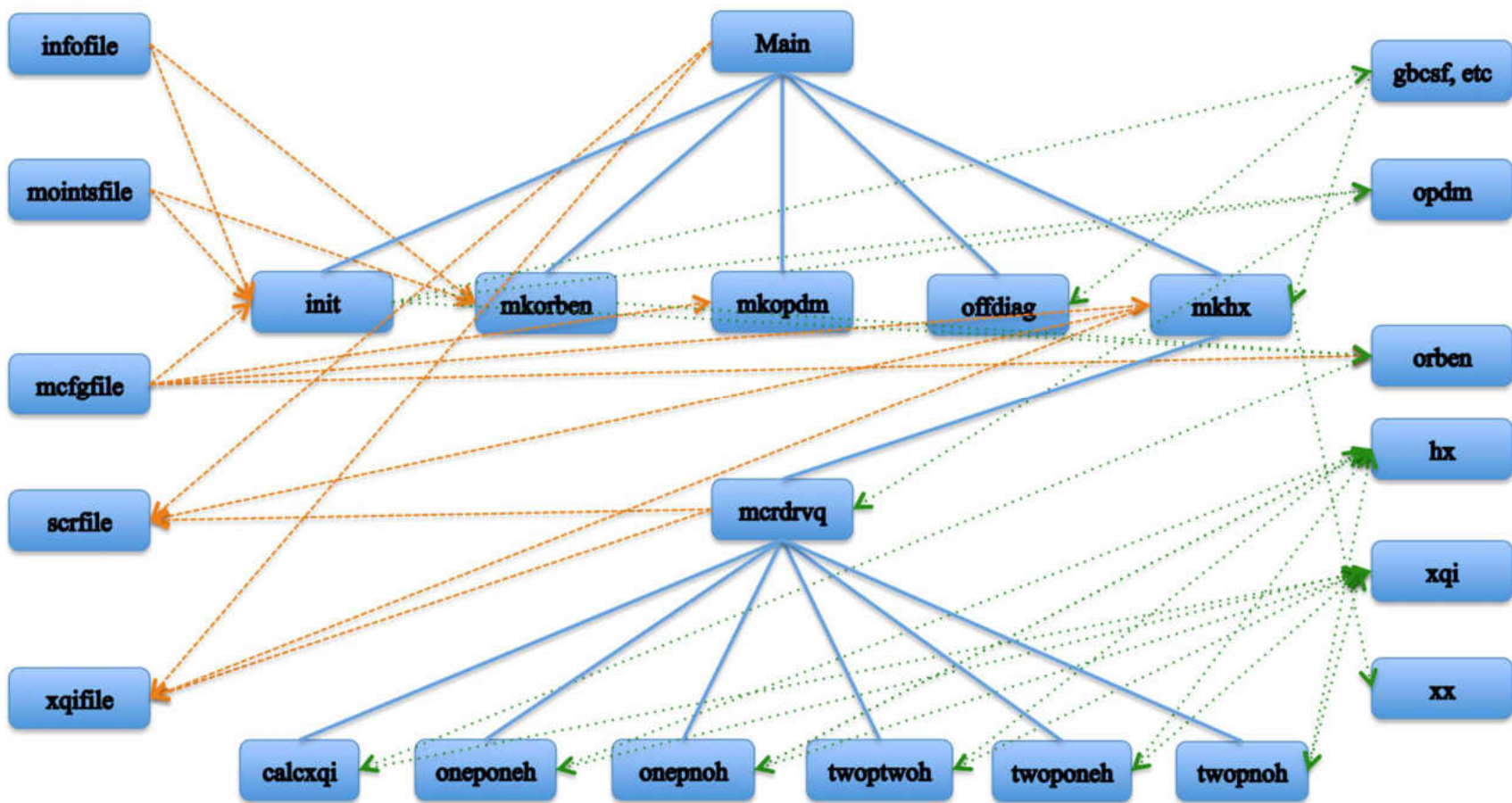


Figure 19. Structure of subroutines in the serial *gvpt2cfg* program. Blue lines represent the calling of subroutines; orange dashed lines represent the accessing of variables; and green dotted lines represent the accessing of arrays. The arrows indicate read and write direction. In order to simplify the graph, subroutines after the perturbation calculations are ignored and their accessing relationship is absorbed by their parent routines. The accessing relationship of outfile and the main function are also ignored.

| Master | Slave |
|---|--|
| Read user input Read infofile about general information on calculation | Read user input Read infofile about general information on calculation |
| Initialize CI space (size construction) Model space calculation Construct one particle density matrix Calculate orbital energy | Initialize CI space (size construction) Model space calculation Construct one particle density matrix Calculate orbital energy |
| Work on routine <i>mkhw</i> --Assign macroconfigurations to slave processors --Receive and record the result of X_{QP} | Work on routine <i>mkhw</i> --Calculate the contribution of assigned macroconfigurations to X_{QP} , $(X^+X)_{PP}$, and $(HX)_{MP}$ --Send the result of X_{QP} |
| MPI_Reduce: sum arrays $(HX)_{MP}$ results from all processors | MPI_Reduce: send arrays $(HX)_{MP}$ results |
| Calculate the HX_{PP} matrix Construct and diagonalize the effective Hamiltonian in the primary space Record data in the scratch file for subsequent calculations | Idle |
| Check convergence MPI_Finalize | MPI_Finalize |

Figure 20. Parallelization scheme of the parallelized *gvvpt2cfg* program.

In MRCISD(TQ) calculations, the model space wave function is usually perturbatively corrected in an iterative manner, although a single iteration suffices in many cases. This requires that the Hamiltonian of the primary-external space interaction be saved in the scratch files (called *scrfile*). Since the sizes of these files are large, they are saved on individual nodes, and the partitioning of the data in these files must remain the same across iterations. However, GVVPT2 calculations require a different way to handle this scratch file. Because the GVVPT2 vector can be used in subsequent GVVPT3 calculations or can be used as the initial guess vector in MRCISD calculations, it is still necessary to save the X_{qi} vectors in the scratch space. But in order for the subsequent calculations to read in the data, considering that these calculations are unrelated to GVVPT2 and are not yet parallelized, it is much more advantageous to save the data to a single file. This is done by transferring the X_{qi} vectors to the master processor and having the master node write the vectors to the appropriate locations in the file. This allows the master to work on the I/O duty whereas the slave nodes work on the calculation duty, relieving the workload from the slaves. Currently, the blocking communications MPI_Send and MPI_Recv are used to transfer the X_{qi} vectors from the slaves to the master processor. We estimate the calculation time on slaves should be much longer than the file writing by the master; as a result, little time would be wasted while waiting for the data to come through. If this step turns out to create a blocking barrier for the efficient parallelization, a non-blocking data transfer with MPI_iSend and MPI_iRecv can be easily implemented to allow the master to write the scratch file while truly waiting for the next data to come through. When the subsequent calculation is MRCISD, this information is copied into another file called *xqifile*.

In order to take advantage of the speed of the scratch space distributed to the computing nodes, all scratch files are stored there. The only files stored in the user's work directory are the input and output files, and the infofile *undmol.dat*. The parallelization was performed using one of the most commonly used open source MPI libraries: OpenMPI. It supports InfiniBand which provides the inter-node communication on the test supercomputer.

The serial version of macroconfiguration-driven GVVPT2 programed in UNDMOL1.3 was parallelized in this work. This version of the GVVPT2 program also takes advantage of sparse storage of electron repulsion integrals over molecular orbitals, and this can reduce the memory usage in GVVPT2 calculations.

Machine Specifications

The calculations reported here were also performed on the local Linux supercomputer in the University of North Dakota: "Hodor". The 32 Dell PowerEdge 720 computer nodes are connected through their PCIe 3.0 expansion buses. Each node is configured with dual 64bit, Intel E5-2643 3.3GHz SandyBridge processors, totaling 8 cores per node. Each node also has 64GB of random access memory. The file system has two 146GB 15K revolutions per minute drives in a Mirror Raid configuration. The nodes communicate through a private 1Gbit Ethernet Administration Network and a private 56Gbit FDR one-to-one InfiniBand Research Network. Due to the stability of the supercomputer, all test calculations presented below write their scratch files to the head node, thus the I/O efficiency is not as ideal as it can be, but we believe the test results can still provide enough insights to the performance of the parallelization.

Results

The systems used in the test calculations are summarized in Table 10 below. Ozone, nitrogen dioxide, and sulfur dioxide molecules were selected to test the parallelization efficiency. All calculations are performed using the aug-cc-pVTZ basis set.¹³⁴ MCSCF calculations were used to provide the initial orbitals for the subsequent GVVPT2 calculations. In both MCSCF and GVVPT2 calculations, full-valence CAS style active spaces are selected to be the model space, represented by collections of macroconfigurations. All core orbitals are frozen (i.e., held doubly occupied after MCSCF optimization) in the GVVPT2 calculations. The MCSCF calculations are not parallelized, and were calculated using UNDMOL1.3. All GVVPT2 calculations are performed with the new *gvvpt2cfg.exe* program, and the results are presented below. It is worth noting that all calculations times presented here are the calculation of *gvvpt2cfg.exe*, not the entire GVVPT2 calculations which also include programs *aoints.exe*, *orbord.exe*, *mctrans.exe*, *mcrcfgs.exe*, and *printcfg.exe*.

Since the parallelization scheme is based on macroconfigurations, the size distributions of CSFs in the macroconfigurations has a large impact on the load balancing of the parallel program. An easy way to control the size of macroconfigurations is by tailoring macroconfigurations to be larger or smaller in calculations. Similar to the investigation of parallelized MRCISD(TQ), several definitions of macroconfigurations were used to achieve various granularity indices, which are defined as the maximum number of CSFs in a single macroconfiguration divided by the total number of CSFs. The selections of macroconfiguration groups are summarized in Table 10. To avoid extremely

inefficient parallelization, all CAS orbital groups are broken down to at least three groups. But since GVVPT2 only considers singly and doubly excited configurations in the external space, the model space can be much larger than the reference space of MRCISD(TQ) calculations. In MRCISD(TQ) calculations, in order to obtain a large number of macroconfigurations, all reference space macroconfiguration groups only have one orbital. This is unnecessary in the GVVPT2 calculations because simple manual separation of macroconfigurations groups can generate very low granularity indices. In the test calculations of NO₂, breaking all twelve CAS orbitals into 3 groups in the way indicated in Table 10 can generate a granularity index of 0.13, further dividing them into 4 groups can lower the granularity index by about 50%, whereas breaking them down to 11 groups further lowers granularity index down by 99%. In the test calculations of O₃, breaking all twelve CAS orbitals into 3 groups can give a granularity index of 0.11, and breaking them into 6 groups can reduce the index to 15 times smaller.

Table 10. Details of the molecules used in GVVPT2 benchmark calculations.

| Molecule | O₃ | O₃ | NO₂ | NO₂ | NO₂ | SO₂ |
|--|--|------------------------------|--|--|---|--|
| Grain Size | fine | coarse | medium | fine | coarse | medium |
| Point Group | C _s | C _s | C _{2v} | C _{2v} | C _{2v} | C _{2v} |
| Target State | A' | A' | A ₁ | A ₁ | A ₁ | A ₁ |
| Grouping of active orbitals | 2 A', 2 A', 2 A', 2 A', 1 A', 3 A'' | 4 A', 4 A', 1 A' 3 A'' | 5 A ₁ , 1 A ₂ , 2 B ₁ , 4 B ₂ | 2 A ₁ , 2 A ₁ , 2 A ₁ , 2 A ₁ , 1 A ₁ , 1 A ₂ , 1 A ₂ , 2 B ₁ , 1 B ₂ , 1 B ₂ , 1 B ₂ , 1 B ₂ | 5 A ₁ , 1 A ₂ 2 B ₁ , 4 B ₂ | 5 A ₁ , 1 A ₂ , 2 B ₁ , 4 B ₂ |
| Total CSFs | 7.0E+08 | 7.0E+08 | 1.0E+09 | 1.0E+09 | 1.0E+09 | 1.1E+09 |
| Total MCRs | 1625 | 108 | 213 | 13710 | 104 | 213 |
| Max CSFs per macroconfiguration | 5.0E+06 | 7.8E+07 | 6.6E+07 | 4.9E+05 | 1.3E+08 | 7.1E+07 |
| Max CSF / Ave CSF | 11.56 | 12.06 | 14.09 | 6.66 | 13.81 | 14.18 |
| Granularity Index | 0.0071 | 0.1117 | 0.0662 | 0.0005 | 0.1327 | 0.0666 |

It can be seen from Figure 21 that the scaling is different for different systems. All calculations speed up by at least 2.7 times when using 3 slave cores (N.B. 4 processors need to be used in total), and in the calculation of fine grained O₃ and SO₂, a 12 times

speedup can be achieved using 31 slave cores, and the curves keep increasing. But in other cases, such as the coarse-grained ozone and all NO₂ calculations, the performances do not increase much after 15 slave cores are used, when the efficiency was increased by only about 6 times. In practice, it was also observed that running the same calculation multiple times could take different amounts of time, and this difference can be fairly drastic. This is most readily apparent in the coarse grain O₃ calculation. One possibility is that because this calculation has a relatively small number of macroconfigurations, and if the assignment of macroconfigurations is different in each run, then the total run time may differ more significantly than others. Another possible explanation is the read-write traffic at the time of execution. Especially because the scratch files are written to the head node, the program performance can depend on how many users are reading or writing on the head node at the time. The numbers presented in Table 11 and Figure 21 below are the average results.

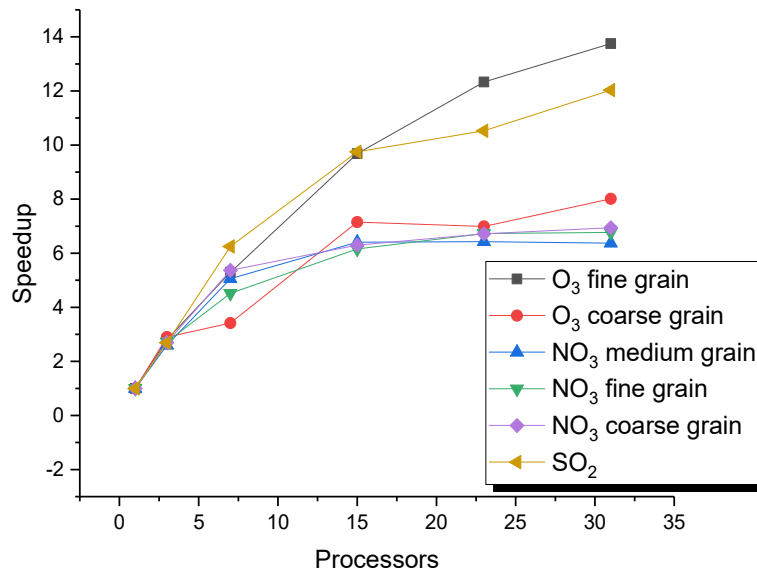


Figure 21. Speedup of the *gvvpt2cfg.exe* program

In all three calculations of NO₂, the speedup curves behave in a very similar fashion. This means that in some calculation cases, in which a considerable amount of macroconfigurations are included, load balancing with separating macroconfiguration groups stops being the limiting factor for GVVPT2 calculations. When the model active space is large (in our test cases, 17 electrons in 12 orbitals), it might be sufficient to only separate the active orbitals to a limited number of groups. In the case of O₃, dividing the active orbitals into smaller groups is better.

In MRCISD(TQ) calculations, we recommend that the users divide orbitals into groups such that as many macroconfigurations as possible are used. This is not the case in GVVPT2 calculations. It can be seen from Table 11 that in some calculations, breaking the active orbitals into more groups almost always increases the total calculation time, assuming the same number of cores are used. This is because the program needs to search for macroconfigurations, and this search is quadratically dependent on the number of macroconfigurations. Implementation of more efficient NlogN searches are possible, but have not been investigated yet. The more macroconfigurations there are, the more expensive the calculation gets. Since in GVVPT2 calculations, the parallel efficiency may not be bound by load balancing, it is not necessary to break down macroconfigurations to the finest level. Even though the search for macroconfigurations also depends quadratically on the number of macroconfigurations in MRCISD(TQ) calculations, the MRCISD(TQ) is still bound by load balancing and the ability to break down macroconfigurations to contain fewer CSFs. Thus different strategies are recommended.

We would like to point out here that if the granularity index is 0.1, the maximum speedup that can be achieved is 10 times, and because the large macroconfigurations are

usually evaluated in the later calculations, a realistic expectation of speedup from using 10 cores is possibly only 5 times. In order to achieve a speedup of 10, it's safer to start with active orbital grouping that generates a granularity index of 0.05. Or in other words, if an expected speedup is N times with N cores, it's recommended to make the granularity index around $\frac{1}{2N}$.

Since each node of the supercomputer "Hodor" has eight processors, the inter-node communication can slow down the calculations. We believe that this may be the cause of the leveling of the speedup curves of NO_2 and coarse grained O_3 curves.

Table 11. Calculation times (in seconds) test cases.

| No. Processors | O_3 | | NO_2 | NO_2 | | SO_2 |
|----------------|--------------|--------|---------------|---------------|--------|---------------|
| | fine | large | regular | fine | large | regular |
| 1 | 122.93 | 121.03 | 212.91 | 231.36 | 220.24 | 152.38 |
| 3 | 43.73 | 40.27 | 81.83 | 85.03 | 81.43 | 56.59 |
| 7 | 23.25 | 20.18 | 42.1 | 51.19 | 41.04 | 24.4 |
| 15 | 12.7 | 19.16 | 33.21 | 37.54 | 34.95 | 15.63 |
| 23 | 9.97 | 12.82 | 33.13 | 34.4 | 32.79 | 14.47 |
| 31 | 8.94 | 8.22 | 33.4 | 34.18 | 31.75 | 12.67 |

Conclusions

The GVVPT2 method, a quasidegenerate perturbation theory that does not have the intruder state problem, was parallelized in the computational chemistry software suite UNDMOL. The program was implemented and tested on the supercomputer "Hodor", which has 32 PowerEdge 720 computer nodes connected through PCIe 3.0 expansion buses. Each node is configured with dual 64bit, Intel E5-2643 3.3GHz SandyBridge

processors, totaling 8 cores per node. The program divides the configuration space into macroconfigurations and evaluates the interactions between the external and the primary spaces macroconfiguration by macroconfiguration. A master/slave type of parallelization scheme is used to assign each external space macroconfigurations to slave cores, and a master core to gather and organize the results after all macroconfigurations are evaluated. The program is embarrassingly parallel.

Our test results show that the parallelization scaling can be better when the configuration space CSFs are divided into more macroconfigurations. But after a certain number of macroconfiguration is generated, the parallelization efficiency doesn't improve any further. Instead, more macroconfigurations can actually slow down the calculation. Generally speaking, if an expected speedup is N times with N cores, it is recommended to make the granularity index around $\frac{1}{2N}$.

CHAPTER V.

IMPLEMENTATION OF RESTRICTED DENSITY FUNCTIONAL THEORY IN UNDMOL

Introduction

Since perturbation theories are generally most effective in low-order, multireference perturbation theories usually require relatively large model spaces to expand the Hamiltonian, such that the perturbation corrections are small. This is traditionally done using large CASSCF calculations. However, the number of variational parameters of MCSCF calculations grows more than exponentially with the number of orbitals; using incomplete active space calculations requires the users to select orbitals based on each individual system studied, and expert testing may be required to make sure the results make sense, even though the calculations converge which is difficult by itself. The expensive MCSCF calculation is usually the time-limiting step in order to perform MRPT2 calculations. This also limits the size of systems that can be calculated with MRPT2.

Realizing that the essential results obtained from MCSCF calculations are sets of molecular orbitals to expand the many-electron wave functions, either in building linear combinations of Slater determinants or CSFs, alternative molecular orbitals become of interest. Ideally, these orbitals should have been determined in the presence of some electron correlation, so that GVVPT2 can calculate the correlation based on perturbations.

Fortunately, MCSCF is not the only theory that can include modest amounts of electron correlation when determining molecular orbitals. According to the Hohenberg–Kohn theorem,²³ which states that electron density can uniquely determine the energy of any ground state system, the dynamic correlations that are usually recovered using multireference wave function methods can also be represented in single reference DFT. It was found that LDA molecular orbitals can be used to expand the many electron wave function in GVVPT2 calculations, although the pilot implementation tests were limited to complete active model spaces and small molecules.¹⁶² Assuming that the hypothesis holds true for larger systems, it would allow us to avoid the expensive and user-biased MCSCF calculations to generate orbitals for GVVPT2, thus saving tremendous time in the calculations. In the pilot study, alpha orbitals from LDA were used, because only spin-unrestricted DFT calculations were supported at the time in available computer programs. However, a cleaner and more well-defined procedure is to use restricted DFT orbitals.

Spin-restricted quantum mechanical methods are of great theoretical importance. The wavefunctions of restricted methods are eigenfunctions of the total spin operator S^2 , spin projection operator S_z (or time-reversal operator Θ) and group operators P_i of the molecular point group, whereas unrestricted wavefunctions break symmetry under of S^2 operators. Even though restricted wavefunction cannot correctly describe the breaking of bonds, which intrinsically can be viewed as a multireference problem, it offers clean and well-defined orbitals on which one can build multireference methods.

Methods

One-electron orbitals used in electronic structure calculations are functions of four variables: three spatial variables (x, y, z or r, θ, ϕ , etc., depending on the coordinate system used) and the spin variable. The spin functions can be represented in a basis of two functions: spin up and spin down. The complete four-variable one-electron wave function is called a (molecular) spin orbital. Since the nonrelativistic Hamiltonian operator does not explicitly contain spin, the one-electron spin wave function can be cleanly separated from the spatial wave function.

$$\chi = \psi(\mathbf{r})\sigma(m_s) \quad [5.1]$$

The spin functions²⁰ are very simple, and lend themselves to a 2-vector representation over a base 2 (i.e., binary) field,

$$\alpha\left(\frac{1}{2}\right)=1, \alpha\left(-\frac{1}{2}\right)=0, \beta\left(\frac{1}{2}\right)=0, \beta\left(-\frac{1}{2}\right)=1 \quad [5.2]$$

It is much easier to write the treat the spin function separately and expand operators in matrices of spatial wave functions. Or in another way of thinking, all operators and values are written with the spin wave function already integrated.

The two most commonly used ways of treating spin in many-electron systems lead to spin-restricted and spin-unrestricted wave functions.^{21,163} To explain the differences between restricted and unrestricted DFT methods, we first look at the differences between the restricted Hartree–Fock (RHF) method and the unrestricted Hartree–Fock (UHF) method.

In the UHF method, the alpha and beta spin orbitals are allowed to have different spatial parts,

$$\chi_i = \begin{cases} \psi_j^\alpha(\mathbf{r})\alpha(m_s) \\ \psi_j^\beta(\mathbf{r})\beta(m_s) \end{cases} \quad [5.3]$$

The full electronic energy can be expressed as²¹

$$\begin{aligned} E_0^{UHF} &= \sum_a^{N_\alpha} (\psi_a^\alpha | h | \psi_a^\alpha) + \frac{1}{2} \sum_a^{N_\alpha} \sum_b^{N_\alpha} [(\psi_a^\alpha \psi_a^\alpha | \psi_b^\alpha \psi_b^\alpha) - (\psi_a^\alpha \psi_b^\alpha | \psi_b^\alpha \psi_a^\alpha)] \\ &+ \sum_a^{N_\beta} (\psi_a^\beta | h | \psi_a^\beta) + \frac{1}{2} \sum_a^{N_\beta} \sum_b^{N_\beta} [(\psi_a^\beta \psi_a^\beta | \psi_b^\beta \psi_b^\beta) - (\psi_a^\beta \psi_b^\beta | \psi_b^\beta \psi_a^\beta)] \\ &+ \sum_a^{N_\alpha} \sum_b^{N_\beta} (\psi_a^\alpha \psi_a^\alpha | \psi_b^\beta \psi_b^\beta) \\ &= \sum_a^{N_\alpha} h_{aa}^\alpha + \sum_a^{N_\beta} h_{aa}^\beta + \frac{1}{2} \sum_a^{N_\alpha} \sum_b^{N_\alpha} (J_{ab}^{\alpha\alpha} - K_{ab}^{\alpha\alpha}) + \frac{1}{2} \sum_a^{N_\beta} \sum_b^{N_\beta} (J_{ab}^{\beta\beta} - K_{ab}^{\beta\beta}) + \sum_a^{N_\alpha} \sum_b^{N_\beta} J_{ab}^{\alpha\beta} \end{aligned} \quad [5.4]$$

Each spin has one set of the SCF equations

$$f^\alpha(1)\psi_i^\alpha(\mathbf{r}_1)\alpha(\omega_1) = \varepsilon_i^\alpha \psi_i^\alpha(\mathbf{r}_1)\alpha(\omega_1) \quad [5.5]$$

$$f^\beta(1)\psi_i^\beta(\mathbf{r}_1)\beta(\omega_1) = \varepsilon_i^\beta \psi_i^\beta(\mathbf{r}_1)\beta(\omega_1) \quad [5.6]$$

It is well known²¹ that the Fock operators f^α and f^β can be written as

$$f^\alpha(1) = h(1) + \sum_a^{N_\alpha} [J_a^\alpha(1) - K_a^\alpha(1)] + \sum_a^{N_\beta} J_a^\beta(1) \quad [5.7]$$

$$f^\beta(1) = h(1) + \sum_a^{N_\beta} [J_a^\beta(1) - K_a^\beta(1)] + \sum_a^{N_\alpha} J_a^\alpha(1) \quad [5.8]$$

As can be seen from the equation above, the Fock operator for alpha spin also depends on the Coulomb term of beta electrons. To calculate the Fock matrix for alpha spin F^α with each element $F_{\mu\nu}^\alpha = \int dr_1 \phi_\mu^*(1) f^\alpha(1) \phi_\nu(1)$, we need knowledge of beta electron densities ρ^β

. This means that F^α and F^β must be updated together with both ρ^α and ρ^β in each self-consistent field iteration.

In closed-shell systems,²¹ RHF restricts all orbitals to be doubly occupied, and the spin-up and spin-down orbitals to have the same spatial part. This also has the computational advantage that the indices in Eq. (1.1) do not need to run through all N spin-orbitals, but N/2 spatial orbitals.

$$E_0^{RHF} = 2 \sum_a^{N/2} (\psi_a | h | \psi_a) + \sum_a^{N/2} \sum_b^{N/2} 2 (\psi_a \psi_a | \psi_b \psi_b) - (\psi_a \psi_b | \psi_b \psi_a) \quad [5.9]$$

similarly, the Fock operator can be defined as

$$f^C(1) = h(1) + \sum_a^{N/2} 2J_a(1) - K_a(1) \quad [5.10]$$

In the basis $\{\phi_\mu\}$, each element of the Fock matrix takes the form

$$\begin{aligned} F_{\mu\nu}^C &= \int dr_1 \phi_\mu^*(1) f^C(1) \phi_\nu(1) \\ &= \int dr_1 \phi_\mu^*(1) h(1) \phi_\nu(1) + \sum_a^{N/2} \int dr_1 \phi_\mu^*(1) [2J_a(1) - K_a(1)] \phi_\nu(1) \\ &= H_{\mu\nu}^{core} + \sum_a^{N/2} \left[2 \int dr_1 dr_2 \phi_\mu^*(1) \phi_\nu(1) r_{12}^{-1} \phi_a^*(1) \phi_a(1) - \int dr_1 dr_2 \phi_\mu^*(1) \phi_a(1) r_{12}^{-1} \phi_a^*(1) \phi_\nu(1) \right] \end{aligned} \quad [5.11]$$

where the core-Hamiltonian matrix is defined as

$$H_{\mu\nu}^{core} = \int dr_1 \phi_\mu^*(1) h(1) \phi_\nu(1) \quad [5.12]$$

When only unpaired electrons exist in the system and the spin coupling maximizes the total spin (e.g., so-called high-spin states), there is only one shell in the entire system, which is the open shell. Spin restricted HF does not place any restriction on the one-electron functions of the unpaired electrons, the spatial wave function is conjugate to the spin wave function (i.e., it is an antisymmetrized single product of spatial functions). The total energy

takes a form that is similar to the spin-orbital Hartree–Fock expression, and can be expressed as

$$E_0^O = \sum_a^{open} (\psi_a | h | \psi_a) + \sum_a^{open} \sum_b^{open} [(\psi_a \psi_a | \psi_b \psi_b) - (\psi_a \psi_b | \psi_b \psi_a)] \quad [5.13]$$

The open-shell Fock operator is

$$f^O(1) = h(1) + \sum_a^{open} J_a(1) - K_a(1) \quad [5.14]$$

When both paired and unpaired electrons exist in the system (two-shell system), and the system is required to be an eigenfunction of S^2 , the method is referred to as restricted open-shell Hartree–Fock (ROHF). The total energy of the system can be written as the sum of a closed-shell part, an open-shell part, and a coupling.

$$\begin{aligned} E_0^{ROHF} &= 2 \left\{ \sum_a^{closed} (\psi_a | h | \psi_a) + \sum_a^{closed} \sum_b^{closed} [(\psi_a \psi_a | \psi_b \psi_b) - \frac{1}{2} (\psi_a \psi_b | \psi_b \psi_a)] \right\} \quad [5.15] \\ &+ \left\{ \sum_\mu^{open} (\psi_\mu | h | \psi_\mu) + \sum_\mu^{open} \sum_\nu^{open} [(\psi_\mu \psi_\mu | \psi_\nu \psi_\nu) - (\psi_\mu \psi_\nu | \psi_\nu \psi_\mu)] \right\} \\ &+ \left\{ \sum_a^{closed} \sum_\mu^{open} [(\psi_a \psi_a | \psi_\mu \psi_\mu) - (\psi_a \psi_\mu | \psi_\mu \psi_a)] \right\} \\ &= 2 \sum_a^{closed} h_{aa}^{closed} + \sum_a^{open} h_{aa}^{open} + \sum_a^{closed} \sum_b^{closed} (J_{ab} - \frac{1}{2} K_{ab}) + \frac{1}{2} \sum_\mu^{open} \sum_\nu^{open} (J_{\mu\nu} - K_{\mu\nu}) + \sum_a^{closed} \sum_\mu^{open} (J_{a\mu} - K_{a\mu}) \end{aligned}$$

The Fock operators of ROHF, f^c and f^o , contain both paired and unpaired electron information, and can be better expressed using density matrices, as done in the next section.

In practice, the ROHF method treats the closed-shell part separately from the open part (with the coupling occurring during convergence). The closed-shell and open-shell

parts have their own electron densities, and the Fock matrices for the closed, F^c , and the open-shell part, F^o , are calculated separately.

In order to obtain the optimal orbitals that result in the Hartree–Fock energy, a necessary condition must be met.

$$\sum_i \langle \delta\psi_i | F_i | \psi_i \rangle = 0 \quad [5.16]$$

Applying orthogonality conditions among orbitals, it can be proven^{164,165} that the condition above reduces to

$$\langle \psi_i | (F_i - F_j) | \psi_j \rangle = 0 \quad [5.17]$$

When both i and j orbitals are in the closed-shell space or the high-spin open-shell space, $F_i - F_j = 0$ is met trivially. However, when they are not in the same shell, additional steps must be taken to make sure the variational requirement is met. So far, we have two different Fock matrices for the two shells, which cannot be diagonalized with the same set of eigenvectors. We have a variational condition that has to be satisfied at the same time. Our resulting wave functions also need to be orthonormal. This can be done in a variety of ways, but is most commonly done by constructing an effective Fock matrix,^{163,164,166} whose closed-shell eigenvectors of the effective Fock matrix are the same as those of F^c , and the open-shell ones the same as those of F^o .

The approach implemented in UNDMOL follows the idea of Edwards and Zerner.¹⁶⁴ Since Hartree–Fock theory always fills orbitals starting from the lowest energy ones,¹⁶⁷ arranging the Fock matrix based on the magnitude of eigenvalues, the Fock matrix can be separated into a block form, corresponding to the paired electron (closed-shell) block, the un-paired electron (open-shell) block, and the virtual block. (Figure 22) Within

each block, unitary rotations of orbitals do not change the eigenvalue or the energy of the system. Focusing on the open-shell block, the derivation is based on the idea of expressing the wave functions of the open-shell in terms of those of the closed-shell. A Fock-like matrix can be defined as

$$F^{\mu\nu} = \Lambda^{\mu\nu} F^\nu + (1 - \Lambda^{\mu\nu}) F^\mu \quad [5.18]$$

where μ represent the closed-shell, ν represent the open-shell, and the arbitrary constants

$\Lambda^{\mu\nu} \neq 0$. A projecting operator $P^\nu = \sum_{k \in \nu} |\psi_k^\nu\rangle\langle\psi_k^\nu|$ can be used to project it to the open-shell

block. Satisfying the variational condition, a Hermitian effective Fock matrix can be defined as

$$\tilde{F}^\mu \equiv F^\mu - \sum_{\nu \neq \mu} [P^\nu F^{\mu\nu} + F^{\mu\nu} P^\nu] \quad [5.19]$$

This is the effective Fock matrix used in our program. The constants $\Lambda^{\mu\nu}$ are chosen as 1, and only one ν shell exists, which is the open-shell.

Comparing the effective Fock matrix and the closed-shell matrix, we notice that the only difference is in the open-shell block. Since the effective Fock matrix is symmetric, it is only necessary to evaluate the upper triangle (or the lower triangle) throughout the entire calculation. As a result, only the shaded triangle area of the Fock matrix is updated.

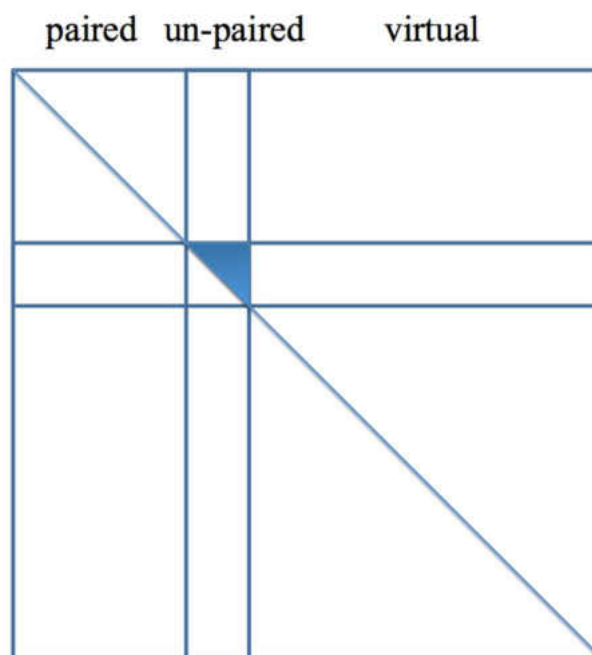


Figure 22. The blocked structure of the Fock matrix.

Relationship between ROHF and UHF Fock Matrices

UNDMOL 1.2 is capable of calculating unrestricted DFT. This is done by calculating the DFT Fock matrices for alpha, F^α and beta, F^β spins. However, in RODFT, the most natural matrix variables are the Fock operators for the closed-shell part F^c and open-shell part F^o , which are different. The computationally efficient way of calculating RODFT is to generate F^c and F^o from the closed-shell and open-shell electron densities. But, this would involve modifying each DFT functional from a dependence on spin-up and spin-down densities (and their gradients for GGA) to a dependence on closed-shell and open-shell densities. A less error-prone procedure to implement RODFT is to use existing UDFT expressions and computer code, which was the procedure followed in my work. Once the alpha and beta spin densities R^α and R^β are extracted from the total density ρ

and open-shell electron density ρ^o , the unrestricted DFT code can be used to calculate the F^α and F^β . Subsequently, these are converted into F^c and F^o , the initial Fock matrices of each iteration are updated, and the energy of the current iteration calculated. If the result is not converged, the next iteration can be carried out. This way we avoided re-writing the DFT calculations with ρ and ρ^o . The extra computational overhead is the memory needed for F^α , F^β , R^α and R^β , in addition to F^c , F^o , ρ and ρ^o , which is a small fraction of the available memory for a modern computer.

Since electron density is an additive property, the relationship of ROHF and UHF density matrices is not difficult to obtain. Following the expressions used in *Methods of Molecular Quantum Mechanics* by R. McWeeny,¹⁶³ the subscript 1 denotes the closed shell, and the subscript 2 denotes the open shell. To cleanly express the electron density in open- and closed-shells, a matrix R is defined as CC^\dagger , with C denoting the coefficient of basis functions. The matrix R has no dependency on electron occupation. In the case of UHF and UDFT, the alpha and beta R matrices R^α and R^β are the same as the density matrices, i.e. $R^\alpha = \rho^\alpha$ and $R^\beta = \rho^\beta$. However, in the case of closed-shell RHF, the matrix R is only half of the total density matrix ρ . In the cases of ROHF and RODFT, the total electron density $\rho = \rho^\alpha + \rho^\beta = R^\alpha + R^\beta = 2R_1 + R_2$ and the open-shell electron density $\rho^o = \rho^\alpha - \rho^\beta = R^\alpha - R^\beta = R_2$ are calculated. The following relationship of electron density matrices can be used to convert the RHF information to the UHF format.

$$\begin{aligned} R^\alpha &= R_2 + R_2 = \frac{1}{2}(\rho + \rho^o) \\ R^\beta &= R_1 = \frac{1}{2}(\rho - \rho^o) \end{aligned} \tag{5.20}$$

Unlike the density matrices, the Fock matrices of RODFT and UDFT are not additive. Realizing that Fock matrices are calculated based on electron density matrices, we expressed the Fock matrices as functions of density matrices. The example is given for the alpha electron UHF case (the other cases can be calculated in similar manners).

$$\begin{aligned}
F_{\mu\nu}^{\alpha} &= \int dr_1 \phi_{\mu}^*(1) f^{\alpha}(1) \phi_{\nu}(1) \tag{5.21} \\
&= H_{\mu\nu}^{core} + \sum_a^{N_{\alpha}} [(\phi_{\mu} \phi_{\nu} | \psi_a^{\alpha} \psi_a^{\alpha}) - (\phi_{\mu} \psi_a^{\alpha} | \psi_a^{\alpha} \phi_{\nu})] + \sum_a^{N_{\beta}} [(\phi_{\mu} \phi_{\nu} | \psi_a^{\beta} \psi_a^{\beta}) - (\phi_{\mu} \psi_a^{\beta} | \psi_a^{\beta} \phi_{\nu})] \\
&= H_{\mu\nu}^{core} + \sum_{\lambda} \sum_{\sigma} \sum_a^{N_{\alpha}} C_{\lambda a}^{\alpha} (C_{\sigma a}^{\alpha})^* [(\mu\nu | \sigma\lambda) - (\mu\lambda | \sigma\nu)] + \sum_{\lambda} \sum_{\sigma} \sum_a^{N_{\beta}} C_{\lambda a}^{\beta} (C_{\sigma a}^{\beta})^* (\mu\nu | \sigma\lambda) \\
&= H_{\mu\nu}^{core} + \sum_{\lambda} \sum_{\sigma} R_{\lambda\sigma}^{\alpha} [(\mu\nu | \sigma\lambda) - (\mu\lambda | \sigma\nu)] + \sum_{\lambda} \sum_{\sigma} R_{\lambda\sigma}^{\beta} (\mu\nu | \sigma\lambda)
\end{aligned}$$

Continuing to follow the expressions used in *Methods of Molecular Quantum Mechanics* by R. McWeeny,¹⁶³ a G matrix can be introduced to represent the total effect of the Coulomb and the exchange terms. It is the matrix representation of the regular two-electron operator. In one-shell systems, the expression of the G matrix is different for high-spin open-shell systems and closed-shell systems. The high-spin open-shell G' matrix takes the form $G'(R) = J(R) - K(R)$, whereas the pure closed-shell G matrix takes the form $G(R) = J(R) - \frac{1}{2}K(R)$, as can be seen from the previous section.

The benefit of using the G and the unusual density R matrices is that when both shells exist in the system, they can cleanly separate the effect of the two shells. Following these notations, the ROHF energy can be expressed as the sum of the closed- and open-shell contributions:

$$E = \nu_1 tr R_1 (h + \frac{1}{2} G_1) + \nu_2 tr R_2 (h + \frac{1}{2} G_2) \tag{5.22}$$

where ν_1 and ν_2 are the occupation numbers of each shell, so we have $\nu_1 = 2, \nu_2 = 1$.

The expressions that relate the Fock matrices in both shells are summarized in Table 12 below. For both shells, the Fock matrices are always the sum of the core Hamiltonian matrix and the G matrix. The G matrices in both shells G_1 and G_2 can always be separated into two parts that depend on closed-shell electrons R_1 and the open-shell electrons R_2 . But in the closed-shell G_1 , both R_1 and R_2 contribute in the form of G, whereas in the open-shell G_2 , electrons in the open-shell R_2 contribute in the form of G'.

Table 12. Expanding Fock matrices of closed- and open-shell parts in ROHF

| Closed-shell part in ROHF | Open-shell part in ROHF |
|-------------------------------------|--|
| $F_1 = h + G_1$ | $F_2 = h + G_2$ |
| $G_1 = G(\nu_1 R_1) + G(\nu_2 R_2)$ | $G_2 = G(\nu_1 R_1) + G'(\nu_2 R_2)$ |
| $G(R) = J(R) - \frac{1}{2} K(R)$ | $G(R) = J(R) - \frac{1}{2} K(R) \quad G'(R) = J(R) - K(R)$ |

For UHF, the expression for the Fock matrices are simpler:

$$F^\alpha = h + G_\alpha, \quad F^\beta = h + G_\beta \quad [5.23]$$

$$G_\alpha = J(R^\alpha + R^\beta) - K(R^\alpha), \quad G_\beta = J(R^\alpha + R^\beta) - K(R^\beta) \quad [5.24]$$

Using the following density matrix relationships,

$$R_1 = R_{closed} = R_\beta, \quad R_2 = R_{open} = R^\alpha - R^\beta \quad [5.25]$$

we can write the Fock matrices for UHF as

$$\begin{aligned}
F^\alpha &= h + J(R^\alpha + R^\beta) - K(R^\alpha) \\
F^\beta &= h + J(R^\alpha + R^\beta) - K(R^\beta)
\end{aligned}
\tag{5.26}$$

and write the Fock matrices for ROHF as

$$\begin{aligned}
F^o &= h + J(2R_1 + R_2) - \frac{1}{2}K(2R_1) - K(R_2) \\
&= h + J(R^\alpha + R^\beta) - \frac{1}{2}K(2R^\beta) - K(R^\alpha - R^\beta) \\
&= h + J(R^\alpha + R^\beta) - K(R^\beta) - K(R^\alpha - R^\beta) \\
&= h + J(R^\alpha + R^\beta) - K(R^\alpha) \\
&= F^\alpha \\
F^c &= h + J(2R_1 + R_2) - \frac{1}{2}K(2R_1 + R_2) \\
&= h + J(R^\alpha + R^\beta) - \frac{1}{2}K(R^\alpha + R^\beta)
\end{aligned}
\tag{5.27}$$

Since

$$F^\alpha + F^\beta = 2h + 2J(R^\alpha + R^\beta) - K(R^\alpha + R^\beta) \tag{5.28}$$

we have

$$\begin{aligned}
F^o &= F^\alpha \\
F^c &= \frac{1}{2}(F^\alpha + F^\beta) \\
F^{diff} &= F^c - F^o = \frac{1}{2}(F^\beta - F^\alpha)
\end{aligned}
\tag{5.29}$$

With these equations above, we can transform the UHF Fock matrices into the ones for ROHF.

Since DFT methods can also be expressed in terms of effective Fock matrices, the relationship above will also exist for DFT calculations. Instead of the Hartree–Fock exchange term, DFT uses an exchange-correlation term, but the main idea remains the same. All equations above can be directly applied to DFT, except F stands for the effective Fock matrices and K stands for the exchange-correlation term.

We note that hybrid DFT methods use both the Hartree–Fock exchange and the DFT exchange. In the subroutine *dft_energy*, the effective alpha and beta Fock matrices only contain the DFT exchange. The full effective Fock matrices also need to include the Hartree–Fock exchange weighted by a fraction called the Hartree–Fock exchange percentage.

$$\begin{aligned}
 F^{diff} &= \frac{1}{2}(F_{full}^{\beta} - F_{full}^{\alpha}) \\
 &= \frac{1}{2}[(F_{DFT}^{\beta} - F_{DFT}^{\alpha}) + \omega_{HF}(F_{HF}^{\beta} - F_{HF}^{\alpha})] \\
 &= \frac{1}{2}[(F_{DFT}^{\beta} - F_{DFT}^{\alpha}) + \omega_{HF}K_{HF}(R_{\alpha} - R_{\beta})] \\
 &= \frac{1}{2}[(F_{DFT}^{\beta} - F_{DFT}^{\alpha}) + \omega_{HF}K_{HF}(\rho^o)]
 \end{aligned}
 \tag{5.30}$$

Here, we use K_{HF} to denote the true Hartree–Fock exchange. This equation is used to satisfy the variational condition.

The direct inversion in the iterative subspace (DIIS) technique^{168,169} is commonly used to increase the rate of convergence of self-consistent field iterations. Since this technique does not change the physical meaning of the Fock matrices, it is possible to apply the RODFT-UDFT transformation with DIIS calculated Fock matrices.

Test calculation results

To test if our implementation is correct, we tested some molecules using both this code and GAMESS. Throughout the comparisons, we used the integration grid as similar as possible for atomic integral calculations, and we also used the same version of DFT functionals (the VWN5 version of B3LYP). It can be seen from Table 13 that RDFT and UDFT results agree with each other for small closed-shell molecules. This is expected

because breaking spin symmetry usually does not lead to great improvements for the ground states of stable molecules in their optimized geometry. UNDMOL RODFT results agree with GAMESS¹⁴⁹ results to the order of 100 micro-Hartree, no worse than the agreement of UDFT. The small disagreement might come from factors such as differences in the calculation of electron repulsion integrals.

Table 13. Test calculation on single point energies

| System | Method | DFT | Basis | UNDMOL | GAMESS |
|-------------------------------|--------|-----------------|-------|------------|------------|
| H ₂ | UDFT | Slater (or LDA) | 3-21G | -1.0337149 | |
| | RDFT | Slater | 3-21G | -1.0337149 | |
| | UDFT | B3LYP(VWN5) | 3-21G | -1.1638084 | -1.1638097 |
| | RDFT | B3LYP(VWN5) | 3-21G | -1.1638084 | -1.1638097 |
| | RHF | | 3-21G | -1.1229403 | -1.1229403 |
| H ₂ ⁺ | RDFT | Slater | 3-21G | -0.5046374 | |
| H ₂ O | RHF | | 3-21G | -75.585499 | -75.585499 |
| | UDFT | Slater | 3-21G | -74.743438 | -74.743461 |
| | RDFT | Slater | 3-21G | -74.743438 | -74.743461 |
| H ₂ O ⁺ | RDFT | Slater | 3-21G | -74.367235 | |
| | UDFT | Slater | 3-21G | -74.367235 | |
| CH ₂ (triplet) | RDFT | Slater | 3-21G | -38.064857 | |
| | UDFT | Slater | 3-21G | -38.067433 | |

We also tested the effect of using DIIS to improve the iteration efficiency. It was found that DIIS can efficiently reduce the cost of calculations. For some calculations that require 40 iterations to converge (i.e., a typical value), DIIS can converge the calculation in less than 10 iterations. This drastically reduced the calculation time.

Conclusions

By using the UDFT routine, RODFT was implemented in UNDMOL. This was achieved by converting the total and open-shell electron densities into the corresponding alpha and beta electron densities and using the UDFT routine to calculate the alpha and beta effective Fock matrices. The effective Fock matrices are subsequently converted to those of the closed- and open-shell parts. The variational condition is satisfied by constructing an effective Fock matrix and diagonalizing it. The calculation results agree with those calculated by GAMESS. We also found that the DIIS technique drastically speeds up the convergence of RODFT calculations. This code can be used to investigate other interesting topics in electronic structure theories, such as using DFT orbitals to expand model spaces in GVVPT2 calculations.

CHAPTER VI.

A DFT STUDY ON ZINC(II)-PTHALOCYANINE TETRASULFONIC ACID ON MONO-LAYER EPITAXIAL GRAPHENE ON SILICON CARBIDE(0001)

Introduction

Graphene has the structure of single sheet graphite. It is a true two-dimensional sheet of carbon atoms.^{170,171} It is strong yet light-weight, and an excellent electrical and thermal conductor, and almost optically transparent.^{172,173} Graphene-based materials have received much attention recently in areas of energy storage,^{174,175} electronics,¹⁷⁶ biological engineering,^{177,178} and photovoltaics.^{179,180} One of the unique properties of graphene is its Dirac point, which is where the conduction and valence bands of graphene meet in a cone in the momentum space. At this Dirac point, the electrons can be described formally by the massless Dirac equation; the dispersion relationship is linear, and the density of states (DOS) of graphene is zero.¹⁸¹ Because of these, it is of interest to modify the electronic properties of graphene by modifying the Dirac point. One way to do this is to create vacancies and substitutional impurities, but this was shown to affect the charge carrier mobility and significantly alter the electrical properties of graphene.^{182,183} Another commonly used way to functionalize graphene is to physisorb organic or inorganic compounds onto the graphene surface. This adsorption, in many cases, keeps the essential electronic properties of graphene intact.

In order to make sure that the molecule can be adsorbed sufficiently strongly to the graphene surface, molecules with large π systems are usually selected due to their strong π - π interaction towards graphene. Phthalocyanines are of this type. (See Figure 23) The molecules have a near-square-shaped two-dimensional structure, and their delocalized π electrons run through the entire molecule. Phthalocyanines are structurally related to porphyrins, which are the active centers of many biologically active molecules, including chlorophyll and heme.^{184,185} Traditionally, phthalocyanines are extensively used as dyes and pigments, such as the phthalocyanine blue and phthalocyanine green paints commonly used in oil paintings. Recently, their unique properties have been discovered and applied for a variety of different purposes: redox reaction catalysis, molecular electronics, and quantum computing,¹⁸⁶⁻¹⁸⁹ which inspired extensive studies focusing on phthalocyanine thin films on substrates.¹⁹⁰⁻¹⁹⁴ In the experiment that inspired our computational studies,¹⁹⁵ zinc(II)-phthalocyanine tetrasulfonic acid (Zn-PcS; see Figure 24) was selected due to its photodynamic and photothermal properties. Zn-PcS also has potential in treating cancer because its high affinity towards tumors over healthy tissue.¹⁸⁵

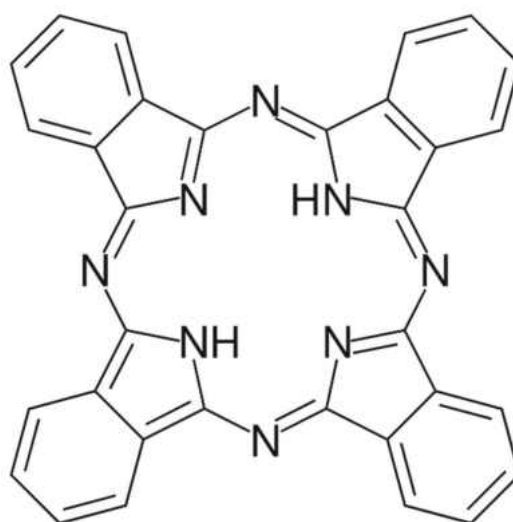


Figure 23. Structure of phthalocyanine.

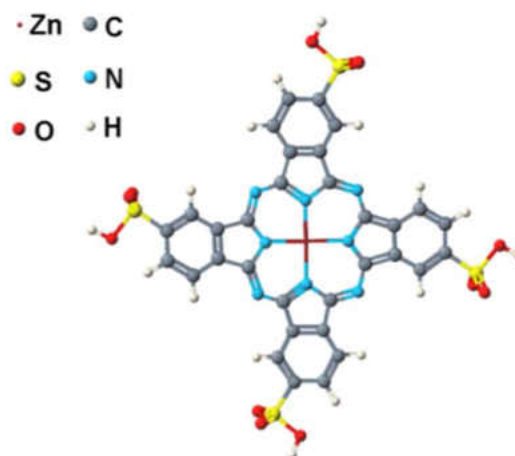


Figure 24. Structure of the Zn-PcS molecule.

There have been some studies on the adsorption of phthalocyanine/porphyrin molecules on graphene,¹⁹⁶⁻¹⁹⁹ including some studies with scanning tunneling microscopy/scanning tunneling spectroscopy (STM/STS), but since these studies were carried out at low temperatures, the room temperature results were not available. Since most applications require performance at the room temperature or higher, Dr. Oncel in UND's physics department used STM/STS to study the graphene system physisorbed with Zn-PcS, where the graphene was supported by SiC.¹⁷⁰ It was discovered that the surface coverage of Zn-PcS is very low. Instead of a layered structure, Zn-PcS molecules only individually adsorbed on the graphene sheet. Moreover, Zn-PcS molecules only adsorbed on bi-layer graphene, but not mono-layer graphene. It was also observed that the Dirac point of graphene disappears in the adsorbed system. We tried to use theoretical calculations to understand these results.

Methods

Calculations of periodic systems

Rather than Gaussian or Slater type orbitals, plane waves are more commonly used in the calculation of crystals. Then, instead of imposing the periodic condition on the wave function in the calculations, plane waves satisfy the boundary conditions by building in periodicity from the beginning (i.e., with the basis set). They are also naturally orthogonal with each other, making integrals easy to calculate. Plane waves also provide a natural way to extend the number of basis functions. One can simply include more basis functions of higher momentum to expand the basis, which is very convenient when deciding if a calculation is converged with respect to the number of basis function. From a historical point of view, plane waves in the free electron model were first applied to study the metallic solid materials made from s- and p-block elements. From a practical point of view, the development of fast Fourier transformation algorithms makes the plane wave calculations exceedingly efficient.

Core electrons in a chemical system have stronger attraction to the nucleus than do valence electrons, and thus have higher momentum. To correctly describe them with basis functions, (very) high momentum functions are necessary, which would render the calculations too expensive. However, since core electrons are rarely involved in chemical bonding or in conduction bands, it is possible to describe the effect of core electrons as a potential which screens the attraction felt by outer electrons. Pseudopotentials were developed for this reason.^{200,201} In such calculations, pseudopotentials are constructed from all-electron calculations of atoms, and they are kept the same in the other systems whether

or not the same atom is covalently bonded or is an ion in the chemical system. The pseudopotentials are generated such that above a “cut-off radius” the all-electron wave function “overlaps” with the wave function under the pseudopotential. The wave function that uses pseudopotentials should also conserve the scattering properties of the original atom in the atomic configuration. Generally speaking, each DFT method has a unique set of pseudopotentials for each atom, and these potentials can be parameterized with and without considering relativistic effects.

There are three types of commonly used pseudopotentials, namely norm-conserving, ultrasoft, and projected augmented wave (PAW) pseudopotentials. The norm-conserving potential is the “hardest”, meaning it requires higher cut-off energy or smaller cut-off radius. The ultrasoft potential relaxes the condition that the charge integrated inside the cut-off radius has to be the same in the pseudopotential and the all-electron cases, and charge augmentation is sometimes used. The PAW potential is the most accurate and has the lowest cut-off energy. It also depends less on the specific exchange-correlation functional used. It is generally recommended to use a PAW potential in calculations, which was done in our calculations.

In the modeling of surfaces and interfaces, the natural system is only periodic in two directions. It is not feasible to directly apply the program designed for modeling crystals, which are periodic in all three directions. One work around is to use a program that only has periodicity in two directions, but such programs are not as well developed as are the programs for 3-D periodicity. The other way of enforcing 2-D periodicity is to use a slab model while forcing a 3-D periodicity. By generating an array of slabs repeating along one direction, separated by sufficient vacuum, one can insure that the slabs have

negligible interaction between the slabs. (See Figure 25) In the simulation of surfaces, a few top layers of atoms are usually kept to generate the properties of the bulk material underneath, making sure the system under study is not a single layer of atoms.

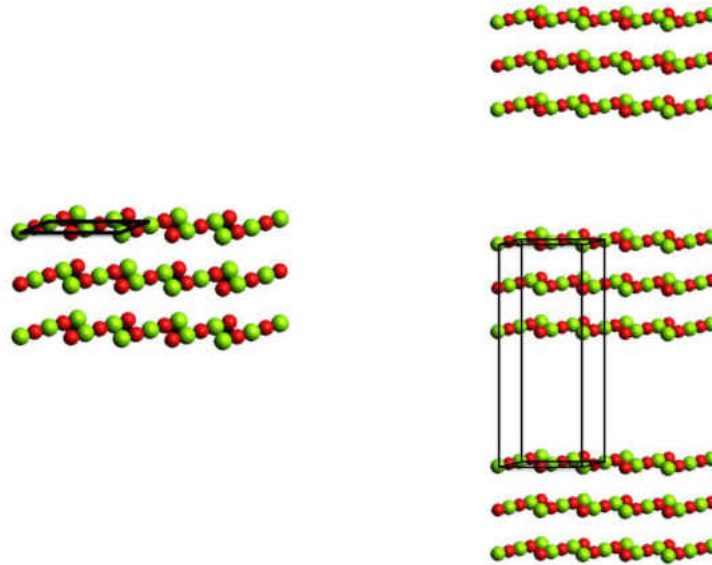


Figure 25. Three-layer slab models of the MgO (100) surface. (a) With 2-D periodic boundary conditions. (b) 3-D supercell approximation of the slab model as adopted in plane wave calculations.⁹⁶

All properties of a crystal can be obtained by integrating in the first Brillouin zone. Each point in the Brillouin zone is called a k point. Theoretically speaking, integrating the entire first Brillouin zone requires knowledge of all possible k points. But in practice, only a limited number k points are sampled, and it is hoped that they can correctly represent the properties of their neighboring k points in the reciprocal space. Monkhorst-Pack meshes are usually used to select the k points. They are equally spaced k points in the first Brillouin zone. (See Figure 26) Since crystals have translational symmetry, it is advantageous to use this symmetry to reduce the number of k points. Using the symmetry in reciprocal space, the example below shows how the number of k points can be reduced from 16 to 3.

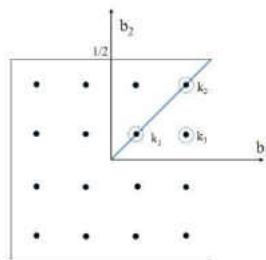


Figure 26. A two-dimensional Monkhorst-Pack mesh in the first Brillouin zone. ⁹⁶

Parameters used in the current study

In order to treat the periodic system, the Density Functional Theory (DFT) method using a plane wave basis with PAW pseudopotentials was carried out with the Quantum-ESPRESSO package.²⁰² Since the graphene system is only periodic in two directions (say x and y), we needed to use the slab model to design “supercells” that are periodic in the z direction. In the experimental results, it was observed that Zn-PcS molecules did not form a continuous layer when adsorbed to graphene; this means that in our simulation, we needed to create a large distance between Zn-PcS molecules so that they did not interact with each other. This was accomplished by placing Zn-PcS molecules periodically in the x and y directions but far away from each other, while the graphene layer underneath was continuous. In our calculation, the vacuum space was set to 21 Å along the z -direction; Zn-PcS molecules were set 16.8 Å and 16.46 Å apart from each other in the x - and y -directions. This makes our unit cell fairly large in comparison with other calculations of the same type.

As mentioned earlier, to efficiently describe the electronic structure of the system, we chose the DFT method. The Perdew–Burke–Erzerhof (PBE)²⁶ functional is an efficient yet relatively accurate exchange-correlation functional for use in the Generalized Gradient Approximation of DFT, and it was used to describe the system. To better describe the π - π

interaction, the second version of the dispersion correction developed by Grimme²⁰² was added to the PBE functional, so that our functional can be denoted as PBE-D2. While the effects of the core electrons and nuclei of the non-metal atoms were captured by the projected augmented wave method,²⁰³ and ultra-soft pseudopotentials were used in the description of Zn.²⁰⁴ The single electron states were expanded in plane waves with kinetic energy cutoffs of 47 and 188 Ry for the wave function and the charge density, respectively. In order to keep the size of the unit cell manageable, we considered only a single layer of graphene. During the geometry optimization process, the convergence criterion for the total energies was chosen as 10^{-4} a.u. between the consecutive self-consistent field calculations, and the maximum force allowed on each atom was set to 0.001 a.u. Among the possible adsorption structures, we chose the one in which the center of Zn-PcS was oriented above the center of the graphene ring. (See Figure 32) We believe that due to the low adsorption energy and the relatively large size of Zn-PcS compared with a graphene ring, the relative positioning of Zn-PcS and graphene would not make a difference. Experimentally,¹⁷⁰ it was observed that the Zn-PcS molecule can be moved around by the STM tip, which suggests that the π - π interaction between Zn-PcS and graphene is too weak to pin the molecule to a precise orientation with the surface. To get the optimized structure of the adsorbed system, the graphene sheet was frozen in space while all atoms in the Zn-PcS molecule were allowed to relax. The self-consistent field calculations were done at the gamma point, and the Density of States calculations were carried out on a $3 \times 3 \times 1$ grid.

Results and discussion

A calculation of pure graphene was performed to test the parameters selected in the study. Based on the plot of the DOS in Figure 27, it can be seen that the PBE-D2 method can correctly capture the Dirac point of the graphene layer, and our method of choice is reasonably accurate.

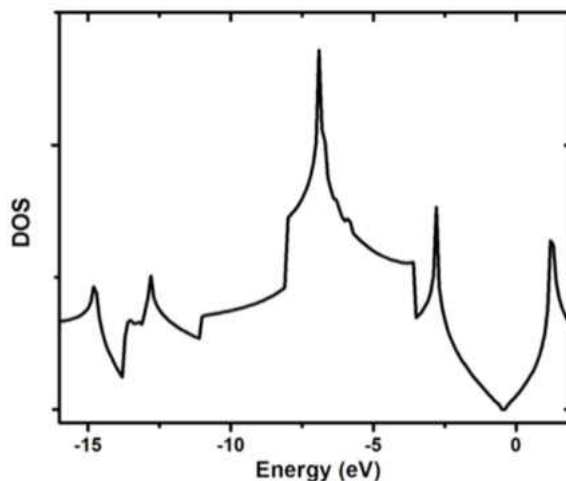


Figure 27. DOS of monolayer graphene calculated by PBE-D2¹⁷⁰

Our calculations show that the Zn-PcS molecule is about 13 Å in width and length, and about 18 Å diagonally. This confirms that the height change in the experimental scan in Figure 28 belongs to the Zn-PcS molecule. We also observed that Zn-PcS changes from a planar structure into a slightly bent one upon adsorption. The center of the molecule becomes closer to the graphene surface. This is also confirmed in the scan below. This is partly due to the fact that Zn-PcS is not completely planar. The sulfonic acid groups keep the edges of the molecule away from the graphene surface. From our calculations, it can be seen that the center Zn atom is 3.1 Å away from the graphene layer, similar to the

distance between the oxygen atoms to the graphene layer, which is 3.07 Å. The H atoms are the farthest from the graphene, with the distance of 5.5 Å. These agree with the experimental results fairly well.

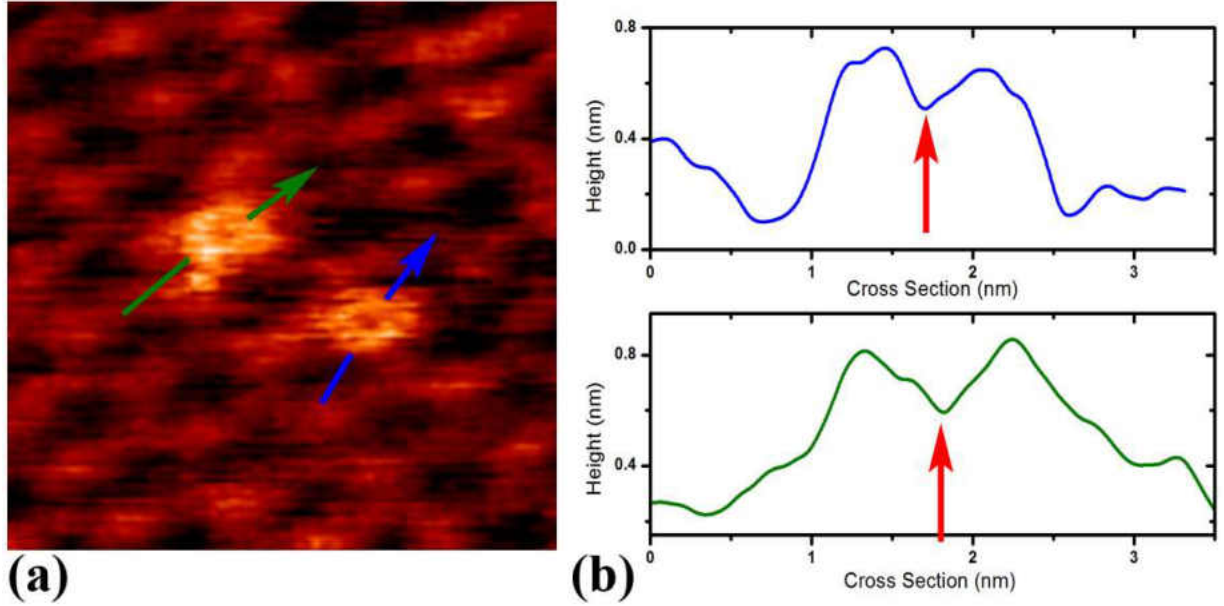


Figure 28. (a) 9nm \times 9nm experimental STM image of Zn-PcS molecules. $V=-0.93$ V, $I=0.78$ nA. Green and blue arrows indicate line scan directions. (b) corresponding line scans across each of the Zn-PcS molecules. Red arrows indicate the center of Zn-PcS molecules.¹⁷⁰

The adsorption energy in this study was defined as the differences between the summed energies of the individual systems and the energy of the adsorbed system. But the geometry of the isolated Zn-PcS molecule was taken as that of the adsorbed molecule. Use of the optimized geometry of the molecule in vacuum might make a small difference.

$$E_{adsorption} = E_{Zn-PcS} + E_{graphene} - E_{adsorbed}$$

Our calculations show that the adsorption energy of Zn-PcS is as low as 3.13eV. The adsorption energy of the free Zn-PcS molecule should be smaller than this value, since the free Zn-PcS molecule should be more stable. For comparison purposes, we observe that

the adsorption energies of hexadecafluorophthalocyanine on monolayer and bilayer graphene are 3.19eV and 3.17eV respectively.¹⁹⁸ At these energies, hexadecafluorophthalocyanine can form uniform overlayers on graphene. Experimentally, only individual Zn-PcS molecules were found adsorbed to the surface, and adsorptions were only observed on bi-layer graphene. We believe that the low adsorption energy is the reason. Zn-PcS does not have a planar structure, which makes it unfavorable for the π - π interaction. In turn, this means that the molecule cannot be effectively stabilized by the substrate. Furthermore, the three-dimensional sulfonic acid group does not provide a convenient orientation for hydrogen bonding of Zn-PcS molecules. This means the molecule cannot be effectively stabilized by another neighboring one. The bi-layer graphene sheets are smoother than mono-layer sheets, and we believe that this difference offers the possibility of having some Zn-PcS adsorbed on bi-layer graphene sheets but not on mono-layer sheets.

To study the effect of Zn-PcS adsorption on the Dirac point, the DOS of the adsorbed system was studied both experimentally and theoretically.¹⁷⁰ In STM/STS experiments, the local DOS is measured by a dI/dV curve. With the STM tip pinned to the molecule, applied voltage can be varied, and the resulting change in the electrical current is recorded to reflect the DOS of that particular point on the molecule. It was concluded (see Figure 29) that the dI/dV curves measured on the bi-layer graphene exhibit a characteristic dip at about 0.3 eV below the Fermi level. The dip is known to originate from the band gap opening around the K-point.²⁰² After the Zn-PcS molecule were adsorbed on the surface, this characteristic dip disappears. This suggests that the Zn-PcS molecule has

states that energetically coincide with the band gap of the bilayer graphene and promote higher tunneling rates at around -0.3eV .

In order to explain the disappearance of the dip in the dI/dV curve, we analyzed the DOS curves produced by the simulation.¹⁷⁰ In the theoretical calculations, the total DOS are calculated using all atoms in the cell, whereas the local DOS only contains the contribution from a particular set of atoms. We calculated both DOS contribution from the Zn-PcS molecule and that from the carbon atoms directly below the Zn-PcS molecule. In order to compare with the experimental result of SiC-supported graphene, the DOS graphs were shifted to the left, so that the Dirac point of monolayer graphene is at 0.4 below the Fermi level. The results are summarized in Figure 30.

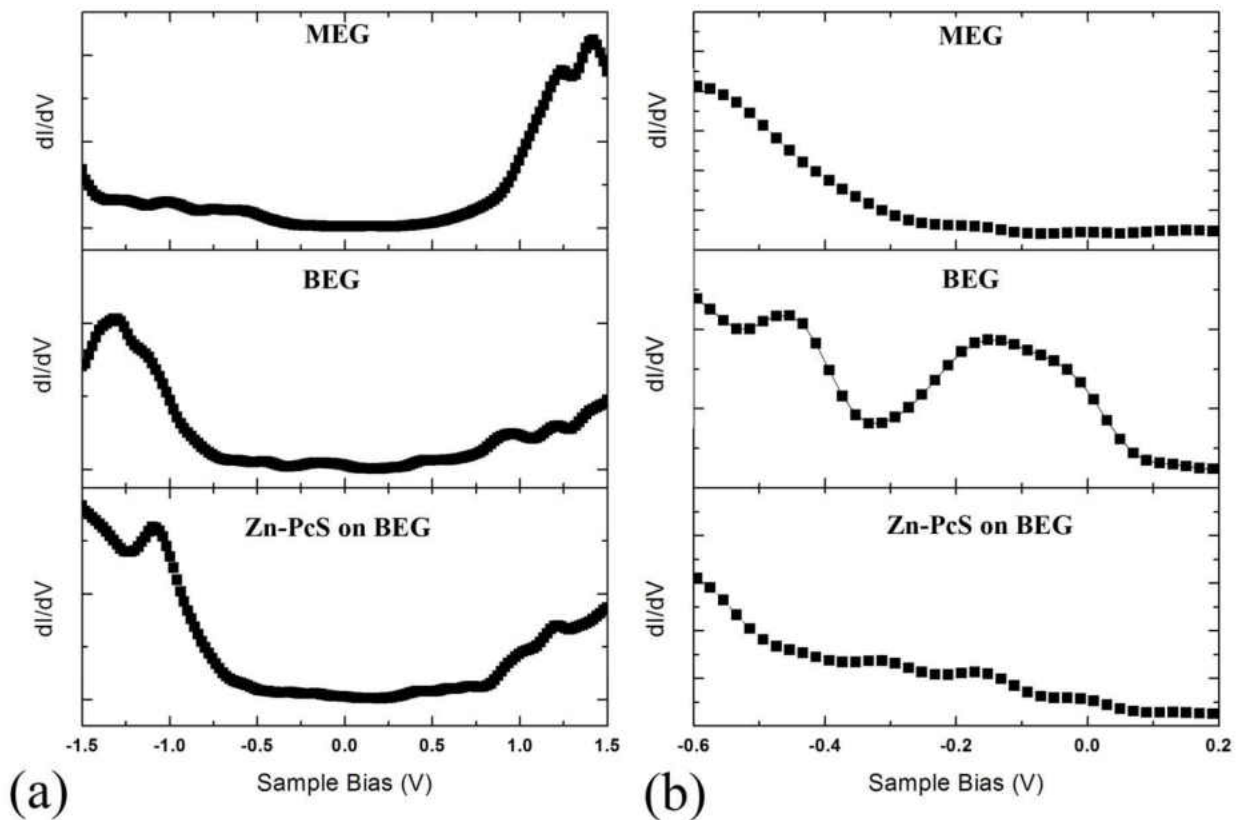


Figure 29. (a) dI/dV curves measured on mono-(top)/bi-layer (middle) epitaxial graphene (MEG/BEG) and on Zn-PcS (bottom) molecule. (b) Section of the same dI/dV curves in (a), near the characteristic dip of BEG ($\sim -0.3\text{eV}$).¹⁷⁰

We found that the DOS around the Dirac point is heavily modified by the adsorbed Zn-PcS molecule.¹⁷⁰ The original Dirac point dip of mono-layer graphene (blue curve) is replaced by a peak (black curve) upon adsorption. Our calculations also show that the highest occupied molecular orbital – lowest unoccupied molecular orbital (HOMO–LUMO) gap of the Zn-PcS molecule is about 1.4 eV, which corresponds to the gap between the peaks around ~1.2 eV below and 0.18 eV above the Dirac point in the projected DOS of the adsorbed system. The HOMO and LUMO of the Zn-PcS molecule are shown in Figure 31. The LUMO peak happens to line up with the Dirac point of graphene, and the Dirac point disappears as a result. The LUMO of isolated Zn-PcS is by definition an unoccupied orbital. After adsorption it is below the Fermi level, meaning that it is partially occupied. This suggests that there must be some charge transfer from graphene to the molecule. To prove this, we also performed a calculation to analyze the charge transfer upon adsorption.

Figure 32 shows the charge transfer between the molecule and graphene.¹⁷⁰ The red bubbles represent electron accumulation, and the blue ones represent electron depletion. It was found that the molecule is mostly negatively charged, while the graphene surface is largely positively charged. The transferred charge mainly localizes around the central Zn atom and the sulfonic acid groups on the perimeter of the molecule (see Figure 32a and 32b). The charge-density difference is integrated in the x-y planes normal to the graphene surface, and plotted along the z direction. This plot shows a small charge transfer (approx.

0.22e) from graphene to the molecule (see Figure 32c). Therefore, the Dirac point of the graphene under Zn-PcS does not exhibit any noticeable shift.

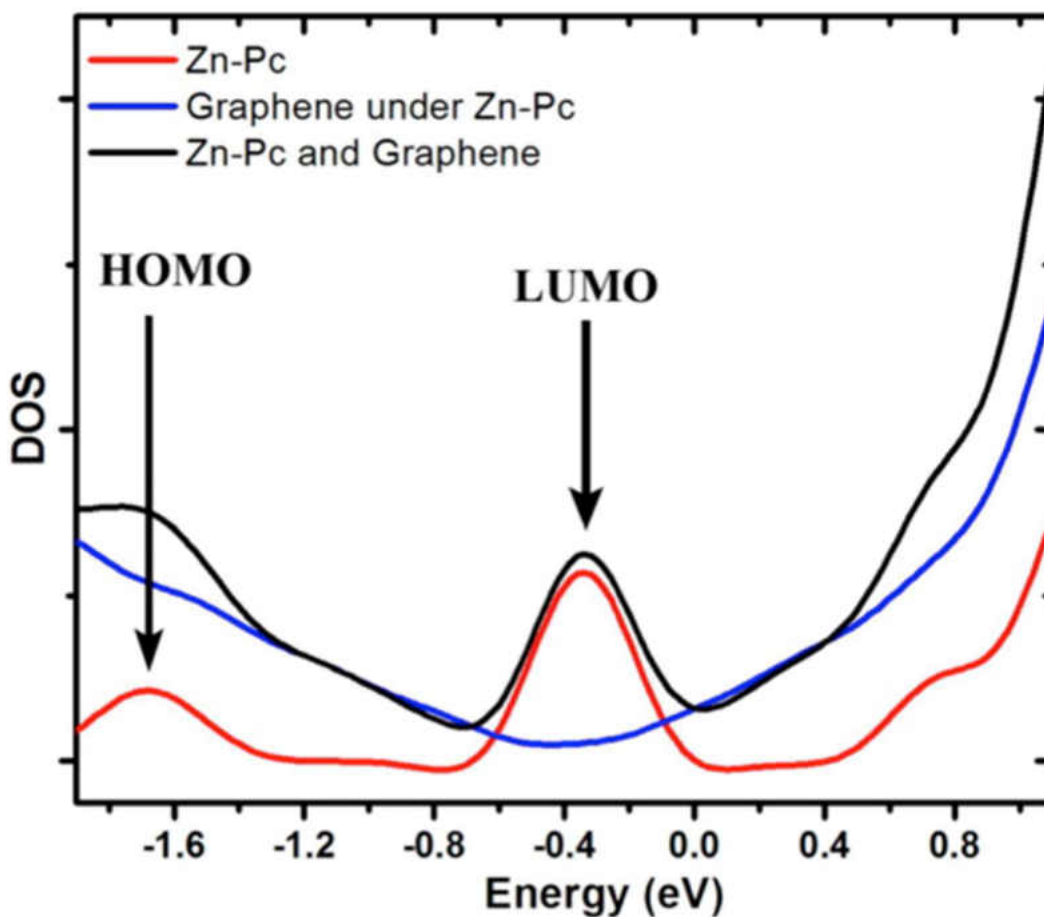
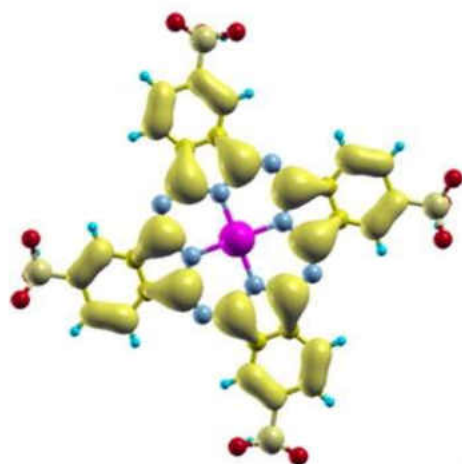


Figure 30. Total DOS (black solid line), projected DOS on the Zn-PcS molecule (red solid line) and projected DOS on graphene (solid blue line). HOMO and LUMO of Zn-PcS molecule are indicated by arrows. In order to simulate the charging effect of the underlying SiC surface, the curves are shifted so that the Dirac point of MEG is at 0.4 eV below the Fermi level.¹⁷⁰

HOMO



LUMO

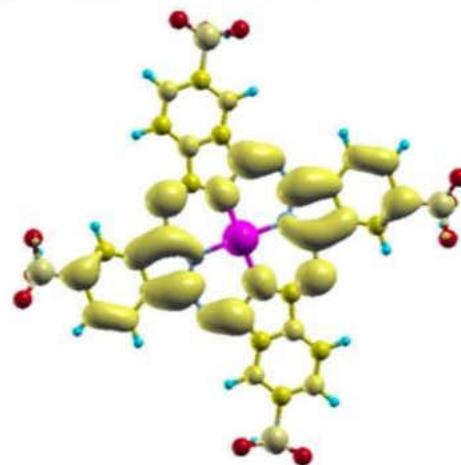


Figure 31. HOMO and LUMO of a Zn-PcS molecule adsorbed on graphene. ¹⁷⁰

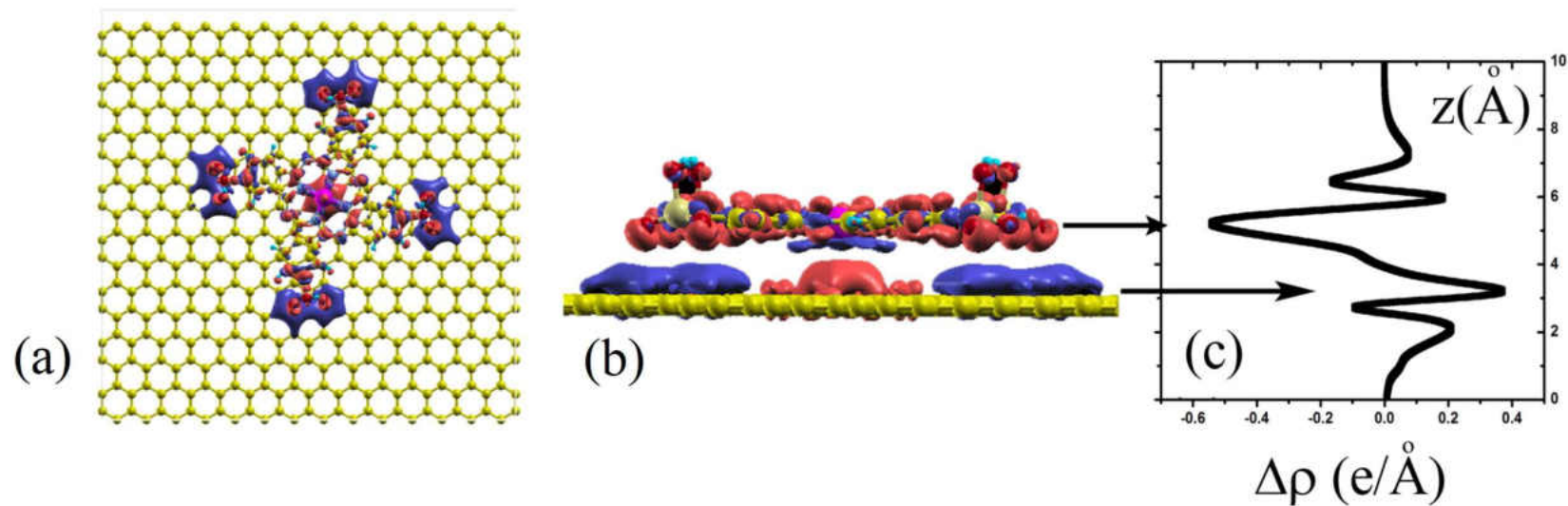


Figure 32. (a) top view and (b) side view of the charge density difference on Zn-PcS adsorbed on graphene system at contour levels of $\pm 0.0003 e/Ry^3$. The blue/black and red/gray bubbles represent regions with electron depletion and accumulation, respectively. (c) The plane-averaged charge density difference along the direction normal to the graphene surface. Arrows are drawn to guide the eye and they correspond to the position of graphene and the Zn-PcS molecule. ¹⁷⁰

Conclusions

In order to understand the adsorption of Zn-PcS on bi-layer graphene observed experimentally with STM/STS, theoretical calculations with the PBE density functional were performed using the plane wave basis set with pseudopotentials. It was found that the adsorption energy of Zn-PcS is very low on mono-layer graphene, which explains why the experimental surface coverage is very low and only adsorption on bi-layer graphene was observed. It was also found that the LUMO orbital of Zn-PcS overlaps with the Dirac point of monolayer graphene, which explains the experimental finding that the characteristic dip of bi-layer graphene at -0.3eV disappears upon adsorption. It was also calculated that there is charge transfer from graphene to the molecule so that the molecule is partially negatively charged.

REFERENCES

- (1) Thiel, W. Semiempirical Quantum–chemical Methods. *Wiley Interdiscip. Rev. Comput. Mol. Sci.* **2014**, *4* (2), 145–157.
- (2) Hartree, D. R. The Wave Mechanics of an Atom with a Non-Coulomb Central Field. Part I. Theory and Methods. *Math. Proc. Cambridge Philos. Soc.* **1928**, *24* (1), 89.
- (3) Fock, V. Näherungsmethode Zur Lösung Des Quantenmechanischen Mehrkörperproblems. *Zeitschrift für Phys.* **1930**, *61* (1–2), 126–148.
- (4) Roothaan, C. C. J. New Developments in Molecular Orbital Theory. *Rev. Mod. Phys.* **1951**, *23* (2), 69–89.
- (5) Becke, A. D. Perspective: Fifty Years of Density-Functional Theory in Chemical Physics. *J. Chem. Phys.* **2014**, *140* (18), 18A301.
- (6) Brillouin, L. Les Problèmes de Perturbations et Les Champs Self-Consistents. *J. Phys. le Radium* **1932**, *3* (9), 373–389.
- (7) Møller, C.; Plesset, M. S. Note on an Approximation Treatment for Many-Electron Systems. *Phys. Rev.* **1934**, *46* (7), 618–622.
- (8) Andersson, K.; Malmqvist, P.; Roos, B. O. Second-order Perturbation Theory with

- a Complete Active Space Self-consistent Field Reference Function. *J. Chem. Phys.* **1992**, *96* (2), 1218–1226.
- (9) Jiang, W.; Khait, Y. G.; Hoffmann, M. R. Configuration-Driven Unitary Group Approach for Generalized Van Vleck Variant Multireference Perturbation Theory †. *J. Phys. Chem. A* **2009**, *113* (16), 4374–4380.
- (10) Schmidt, M. W.; Gordon, M. S. THE CONSTRUCTION AND INTERPRETATION OF MCSCF WAVEFUNCTIONS. *Annu. Rev. Phys. Chem.* **1998**, *49* (1), 233–266.
- (11) Shavitt, I. The Method of Configuration Interaction. In *Methods of Electronic Structure Theory*; Springer US: Boston, MA, 1977; pp 189–275.
- (12) Paldus, J.; Čížek, J.; Saute, M.; Laforgue, A. Correlation Problems in Atomic and Molecular Systems. VI. Coupled-Cluster Approach to Open-Shell Systems. *Phys. Rev. A* **1978**, *17* (3), 805–815.
- (13) Čížek, J. On the Correlation Problem in Atomic and Molecular Systems. Calculation of Wavefunction Components in Ursell-Type Expansion Using Quantum-Field Theoretical Methods. *J. Chem. Phys.* **1966**, *45* (11), 4256–4266.
- (14) Szalay, P. G. Multireference Averaged Quadratic Coupled-Cluster (MR-AQCC) Method Based on the Functional of the Total Energy. *Chem. Phys.* **2008**, *349* (1–3), 121–125.
- (15) Gdanitz, R. J.; Ahlrichs, R. The Averaged Coupled-Pair Functional (ACPF): A Size-Extensive Modification of MR CI(SD). *Chem. Phys. Lett.* **1988**, *143* (5), 413–420.
- (16) Szalay, P. G.; Bartlett, R. J. Multi-Reference Averaged Quadratic Coupled-Cluster

- Method: A Size-Extensive Modification of Multi-Reference CI. *Chem. Phys. Lett.* **1993**, *214* (5), 481–488.
- (17) van Duin, A. C. T.; Dasgupta, S.; Lorant, F.; Goddard, W. A. ReaxFF: A Reactive Force Field for Hydrocarbons. *J. Phys. Chem. A* **2001**, *105* (41), 9396–9409.
- (18) Jorgensen, W. L.; Maxwell, D. S.; Tirado-Rives, J. Development and Testing of the OPLS All-Atom Force Field on Conformational Energetics and Properties of Organic Liquids. *J. Am. Chem. Soc.* **1996**, *118* (45), 11225–11236.
- (19) Cramer, C. J. *Essentials of Computational Chemistry: Theories and Models*; Wiley, 2004.
- (20) Helgaker, T.; Jørgensen, P.; Olsen, J. *Molecular Electronic-Structure Theory*; Wiley, 2000.
- (21) Szabo, A.; Ostlund, N. S. *Modern Quantum Chemistry: Introduction to Advanced Electronic Structure Theory*; Dover Publications, 1996.
- (22) Jensen, F. *Introduction to Computational Chemistry*; John Wiley & Sons, 2007.
- (23) Hohenberg, P.; Kohn, W. Inhomogeneous Electron Gas. *Phys. Rev.* **1964**, *136* (3B), B864–B871.
- (24) Kohn, W.; Sham, L. J. Self-Consistent Equations Including Exchange and Correlation Effects. *Phys. Rev.* **1965**, *140* (4A), A1133–A1138.
- (25) Ceperley, D. M.; Alder, B. J. Ground State of the Electron Gas by a Stochastic Method. *Phys. Rev. Lett.* **1980**, *45* (7), 566–569.
- (26) Perdew, J. P.; Burke, K.; Ernzerhof, M. Generalized Gradient Approximation Made Simple. *Phys. Rev. Lett.* **1996**, *77* (18), 3865–3868.
- (27) Perdew, J. P.; Schmidt, M. W. Jacob's Ladder of Density Functional

- Approximations for the Exchange- Correlation Energy. In *Density Functional Theory and Its Applications to Materials*; 2001; pp 1–20.
- (28) Tao, J.; Perdew, J. P.; Staroverov, V. N.; Scuseria, G. E. Climbing the Density Functional Ladder: Nonempirical Meta–Generalized Gradient Approximation Designed for Molecules and Solids. *Phys. Rev. Lett.* **2003**, *91* (14), 146401.
- (29) Zhao, Y.; Truhlar, D. G. Density Functionals with Broad Applicability in Chemistry. *Acc. Chem. Res.* **2008**, *41* (2), 157–167.
- (30) Zhao, Y.; Schultz, N. E.; Truhlar, D. G. Design of Density Functionals by Combining the Method of Constraint Satisfaction with Parametrization for Thermochemistry, Thermochemical Kinetics, and Noncovalent Interactions. *J. Chem. Theory Comput.* **2006**, *2* (2), 364–382.
- (31) Zhao, Y.; Truhlar, D. G. A New Local Density Functional for Main-Group Thermochemistry, Transition Metal Bonding, Thermochemical Kinetics, and Noncovalent Interactions. *J. Chem. Phys.* **2006**, *125* (19), 194101.
- (32) Zhao, Y.; Truhlar, D. G. The M06 Suite of Density Functionals for Main Group Thermochemistry, Thermochemical Kinetics, Noncovalent Interactions, Excited States, and Transition Elements: Two New Functionals and Systematic Testing of Four M06-Class Functionals and 12 Other Function. *Theor. Chem. Acc.* **2008**, *120* (1–3), 215–241.
- (33) Stephens, P. J.; Devlin, F. J.; Chabalowski, C. F.; Frisch, M. J. Ab Initio Calculation of Vibrational Absorption and Circular Dichroism Spectra Using Density Functional Force Fields. *J. Phys. Chem.* **1994**, *98* (45), 11623–11627.
- (34) Becke, A. D. Density-Functional Exchange-Energy Approximation with Correct

- Asymptotic Behavior. *Phys. Rev. A* **1988**, *38* (6), 3098–3100.
- (35) Lee, C.; Yang, W.; Parr, R. G. Development of the Colle-Salvetti Correlation-Energy Formula into a Functional of the Electron Density. *Phys. Rev. B* **1988**, *37* (2), 785–789.
- (36) Adamo, C.; Cossi, M.; Barone, V. An Accurate Density Functional Method for the Study of Magnetic Properties: The PBE0 Model. *J. Mol. Struct. THEOCHEM* **1999**, *493* (1), 145–157.
- (37) Laming, G. J.; Termath, V.; Handy, N. C. A General Purpose Exchange-correlation Energy Functional. *J. Chem. Phys.* **1993**, *99* (11), 8765–8773.
- (38) Chai, J.-D.; Head-Gordon, M.; Laming, G. J.; Shao, Y.; Head-Gordon, M.; Brown, S. T.; Gilbert, A. T. B.; Slipchenko, L. V.; Levchenko, S. V.; O’Neill, D. P.; et al. Long-Range Corrected Hybrid Density Functionals with Damped Atom–atom Dispersion Corrections. *Phys. Chem. Chem. Phys.* **2008**, *10* (44), 6615.
- (39) Yamanaka, S.; Yamaki, D.; Shigeta, Y.; Nagao, H.; Yamaguchi, K. Noncollinear Spin Density Functional Theory for Spin-Frustrated and Spin-Degenerate Systems. *Int. J. Quantum Chem.* **2001**, *84* (6), 670–676.
- (40) Van Wüllen, C. Spin Densities in Two-Component Relativistic Density Functional Calculations: Noncollinear versus Collinear Approach. *J. Comput. Chem.* **2002**, *23* (8), 779–785.
- (41) Ghosh, S.; Sonnenberger, A. L.; Hoyer, C. E.; Truhlar, D. G.; Gagliardi, L. Multiconfiguration Pair-Density Functional Theory Outperforms Kohn–Sham Density Functional Theory and Multireference Perturbation Theory for Ground-State and Excited-State Charge Transfer. *J. Chem. Theory Comput.* **2015**, *11* (8),

3643–3649.

- (42) Filatov, M.; Shaik, S. Spin-Restricted Density Functional Approach to the Open-Shell Problem. *Chem. Phys. Lett.* **1998**, *288* (5), 689–697.
- (43) Gräfenstein, J.; Kraka, E.; Cremer, D. Density Functional Theory for Open-Shell Singlet Biradicals. *Chem. Phys. Lett.* **1998**, *288* (5), 593–602.
- (44) Khait, Y. G.; Hoffmann, M. R. Multireference Spin-Adapted Variant of Density Functional Theory. *J. Chem. Phys.* **2004**, *120* (11), 5005–5016.
- (45) Petersilka, M.; Gossmann, U. J.; Gross, E. K. U. Excitation Energies from Time-Dependent Density-Functional Theory. *Phys. Rev. Lett.* **1996**, *76* (8), 1212–1215.
- (46) van Leeuwen, R. Causality and Symmetry in Time-Dependent Density-Functional Theory. *Phys. Rev. Lett.* **1998**, *80* (6), 1280–1283.
- (47) Runge, E.; Gross, E. K. U. Density-Functional Theory for Time-Dependent Systems. *Phys. Rev. Lett.* **1984**, *52* (12), 997–1000.
- (48) Vignale, G. Real-Time Resolution of the Causality Paradox of Time-Dependent Density-Functional Theory. *Phys. Rev. A* **2008**, *77* (6), 62511.
- (49) Shao, Y.; Head-Gordon, M.; Krylov, A. I. The Spin-Flip Approach within Time-Dependent Density Functional Theory: Theory and Applications to Diradicals. *J. Chem. Phys.* **2003**, *118* (11), 4807–4818.
- (50) Grimme, S.; Antony, J.; Ehrlich, S.; Krieg, H. A Consistent and Accurate Ab Initio Parametrization of Density Functional Dispersion Correction (DFT-D) for the 94 Elements H-Pu. *J. Chem. Phys.* **2010**, *132* (15), 154104.
- (51) Grimme, S. Density Functional Theory with London Dispersion Corrections. *Wiley Interdiscip. Rev. Comput. Mol. Sci.* **2011**, *1* (2), 211–228.

- (52) Lignères, V. L.; Carter, E. A. An Introduction to Orbital-Free Density Functional Theory. In *Handbook of Materials Modeling*; Springer Netherlands: Dordrecht, 2005; pp 137–148.
- (53) Anisimov; Zaanen; Andersen. Band Theory and Mott Insulators: Hubbard U instead of Stoner I. *Phys. Rev. B. Condens. Matter* **1991**, *44* (3), 943–954.
- (54) Elstner, M.; Seifert, G. Density Functional Tight Binding. *Philos. Trans. R. Soc. London A Math. Phys. Eng. Sci.* **2014**, *372* (2011).
- (55) Elstner, M.; Porezag, D.; Jungnickel, G.; Elsner, J.; Haugk, M.; Frauenheim, T.; Suhai, S.; Seifert, G. Self-Consistent-Charge Density-Functional Tight-Binding Method for Simulations of Complex Materials Properties. *Phys. Rev. B* **1998**, *58* (11), 7260–7268.
- (56) Yang; Yu, H.; York, D.; Cui, Q.; Elstner, M. Extension of the Self-Consistent-Charge Density-Functional Tight-Binding Method: Third-Order Expansion of the Density Functional Theory Total Energy and Introduction of a Modified Effective Coulomb Interaction. *J. Phys. Chem. A* **2007**, *111* (42), 10861–10873.
- (57) Seifert, G.; Porezag, D.; Frauenheim, T. Calculations of Molecules, Clusters, and Solids with a Simplified LCAO-DFT-LDA Scheme. *Int. J. Quantum Chem.* **1996**, *58* (2), 185–192.
- (58) Porezag, D.; Frauenheim, T.; Köhler, T.; Seifert, G.; Kaschner, R. Construction of Tight-Binding-like Potentials on the Basis of Density-Functional Theory: Application to Carbon. *Phys. Rev. B* **1995**, *51* (19), 12947–12957.
- (59) Li, L.; Snyder, J. C.; Pelaschier, I. M.; Huang, J.; Niranjana, U.-N.; Duncan, P.; Rupp, M.; Müller, K.-R.; Burke, K. Understanding Machine-Learned Density

- Functionals. *Int. J. Quantum Chem.* **2014**, *116* (11), 819–833.
- (60) Snyder, J. C.; Rupp, M.; Hansen, K.; Müller, K.-R.; Burke, K. Finding Density Functionals with Machine Learning. *Phys. Rev. Lett.* **2012**, *108* (25), 253002.
- (61) Epstein, S. T. *The Variation Method in Quantum Chemistry*; Academic Press, 1974.
- (62) SHAVITT, I. The History and Evolution of Configuration Interaction. *Mol. Phys.* **1998**, *94* (1), 3–17.
- (63) Khait, Y. G.; Song, J.; Hoffmann, M. R. Macroconfigurations in Molecular Electronic Structure Theory. *Int. J. Quantum Chem.* **2004**, *99* (4), 210–220.
- (64) Lanczos, C. An Iteration Method for the Solution of the Eigenvalue Problem of Linear Differential and Integral Operators. *J. Reseach Natl. Bur. Stand.* **1950**, *45*, 255–282.
- (65) Arnoldi, W. The Principle of Minimized Iterations in the Solution of the Matrix Eigenvalue Problem. *Q. Appl. Math.* **1951**.
- (66) Davidson, E. R. The Iterative Calculation of a Few of the Lowest Eigenvalues and Corresponding Eigenvectors of Large Real-Symmetric Matrices. *J. Comput. Phys.* **1975**, *17* (1), 87–94.
- (67) Roos, B. A New Method for Large-Scale CI Calculations. *Chem. Phys. Lett.* **1972**, *15* (2), 153–159.
- (68) Buenker, R.; Burton, P. Proceedings of the Workshop on Quantum Chemistry and Molecular Physics, Wollongong, Australia. **1980**.
- (69) Krebs, S.; Buenker, R. J. A New Table-direct Configuration Interaction Method for the Evaluation of Hamiltonian Matrix Elements in a Basis of Linear

- Combinations of Spin-adapted Functions. *J. Chem. Phys.* **1995**, *103* (13), 5613–5629.
- (70) Pauncz, R. *The Symmetric Group in Quantum Chemistry*; CRC Press, 1995.
- (71) Duch, W.; Karwowski, J. Symmetric Group Approach to Configuration Interaction Methods. *Comput. Phys. Reports* **1985**, *2* (3), 93–170.
- (72) Duch, W.; Karwowski, J. Symmetric Group Graphical Approach to the Direct Configuration Interaction Method. *Int. J. Quantum Chem.* **1982**, *22* (4), 783–824.
- (73) Guldberg, A.; Rettrup, S.; Bendazzoli, G. L.; Palmieri, P. A New Symmetric Group Program for Direct Configuration Interaction Studies of Molecules. *Int. J. Quantum Chem.* **1987**, *32* (S21), 513–521.
- (74) Paldus, J. Unitary-Group Approach to the Many-Electron Correlation Problem: Relation of Gelfand and Weyl Tableau Formulations. *Phys. Rev. A* **1976**, *14* (5), 1620–1625.
- (75) Gould, M. D.; Paldus, J. Unitary Group Approach to General System Partitioning. I. Calculation of $U(n=n_1+n_2): U(n_1) \times U(n_2)$ Reduced Matrix Elements and Reduced Wigner Coefficients. *Int. J. Quantum Chem.* **1986**, *30* (3), 327–363.
- (76) Shavitt, I. No Title. In *Lecture Notes in Chemistry*; Heniz, J., Ed.; Science, 1988; p 300.
- (77) Shavitt, I. Mathematical Frontiers in Computational Chemical Physics. In *Mathematical Frontiers in Computational Chemical Physics*; Truhlar, D. G., Ed.; Springer: New York, 1988; p 300.
- (78) Paldus, J.; Boyle, M. J. Unitary Group Approach to the Many-Electron Correlation Problem via Graphical Methods of Spin Algebras. *Phys. Scr.* **1980**, *21* (3–4), 295–

311.

- (79) Brooks, B. R.; Laidig, W. D.; Saxe, P.; Handy, N. C.; Schaefer, H. F. The Loop-Driven Graphical Unitary Group Approach: A Powerful Method for the Variational Description of Electron Correlation. *Phys. Scr.* **1980**, *21* (3–4), 312–322.
- (80) Brooks, B. R.; Schaefer, H. F. The Graphical Unitary Group Approach to the Electron Correlation Problem. Methods and Preliminary Applications. *J. Chem. Phys.* **1979**, *70* (11), 5092–5106.
- (81) Brooks, B. R.; Schaefer, H. F. The BERKELEY System. III. General Configuration-Interaction Methods for Open-Shell Molecular Electronic States. *Int. J. Quantum Chem.* **1978**, *14* (5), 603–612.
- (82) Siegbahn, P. E. M. Generalizations of the Direct CI Method Based on the Graphical Unitary Group Approach. II. Single and Double Replacements from Any Set of Reference Configurations. *J. Chem. Phys.* **1980**, *72* (3), 1647–1656.
- (83) Siegbahn, P. E. M. Generalizations of the Direct CI Method Based on the Graphical Unitary Group Approach. I. Single Replacements from a Complete CI Root Function of Any Spin, First Order Wave Functions. *J. Chem. Phys.* **1979**, *70* (12), 5391–5397.
- (84) Shavitt, I. The Graphical Unitary Group Approach and Its Application to Direct Configuration Interaction Calculations. In *Lecture Notes in Chemistry*; Springer Berlin Heidelberg, 1981; p 51.
- (85) Wang, Y.; Gan, Z.; Su, K.; Wen, Z. An Improved Externally Contracted CI Method. *Chem. Phys. Lett.* **1999**, *312* (2), 277–283.

- (86) Wang, Y.; Wen, Z.; Zhang, Z.; Du, Q. New Realization of Loop Driven Direct CI. *J. Comput. Chem.* **1992**, *13* (2), 187–198.
- (87) Shavitt, I. Matrix Element Evaluation in the Unitary Group Approach to the Electron Correlation Problem. *Int. J. Quantum Chem. Symp.* **1978**, *12* (S12), 5–32.
- (88) Shavitt, I. Graph Theoretical Concepts for the Unitary Group Approach to the Many-Electron Correlation Problem. *Int. J. Quantum Chem.* **1977**, *12* (11 S), 131–148.
- (89) Paldus, J. Group Theoretical Approach to the Configuration Interaction and Perturbation Theory Calculations for Atomic and Molecular Systems. *J. Chem. Phys.* **1974**, *61* (12), 5321–5330.
- (90) Paldus, J. A Pattern Calculus for the Unitary Group Approach to the Electronic Correlation Problem. *Int. J. Quantum Chem.* **1975**, *9* (9 S), 165–174.
- (91) Kedziora, Gary Steven, J.; Shavitt, I. The Graphical Unitary Group Approach to Configuration Interaction Calculations : An Application to the Dipole Moment and Potential Energy Surface of the Water Molecule, Ohio State University, 1994.
- (92) Saxe, P.; Fox, D. J.; Schaefer, H. F.; Handy, N. C. The Shape-driven Graphical Unitary Group Approach to the Electron Correlation Problem. Application to the Ethylene Molecule. *J. Chem. Phys.* **1982**, *77* (11), 5584–5592.
- (93) Lischka, H.; Shepard, R.; Brown, F. B.; Shavitt, I. New Implementation of the Graphical Unitary Group Approach for Multireference Direct Configuration Interaction Calculations. *Int. J. Quantum Chem.* **2009**, *20* (S15), 91–100.
- (94) Löwdin, P.-O. Studies in Perturbation Theory. *J. Mol. Spectrosc.* **1963**, *10* (1–6), 12–33.

- (95) Bravais, A. On the Systems Formed by Points Regularly Distributed on a Plane or in Space. **1949**.
- (96) Dovesi, R.; Civalieri, B.; Orlando, R.; Roetti, C.; Saunders, V. R. {em Ab Initio} Quantum Simulation in Solid State Chemistry. *Rev. Comput. Chem.* **2005**, *21*, 1–125.
- (97) Chelikowsky, J. R.; Cohen, M. L. Electronic Structure of Silicon. *Phys. Rev. B* **1974**, *10* (12), 5095–5107.
- (98) Collin, G. J.; Deslauriers, H.; De Mare, G. R.; Poirier, R. A. The 21 3.8-Nm Photochemlstry of Gaseous 1,3-Butadiene and the Structure of Some C₃H₃ Radicals. *J. Phys. Chem* **1990**, *94*, 134–141.
- (99) Mebel, A. M.; Jackson, W. M.; Chang, A. H. H.; Lin, S. H. Photodissociation Dynamics of Propyne and Allene: A View from Ab Initio Calculations of the C₃H_n (N = 1~4) Species and the Isomerization Mechanism for C₃H₂. *J. Am. Chem. Soc.* **1998**, *120* (23), 5751–5763.
- (100) Westmoreland, P. R.; Dean, A. M.; Howard, J. B.; Longwellt, J. P. Forming Benzene in Flames by Chemically Activated Isomerization. *J. Phys. Chem* **1989**, *93*, 8171–8180.
- (101) Gilbert, T.; Pfab, R.; Fischer, I.; Chen, P. The Zero Kinetic Energy Photoelectron Spectrum of the Propargyl Radical, C₃H₃. *J. Chem. Phys.* **2000**, *112* (6), 2575–2578.
- (102) Miller, J. A.; Melius, C. F. Kinetic and Thermodynamic Issues in the Formation of Aromatic Compounds in Flames of Aliphatic Fuels. *Combust. Flame* **1992**, *91* (1), 21–39.

- (103) Gladstone, G. R.; Allen, M.; Yung, Y. L. Hydrocarbon Photochemistry in the Upper Atmosphere of Jupiter. *Icarus* **1996**, *119* (1), 1–52.
- (104) Hemberger, P.; Lang, M.; Noller, B.; Fischer, I.; Alcaraz, C.; Cunha de Miranda, B. K.; Garcia, G. A.; Soldi-Lose, H. Photoionization of Propargyl and Bromopropargyl Radicals: A Threshold Photoelectron Spectroscopic Study. *J. Phys. Chem. A* **2011**, *115* (11), 2225–2230.
- (105) Gao, H.; Xu, Y.; Yang, L.; Lam, C.-S.; Wang, H.; Zhou, J.; Ng, C. Y. High-Resolution Threshold Photoelectron Study of the Propargyl Radical by the Vacuum Ultraviolet Laser Velocity-Map Imaging Method. *J. Chem. Phys.* **2011**, *135* (22), 224304.
- (106) Savee, J. D.; Soorkia, S.; Welz, O.; Selby, T. M.; Taatjes, C. A.; Osborn, D. L. Absolute Photoionization Cross-Section of the Propargyl Radical. *J. Chem. Phys.* **2012**, *136* (13), 134307.
- (107) Gilbert, T.; Fischer, I.; Chen, P. Zero Kinetic Energy Photoelectron Spectra of the Allyl Radical, C₃H₅. *J. Chem. Phys.* **2000**, *113* (2), 561–566.
- (108) Yuan, L.; DeSain, J.; Curl, R. F. Analysis of the K-Subband Structure of the Fundamental of Propargyl Radical H₂CCCH. *J. Mol. Spectrosc.* **1998**, *187* (1), 102–108.
- (109) Botschwina, P.; Oswald, R. Calculated Photoelectron Spectra of Isotopomers of the Propargyl Radical (H₂C₃H): An Explicitly Correlated Coupled Cluster Study. *Chem. Phys.* **2010**, *378* (1–3), 4–10.
- (110) Lau, K.-C.; Ng, C. Y. Note: Accurate *Ab Initio* Predictions of Ionization Energies of Propargyl and Allyl Radicals: Revisited. *J. Chem. Phys.* **2011**, *135* (24),

246101.

- (111) Honjou, H.; Yoshimine, M.; Pacansky, J. Theoretical Studies on the Ground State and Low-Lying Doublet Excited States of the Propargyl Radical. *J. Phys. Chem.* **1987**, *91*, 4455–4459.
- (112) Botschwina, P.; Oswald, R.; Flugge, J.; Horn, M. A Theoretical Investigation of the Propargyl Radical and Its Cation. *Zeitschrift für Phys. Chemie* **1995**, *188*, 29–43.
- (113) Deyerl, H.-J.; Fischer, I.; Chen, P. Photodissociation Dynamics of the Propargyl Radical. *J. Chem. Phys.* **1999**, *111* (8), 3441–3448.
- (114) Klippenstein, S. J.; Miller, J. A.; Jasper, A. W. Kinetics of Propargyl Radical Dissociation. *J. Phys. Chem. A* **2015**, *119* (28), 7780–7791.
- (115) Nguyen, T. L.; Mebel, A. M.; Lin, S. H.; Kaiser, R. I. Product Branching Ratios of the $C(3P) + C_2H_3(2A')$ and $CH(2\Pi) + C_2H_2(1\Sigma_g^+)$ Reactions and Photodissociation of $H_2CC\equiv CH(2B)$ at 193 and 242 Nm: An Ab Initio/RRKM Study. *J. Phys. Chem. A* **2001**, *105* (51), 11549–11559.
- (116) Castiglioni, L.; Vukovic, S.; Crider, P. E.; Lester, W. A.; Neumark, D. M.; Moore, D. T.; Neumark, D. M. Intramolecular Competition in the Photodissociation of C_3D_3 Radicals at 248 and 193 Nm. *Phys. Chem. Chem. Phys.* **2010**, *12* (36), 10714.
- (117) Vázquez, J.; Harding, M. E.; Gauss, J.; Stanton, J. F. High-Accuracy Extrapolated Ab Initio Thermochemistry of the Propargyl Radical and the Singlet C_3H_2 Carbenes. *J. Phys. Chem. A* **2009**, *113* (45), 12447–12453.
- (118) Kochi, J. K.; Krusic, P. J. Electron Spin Resonance of Free Radicals from

- Acetylenes and Allenes. *J. Am. Chem. Soc.* **1970**, *92* (13), 4110–4114.
- (119) Robinson, M. S.; Polak, M. L.; Bierbaum, V. M.; DePuy, C. H.; Lineberger, W. C. Experimental Studies of Allene, Methylacetylene, and the Propargyl Radical: Bond Dissociation Energies, Gas-Phase Acidities, and Ion-Molecule Chemistry. *J. Am. Chem. Soc.* **1995**, *117*, 6766–6778.
- (120) Wyss, M.; Riaplov, E.; Maier, J. P. Electronic and Infrared Spectra of $\text{H}_2\text{C}_3\text{H}^+$ and Cyclic C_3H_3^+ in Neon Matrices. *J. Chem. Phys.* **2001**, *114* (23), 10355–10361.
- (121) Oakes, J. M.; Ellison, G. B. Photoelectron Spectroscopy of the Allenyl Ion $\text{CH}_2=\text{C}=\text{CH}$. *J. Am. Chem. Soc.* **1983**, *105*, 2969–2975.
- (122) Fahr, A.; Laufer, A. H. UV-Absorption Spectra of the Radical Transients Generated from the 193-Nm Photolysis of Allene, Propyne, and 2-Butyne. *J. Phys. Chem. A* **2005**, *109* (11), 2534–2539.
- (123) Fahr, A.; Hassanzadeh, P.; Laszlo, B.; Huie, R. E. Ultraviolet Absorption and Cross Sections of Propargyl (C_3H_3) Radicals in the 230–300 Nm Region. *Chem. Phys.* **1997**, *215* (1), 59–66.
- (124) Goncher, S. J.; Moore, D. T.; Sveum, N. E.; Neumark, D. M. Photofragment Translational Spectroscopy of Propargyl Radicals at 248nm. *J. Chem. Phys.* **2008**, *128* (11), 114303.
- (125) Einfeld, W.; Lindh, R.; Malmqvist, P.-Å.; Veryazov, V.; Widmark, P.-O.; Pierloot, K.; Merchán, M. Ab Initio Calculation of Electronic Absorption Spectra and Ionization Potentials of C_3H_3 Radicals. *Phys. Chem. Chem. Phys.* **2005**, *7* (23), 3924.
- (126) Einfeld, W. Calculation of the Vibrationally Resolved Electronic Absorption

- Spectrum of the Propargyl Radical (H₂CCCH). *J. Phys. Chem. A* **2006**, *110* (11), 3903–3910.
- (127) Zheng, X.; Song, Y.; Zhang, J. Ultraviolet Photodissociation Dynamics of the Propargyl Radical. *J. Phys. Chem. A* **2009**, *113* (16), 4604–4612.
- (128) Crider, P. E.; Castiglioni, L.; Kautzman, K. E.; Neumark, D. M. Photodissociation of the Propargyl and Propynyl (C₃D₃) Radicals at 248 and 193 Nm. *J. Chem. Phys.* **2009**, *130* (4), 44310.
- (129) Khait, Y. G.; Jiang, W.; Hoffmann, M. R. On the Inclusion of Triple and Quadruple Electron Excitations into MRCISD for Multiple States. *Chem. Phys. Lett.* **2010**, *493* (1), 1–10.
- (130) Khait, Y. G.; Song, J.; Hoffmann, M. R. Perturbative Triple and Quadruple Excitation Corrections to MRCISD. *Chem. Phys. Lett.* **2003**, *372* (5–6), 674–685.
- (131) Hoffmann, M. R. Canonical Van Vleck Quasidegenerate Perturbation Theory with Trigonometric Variables. *J. Phys. Chem.* **1996**, *100* (15), 6125–6130.
- (132) Hoffmann, M. R. Third-Order Complete Active Space Self-Consistent Field Based Generalized Van Vleck Perturbation Theory. *Chem. Phys. Lett.* **1993**, *210* (1–3), 193–200.
- (133) Mbote, Y. E. B.; Khait, Y. G.; Hardel, C.; Hoffmann, M. R. Multireference Generalized Van Vleck Perturbation Theory (GVVPT2) Study of the NCO + HCNO Reaction: Insight into Intermediates [?] *J. Phys. Chem. A* **2010**, *114* (33), 8831–8836.
- (134) Dunning, T. H. Gaussian Basis Sets for Use in Correlated Molecular Calculations. I. The Atoms Boron through Neon and Hydrogen. *J. Chem. Phys.* **1989**, *90* (2),

1007–1023.

- (135) Kendall, R. A.; Dunning, T. H.; Harrison, R. J. Electron Affinities of the First-Row Atoms Revisited. Systematic Basis Sets and Wave Functions. *J. Chem. Phys.* **1992**, *96* (9), 6796–6806.
- (136) Feller, D. Application of Systematic Sequences of Wave Functions to the Water Dimer. *J. Chem. Phys.* **1992**, *96* (8), 6104–6114.
- (137) Feller, D. The Use of Systematic Sequences of Wave Functions for Estimating the Complete Basis Set, Full Configuration Interaction Limit in Water. *J. Chem. Phys.* **1993**, *98* (9), 7059–7071.
- (138) Halkier, A.; Helgaker, T.; Jørgensen, P.; Klopper, W.; Olsen, J. Basis-Set Convergence of the Energy in Molecular Hartree–Fock Calculations. *Chem. Phys. Lett.* **1999**, *302* (5), 437–446.
- (139) Tamukong, P. K.; Theis, D.; Khait, Y. G.; Hoffmann, M. R. GVVPT2 Multireference Perturbation Theory Description of Diatomic Scandium, Chromium, and Manganese. *J. Phys. Chem. A* **2012**, *116* (18), 4590–4601.
- (140) Williams, T. G.; DeYonker, N. J.; Wilson, A. K. Hartree-Fock Complete Basis Set Limit Properties for Transition Metal Diatomics. *J. Chem. Phys.* **2008**, *128* (4), 44101.
- (141) Jiang, W.; Khait, Y. G.; Hoffmann, M. R. MRCISD and GVVPT3 Study of the Low-Lying Electronic States of NO^x. *Mol. Phys.* **2009**, *107* (8–12), 889–897.
- (142) Schwartz, C. Importance of Angular Correlations between Atomic Electrons. *Phys. Rev.* **1962**, *126* (3), 1015–1019.
- (143) Halkier, A.; Helgaker, T.; Jørgensen, P.; Klopper, W.; Koch, H.; Olsen, J.; Wilson,

- A. K. Basis-Set Convergence in Correlated Calculations on Ne, N₂ and H₂O. *Chem. Phys. Lett.* **1998**, 286 (3–4), 243–252.
- (144) Helgaker, T.; Klopper, W.; Koch, H.; Noga, J. Basis-Set Convergence of Correlated Calculations on Water. *J. Chem. Phys.* **1997**, 106 (23), 9639–9646.
- (145) Liu, B.; Yoshimine, M. The Alchemy Configuration Interaction Method. I. The Symbolic Matrix Method for Determining Elements of Matrix Operators. *J. Chem. Phys.* **1981**, 74 (1), 612–616.
- (146) Werner, H.; Knowles, P. J. An Efficient Internally Contracted Multiconfiguration–reference Configuration Interaction Method. *J. Chem. Phys.* **1988**, 89 (9), 5803–5814.
- (147) Siegbahn, P. E. M. The Externally Contracted CI Method Applied to N₂. *Int. J. Quantum Chem.* **1983**, 23 (6), 1869–1889.
- (148) Frisch, M. J.; Trucks, G. W.; Schlegel, H. B.; Scuseria, G. E.; Robb, M. A.; Cheeseman, J. R.; Scalmani, G.; Barone, V.; Petersson, G. A.; Nakatsuji, H.; et al. *Gaussian 16, Revision A.03*; Gaussian, Inc.: Wallingford CT, 2016.
- (149) Schmidt, M. W.; Baldridge, K. K.; Boatz, J. A.; Elbert, S. T.; Gordon, M. S.; Jensen, J. H.; Koseki, S.; Matsunaga, N.; Nguyen, K. A.; Su, S.; et al. General Atomic and Molecular Electronic Structure System. *J. Comput. Chem.* **1993**, 14 (11), 1347–1363.
- (150) Lischka, H.; Müller, T.; Szalay, P.; Shavitt, I.; Pitzer, R. M.; Shepard, R. Columbus—a Program System for Advanced Multireference Theory Calculations. *Wiley Interdiscip. Rev. Comput. Mol. Sci.* **2011**, 1 (2), 191–199.
- (151) Werner, H.-J.; Knowles, P. J.; Knizia, G.; Manby, F. R.; Schütz, M. Molpro: A

- General-Purpose Quantum Chemistry Program Package. *Wiley Interdiscip. Rev. Comput. Mol. Sci.* **2012**, *2* (2), 242–253.
- (152) Carriero, N.; Gelernter, D. Linda in Context. *Commun. ACM* **1989**, *32* (4), 444–458.
- (153) Fletcher, G. D.; Schmidt, M. W.; Bode, B. M.; Gordon, M. S. The Distributed Data Interface in GAMESS. *Comput. Phys. Commun.* **2000**, *128* (1–2), 190–200.
- (154) Kendall, R. A.; Aprà, E.; Bernholdt, D. E.; Bylaska, E. J.; Dupuis, M.; Fann, G. I.; Harrison, R. J.; Ju, J.; Nichols, J. A.; Nieplocha, J.; et al. High Performance Computational Chemistry: An Overview of NWChem a Distributed Parallel Application. *Comput. Phys. Commun.* **2000**, *128* (1–2), 260–283.
- (155) Hoffmann, M. R. A State-Selective Quasidegenerate Perturbation Theory for the Electronic Structure of Molecules. *Chem. Phys. Lett.* **1992**, *195* (2–3), 127–134.
- (156) Khait, Y. G.; Hoffmann, M. R. A Self-Consistent Version of Quasidegenerate Perturbation Theory. *J. Chem. Phys.* **1998**, *108* (20), 8317–8330.
- (157) Nakano, H. Quasidegenerate Perturbation Theory with Multiconfigurational Self-consistent-field Reference Functions. *J. Chem. Phys.* **1993**, *99* (10), 7983–7992.
- (158) Camacho, C.; Witek, H. A.; Yamamoto, S. Intruder States in Multireference Perturbation Theory: The Ground State of Manganese Dimer. *J. Comput. Chem.* **2009**, *30* (3), 468–478.
- (159) Khait, Y. G.; Song, J.; Hoffmann, M. R. Explication and Revision of Generalized Van Vleck Perturbation Theory for Molecular Electronic Structure. *J. Chem. Phys.* **2002**, *117* (9), 4133–4145.
- (160) Meyer, W. PNO–CI Studies of Electron Correlation Effects. I. Configuration

- Expansion by Means of Nonorthogonal Orbitals, and Application to the Ground State and Ionized States of Methane. *J. Chem. Phys.* **1973**, *58* (3), 1017–1035.
- (161) Shavitt, I.; Redmon, L. T. Quasidegenerate Perturbation Theories. A Canonical van Vleck Formalism and Its Relationship to Other Approaches. *J. Chem. Phys.* **1980**, *73* (11), 5711–5717.
- (162) Hoffmann, M. R.; Helgaker, T. Use of Density Functional Theory Orbitals in the GVVPT2 Variant of Second-Order Multistate Multireference Perturbation Theory. *J. Phys. Chem. A* **2015**, *119* (9), 1548–1553.
- (163) McWeeny, R. *Methods of Molecular Quantum Mechanics*; Academic Press, 1992.
- (164) Edwards, W. D.; Zerner, M. C. A Generalized Restricted Open-Shell Fock Operator. *Theor. Chim. Acta* **1987**, *72* (5–6), 347–361.
- (165) Wahl, A. C.; Das, G. The Multiconfiguration Self-Consistent Field Method. In *Methods of Electronic Structure Theory*; Springer US: Boston, MA, 1977; pp 51–78.
- (166) Roothaan, C. C. J. Self-Consistent Field Theory for Open Shells of Electronic Systems. *Rev. Mod. Phys.* **1960**, *32* (2), 179–185.
- (167) Bach, V.; Lieb, É. H.; Loss, M.; Solovej, J. P. There Are No Unfilled Shells in Unrestricted Hartree-Fock Theory. In *The Stability of Matter: From Atoms to Stars*; Springer-Verlag: Berlin/Heidelberg, 1994; pp 313–315.
- (168) Pulay, P. Convergence Acceleration of Iterative Sequences. the Case of Scf Iteration. *Chem. Phys. Lett.* **1980**, *73* (2), 393–398.
- (169) Almlöf, J.; Faegri, K.; Korsell, K. Principles for a Direct SCF Approach to LICAO - MO Ab Initio Calculations. *J. Comput. Chem.* **1982**, *3* (3), 385–399.

- (170) Nicholls, D.; Li, R. R.; Ware, B.; Pansegrau, C.; Çakir, D.; Hoffmann, M. R.; Oncel, N. Scanning Tunneling Microscopy and Density Functional Theory Study on zinc(II)-Phthalocyanine Tetrasulfonic Acid on Bilayer Epitaxial Graphene on Silicon carbide(0001). *J. Phys. Chem. C* **2015**, *119* (18), 9845–9850.
- (171) Castro Neto, A. H.; Guinea, F.; Peres, N. M. R.; Novoselov, K. S.; Geim, A. K. The Electronic Properties of Graphene. *Rev. Mod. Phys.* **2009**, *81* (1), 109–162.
- (172) Weiss, N. O.; Zhou, H.; Liao, L.; Liu, Y.; Jiang, S.; Huang, Y.; Duan, X. Graphene: An Emerging Electronic Material. *Adv. Mater.* **2012**, *24* (43), 5782–5825.
- (173) An, X.; Butler, T. W.; Washington, M.; Nayak, S. K.; Kar, S. Optical and Sensing Properties of 1-Pyrenecarboxylic Acid-Functionalized Graphene Films Laminated on Polydimethylsiloxane Membranes. *ACS Nano* **2011**, *5* (2), 1003–1011.
- (174) Sun, Y.; Wu, Q.; Shi, G.; Cao, A. Y.; Wei, J. Q.; Li, C. Y.; Jia, Y.; Li, Z.; Li, X.; Wu, D. H.; et al. Graphene Based New Energy Materials. *Energy Environ. Sci.* **2011**, *4* (4), 1113.
- (175) Sahoo, N. G.; Pan, Y.; Li, L.; Chan, S. H. Graphene-Based Materials for Energy Conversion. *Adv. Mater.* **2012**, *24* (30), 4203–4210.
- (176) Avouris, P.; Chen, Z.; Perebeinos, V. Carbon-Based Electronics. *Nat. Nanotechnol.* **2007**, *2* (10), 605–615.
- (177) Liu, Z.; Robinson, J. T.; Sun, X.; Dai, H. PEGylated Nanographene Oxide for Delivery of Water-Insoluble Cancer Drugs. *J. Am. Chem. Soc.* **2008**, *130* (33), 10876–10877.
- (178) Avouris, P.; Dimitrakopoulos, C. Graphene: Synthesis and Applications. *Mater.*

Today **2012**, *15* (3), 86–97.

- (179) Shen, J.; Zhu, Y.; Yang, X.; Li, C. Graphene Quantum Dots: Emergent Nanolights for Bioimaging, Sensors, Catalysis and Photovoltaic Devices. *Chem. Commun.* **2012**, *48* (31), 3686.
- (180) Zhao, J.; Tang, L.; Xiang, J.; Ji, R.; Yuan, J.; Zhao, J.; Yu, R.; Tai, Y.; Song, L. Chlorine Doped Graphene Quantum Dots: Preparation, Properties, and Photovoltaic Detectors. *Appl. Phys. Lett.* **2014**, *105* (11), 111116.
- (181) Nair, R. R.; Blake, P.; Grigorenko, A. N.; Novoselov, K. S.; Booth, T. J.; Stauber, T.; Peres, N. M. R.; Geim, A. K. Fine Structure Constant Defines Visual Transparency of Graphene. *Science* (80-.). **2008**, *320* (5881).
- (182) Lee, S.-K.; Okura, I. Optical Sensor for Oxygen Using a Porphyrin-Doped Sol-Gel Glass. *Analyst* **1997**, *122* (1), 81–84.
- (183) Boukhvalov, D. W.; Katsnelson, M. I. Destruction of Graphene by Metal Adatoms. *Appl. Phys. Lett.* **2009**, *95* (2), 23109.
- (184) Antonini, E.; Rossi-Bernardi, L.; Chiancone, E. *Hemoglobins*; Academic Press, 1981.
- (185) Souza, J. G.; Gelfuso, G. M.; Simão, P. S.; Borges, A. C.; Lopez, R. F. V. Iontophoretic Transport of Zinc Phthalocyanine Tetrasulfonic Acid as a Tool to Improve Drug Topical Delivery. *Anticancer. Drugs* **2011**, *22* (8), 783–793.
- (186) Hains, A. W.; Liang, Z.; Woodhouse, M. A.; Gregg, B. A. Molecular Semiconductors in Organic Photovoltaic Cells. *Chem. Rev.* **2010**, *110* (11), 6689–6735.
- (187) Bansal, A. K.; Holzer, W.; Penzkofer, A.; Tsuboi, T. Absorption and Emission

- Spectroscopic Characterization of Platinum-Octaethyl-Porphyrin (PtOEP). *Chem. Phys.* **2006**, *330* (1–2), 118–129.
- (188) Perry, J. W.; Mansour, K.; Lee, I.-Y. S.; Wu, X.-L.; Bedworth, P. V.; Chen, C.-T.; Ng, D.; Marder, S. R.; Miles, P.; Wada, T.; et al. Organic Optical Limiter with a Strong Nonlinear Absorptive Response. *Science* (80-.). **1996**, *273* (5281).
- (189) Tsuboi, T.; Wasai, Y.; Nabatova-Gabain, N. Optical Constants of Platinum Octaethyl Porphyrin in Single-Layer Organic Light Emitting Diode Studied by Spectroscopic Ellipsometry. *Thin Solid Films* **2006**, *496* (2), 674–678.
- (190) Järvinen, P.; Hämäläinen, S. K.; Ijäs, M.; Harju, A.; Liljeroth, P. Self-Assembly and Orbital Imaging of Metal Phthalocyanines on a Graphene Model Surface. *J. Phys. Chem. C* **2014**, *118* (24), 13320–13325.
- (191) Scudiero, L.; Hipps, K. W. Controlled Manipulation of Self-Organized Ni(II)-Octaethylporphyrin Molecules Deposited from Solution on HOPG with a Scanning Tunneling Microscope. *J. Phys. Chem. C* **2007**, *111* (47), 17516–17520.
- (192) Hämäläinen, S. K.; Stepanova, M.; Drost, R.; Liljeroth, P.; Lahtinen, J.; Sainio, J. Self-Assembly of Cobalt-Phthalocyanine Molecules on Epitaxial Graphene on Ir(111). *J. Phys. Chem. C* **2012**, *116* (38), 20433–20437.
- (193) Miyake, Y.; Tanaka, H.; Ogawa, T. Scanning Tunneling Microscopy Investigation of Vanadyl and cobalt(II) Octaethylporphyrin Self-Assembled Monolayer Arrays on Graphite. *Colloids Surfaces A Physicochem. Eng. Asp.* **2008**, *313–314*, 230–233.
- (194) Huber, V.; Lysetska, M.; Würthner, F. Self-Assembled Single- and Double-Stack π -Aggregates of Chlorophyll Derivatives on Highly Ordered Pyrolytic Graphite.

- Small* **2007**, 3 (6), 1007–1014.
- (195) Moon, H. K.; Son, M.; Park, J. E.; Yoon, S. M.; Lee, S. H.; Choi, H. C. Significant Increase in the Water Dispersibility of Zinc Phthalocyanine Nanowires and Applications in Cancer Phototherapy. *NPG Asia Mater.* **2012**, 4 (4), e12.
- (196) Zhang, H. G.; Sun, J. T.; Low, T.; Zhang, L. Z.; Pan, Y.; Liu, Q.; Mao, J. H.; Zhou, H. T.; Guo, H. M.; Du, S. X.; et al. Assembly of Iron Phthalocyanine and Pentacene Molecules on a Graphene Monolayer Grown on Ru(0001). *Phys. Rev. B* **2011**, 84 (24), 245436.
- (197) Wang, Y.-L.; Ren, J.; Song, C.-L.; Jiang, Y.-P.; Wang, L.-L.; He, K.; Chen, X.; Jia, J.-F.; Meng, S.; Kaxiras, E.; et al. Selective Adsorption and Electronic Interaction of Fe₁₆CuPc on Epitaxial Graphene. *Phys. Rev. B* **2010**, 82 (24), 245420.
- (198) Ren, J.; Meng, S.; Wang, Y.-L.; Ma, X.-C.; Xue, Q.-K.; Kaxiras, E. Properties of Copper (Fluoro-)Phthalocyanine Layers Deposited on Epitaxial Graphene. *J. Chem. Phys.* **2011**, 134 (19), 194706.
- (199) Endlich, M.; Gozdzik, S.; Néel, N.; da Rosa, A. L.; Frauenheim, T.; Wehling, T. O.; Kröger, J. Phthalocyanine Adsorption to Graphene on Ir(111): Evidence for Decoupling from Vibrational Spectroscopy. *J. Chem. Phys.* **2014**, 141 (18), 184308.
- (200) Martin, R. M. *Electronic Structure: Basic Theory and Practical Methods*; Cambridge University Press, 2004.
- (201) Kohanoff, J. *Electronic Structure Calculations for Solids and Molecules: Theory and Computational Methods*. Cambridge University Press 2006, p 348.

- (202) Giannozzi, P.; Baroni, S.; Bonini, N.; Calandra, M.; Car, R.; Cavazzoni, C.; Ceresoli, D.; Chiarotti, G. L.; Cococcioni, M.; Dabo, I.; et al. QUANTUM ESPRESSO: A Modular and Open-Source Software Project for Quantum Simulations of Materials. *J. Phys. Condens. Matter* **2009**, *21* (39), 395502.
- (203) Kresse, G.; Joubert, D. From Ultrasoft Pseudopotentials to the Projector Augmented-Wave Method. *Phys. Rev. B* **1999**, *59* (3), 1758–1775.
- (204) Vanderbilt, D. Soft Self-Consistent Pseudopotentials in a Generalized Eigenvalue Formalism. *Phys. Rev. B* **1990**, *41* (11), 7892–7895.